First Measurement of the Gluon Polarisation in the Nucleon using D Mesons at COMPASS

Martin Frhr. von Hodenberg

Fakultät für Mathematik und Physik
Albert-Ludwigs-Universität Freiburg

First Measurement of the Gluon Polarisation in the Nucleon using D Mesons at COMPASS

Dissertation
zur
Erlangung des Doktorgrades
der
Fakultät für Mathematik und Physik
der
Albert–Ludwigs–Universität
Freiburg im Breisgau

vorgelegt von

Martin Frhr. von Hodenberg

aus Freiburg im Breisgau

November 2005

Dekan:	Prof. Dr. Josef Honerkamp
Leiter der Arbeit:	Prof. Dr. Kay Königsmann
Referent:	Prof. Dr. Kay Königsmann
Korreferent:	Prof. Dr. Jochum van der Bij
Tag der Verkündigung des Prüfungsergebnisses:	16. Januar 2006

Contents

Chapter 1

Introduction

The main goal of high-energy physics is to investigate the fundamental structure of matter and the interactions between its constituents. Most of what is known today about the structure of matter has been revealed by scattering experiments. By its means it was discovered that the atom has a compact nucleus, later this nucleus was found to have substructure itself, comprised of nucleons, namely the proton and the neutron.

Inelastic electron-proton scattering has shown that the nucleon is not point-like, but consists of charged constituents, first called partons. Hadron production in e^+e^- scattering has confirmed the expectation of the fractional charge of the partons and has revealed the existence of gluons, the mediator particles of the strong interaction. This led to a generalisation of the term parton to be a synonym for quarks and gluons. Deep-inelastic lepton-proton scattering in the 1980s and 1990s has then validated the existence of the gluon and has shown that the nucleon's momentum is more or less equally divided among the quarks and the gluons. Growing experimental evidence for the existence of the nucleon's charged constituents eventually led to their identification with the quarks postulated by Gell-Mann and Zweig for the purpose of explaining symmetries in hadron spectroscopy. The unpolarised nucleon structure is by now known to high precision, whereas there remain open questions in the domain of their spin structure.

It is known since the 1920s that the nucleons carry half integer spin and therefore belong to the family of fermions. This means that they obey the Pauli exclusion principle, resulting in the wealth of hadronic structure known to us as opposed to an exclusively populated single hadronic ground state. However, it is not known how this spin comes about in terms of the nucleon's constituents. Possible contributions to the nucleon spin are the spin contributions as well as the orbital angular momenta of the constituent quarks and gluons.

The naive expectation, that the spin is carried by the quarks was proven not to be correct by a measurement of the European Muon Collaboration (EMC). This measurement showed that the contribution of the quarks to the spin of the nucleon may even be consistent with zero. A lot of activity on the experimental as well as on the theoretical side was triggered by this surprising result. Experiments at SLAC, DESY and CERN have since then measured the quark contribution to be about 30 %.

The aim of a new generation of experiments is now to answer the question of how the remaining fraction can be accounted for. COMPASS [1] is a fixed target experiment at CERN, aiming mainly at the measurement of the gluon polarisation $\Delta G/G$ by isolating events originating in photon-gluon fusion. The tool of deep inelastic scattering (DIS) is introduced in Chapter 2 of this thesis along with the theoretical background for the extraction of information on the spin structure of the nucleon. The different approaches to measure the gluon helicity contribution will be summarised, showing that the photon-gluon fusion process is a valuable tool.

The photon-gluon fusion process can be tagged by detecting the decay products of charmed mesons (open charm). For this purpose the COMPASS spectrometer has been set up, featuring the necessary large kinematic acceptance as well as the capability to stand the high rates that are mandatory to a precision measurement. The polarised beam and target as well as the spectrometer are described in Chapter 3. Since the open charm approach is statistically limited, one is especially interested in a highly efficient reconstruction. This motivated detailed studies of the beam reconstruction, leading to major improvements in the reconstruction efficiency as part of this work. The efforts made will be summarised in Chapter 4.

Due to multiple scattering in the solid-state target and the absence of vertex detectors, the charmed meson has to be identified via its invariant mass. One is thus interested in an excellent mass resolution and a supression of the background in order not to accumulate too much background in the mass window analysed. The reconstruction of the charmed mesons has been optimised in view of these points and is covered in Chapter 5. Having a sample of D mesons at hand, the gluon polarisation can be extracted. The necessary ingredients and methods are introduced in Chapter 6. Chapter 7 eventually shows the results of the analysis and an interpretation in the context of already available information on the gluon helicity is given.

Chapter 2

Theoretical Motivation

The spin of a nucleon can be decomposed in the following way [2]

$$\frac{1}{2} = \frac{s_N}{\hbar} = \frac{1}{2}\Delta\Sigma + \Delta G + L_q + L_g, \tag{2.1}$$

where $\Delta\Sigma$ and ΔG are the spin contributions carried by the quarks and the gluons, and $L_{q(g)}$ is the contribution of the orbital angular momentum of the quarks (gluons) to the nucleon spin. The quark spin contribution $\Delta\Sigma$ is given by

$$\Delta\Sigma = \Delta u + \Delta\overline{u} + \Delta d + \Delta\overline{d} + \Delta s + \Delta\overline{s}, \tag{2.2}$$

where $\Delta q\,(\Delta\overline{q})$ is the spin contribution of a (anti)quark $q\,(\overline{q})$. A simple model of the nucleon, which takes into account relativistic effects, gives rise to the expectation that the quark contribution amounts to $\Delta\Sigma \approx 0.75$ [3]. However, the result from a number of fixed-target experiments, such as SMC at CERN, E-143 at SLAC and HERMES at DESY, is a value for $\Delta\Sigma$ of $0.347 \pm 0.24 \pm 0.006$ [4]. It remains to be shown what the reason for the unexpected discrepancy between the expectation for $\Delta\Sigma$ and the measurement is and what the contribution of the gluons and the contributions of the angular momenta to the spin-sum rule (2.1) are.

This chapter introduces the deep inelastic scattering (DIS) as one of the main tools to investigate the nucleon spin and gives an impression of how structure functions are measured. Means to extract information on $\Delta\Sigma$ and ΔG from the currently available data are shown and finally the possibilities of a direct measurement of ΔG are discussed. Part of this chapter is adapted from [5].

2.1 Deep Inelastic Scattering

2.1.1 Deep Inelastic Scattering Kinematics

In deep inelastic lepton-nucleon scattering (DIS) a point-like lepton interacts with a nucleon via the exchange of a virtual boson. In the kinematic range covered by the COMPASS experiment one can safely assume an electromagnetic interaction, where the place of the mediator is taken by a virtual photon. Fig. 2.1 shows a schematic view of this process, where $\mathbf{k}$, $\mathbf{k}'$ and $\mathbf{P}$ are the four-momenta* of the incoming lepton, the scattered lepton and the target nucleon, the latter being at rest in a fixed-target experiment ($\mathbf{P} = (M, 0, 0, 0)$). The four-momenta of the incoming and the scattered lepton are given by $\mathbf{k} = (E, \vec{p})$ and $\mathbf{k}' = (E', \vec{p}\,')$. $\mathbf{S_N}$ and $\mathbf{S_l}$ are the polarisation vectors of the nucleon and the lepton, respectively. Observables in this reaction are the energies of the incoming and the scattered

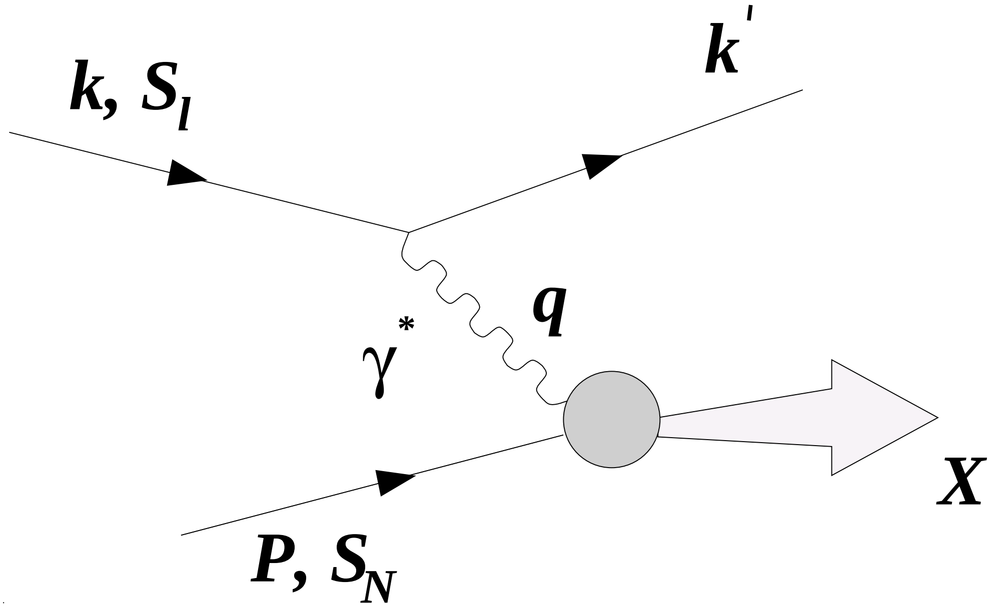

Figure 2.1: Schematic view of the deep inelastic scattering process.

lepton, E and E', and its scattering angle θ. From these observables the following Lorentz invariant variables can be constructed [6]:

$$\begin{aligned} -\mathbf{q}^2 &=: Q^2 = -(\mathbf{k} - \mathbf{k}')^2 \\ &\overset{\text{lab}}{=} -2(m_\mu^2 - EE' + pp' \cos\theta), \qquad (2.3) \\ \mathbf{P} \cdot \mathbf{q} &\overset{\text{lab}}{=} M\nu = M(E - E'), \qquad (2.4) \\ \mathbf{P} \cdot \mathbf{k} &\overset{\text{lab}}{=} ME. \qquad (2.5) \end{aligned}$$

The fractional energy transfer from the lepton to the nucleon is given by

$$y = \frac{\mathbf{P} \cdot \mathbf{q}}{\mathbf{P} \cdot \mathbf{k}} \overset{\text{lab}}{=} \frac{\nu}{E}, \qquad (2.6)$$

*Four-vectors will be denoted in bold face, three-vectors as $\vec{a}$

and the Bjørken scaling variable† is defined by

$$x = \frac{Q^2}{2\mathbf{P}\cdot\mathbf{q}} \stackrel{\text{lab}}{=} \frac{Q^2}{2M\nu}. \tag{2.7}$$

2.1.2 Cross Sections and Structure Functions

The Born cross section for inclusive‡ deep inelastic lepton-nucleon scattering can be expressed as a product of a leptonic tensor $L_{\mu\nu}$ and a hadronic tensor $W_{\mu\nu}$ [6],

$$\frac{d^2\sigma}{d\Omega dE'} = \frac{\alpha^2}{MQ^4}\frac{E'}{E}L_{\mu\nu}W^{\mu\nu}, \tag{2.8}$$

where α is the electromagnetic fine-structure constant and Ω is the solid angle in which the lepton is detected. The leptonic tensor involves the upper part of the schematic in Fig. 2.1 and is calculable in QED, while the hadronic tensor contains the complicated structure of the nucleon, symbolised in the schematic view by the grey circle. To explore this structure is the purpose of the COMPASS experiment along with other experiments, e.g. at DESY, SLAC, CERN and other laboratories.

Both tensors can be decomposed in a polarisation-independent symmetric part and a polarisation-dependent antisymmetric part with respect to $\mu \leftrightarrow \nu$,

$$L_{\mu\nu}(\mathbf{S_l},\mathbf{k},\mathbf{k}') = L^{(S)}_{\mu\nu}(\mathbf{k},\mathbf{k}') + iL^{(A)}_{\mu\nu}(\mathbf{S_l},\mathbf{k},\mathbf{k}'), \tag{2.9}$$

$$W_{\mu\nu}(\mathbf{S_N},\mathbf{P},\mathbf{q}) = W^{(S)}_{\mu\nu}(\mathbf{P},\mathbf{q}) + iW^{(A)}_{\mu\nu}(\mathbf{S_N},\mathbf{P},\mathbf{q}). \tag{2.10}$$

A contraction of the tensors thus yields only terms independent of the involved polarisation vectors $\mathbf{S_l}$ and $\mathbf{S_N}$ and terms depending on both of them.

The two parts of the hadronic tensor can be parametrised in terms of four structure functions, which contain the information about the structure of the nucleon. The symmetric part depends on the dimensionless, unpolarised structure functions $F_1(x,Q^2)$ and $F_2(x,Q^2)$, whereas the antisymmetric polarisation-dependent part involves the polarised structure functions $g_1(x,Q^2)$ and $g_2(x,Q^2)$. The unpolarised structure functions F_2^p and F_2^d for the proton and the deuteron have been measured by several experiments and are well known. A compilation of the data is plotted in Fig. 2.2, showing that the structure functions have been measured over a wide kinematic range.

Eventually the differential cross section can be given as a sum of polarisation-dependent and polarisation-independent terms [13],

$$\frac{d^2\sigma}{d\Omega dE'} = \frac{d^2\overline{\sigma}}{d\Omega dE'} - h_l\cos\psi\frac{d^2\Delta\sigma_\parallel}{d\Omega dE'} - h_l\sin\psi\frac{d^2\Delta\sigma_\perp}{d\Omega dE'}, \tag{2.11}$$

involving the lepton helicity h_l. In this formalism the polarisation vector of the target nucleon $\mathbf{S_N}$ has a polar angle ψ with respect to the initial lepton direction (cf. Fig. 2.3), the two vectors defining the spin plane. The scattered lepton is detected under an azimuthal angle ϕ relative to this spin plane, defining the scattering plane. The term involving $\overline{\sigma}$ in

†Throughout this work the Bjørken scaling variable and the fractional energy will be denoted with x and y, respectively, whereas the spatial coordinates are given as x and y.

‡In inclusive measurements only the scattered lepton is detected.

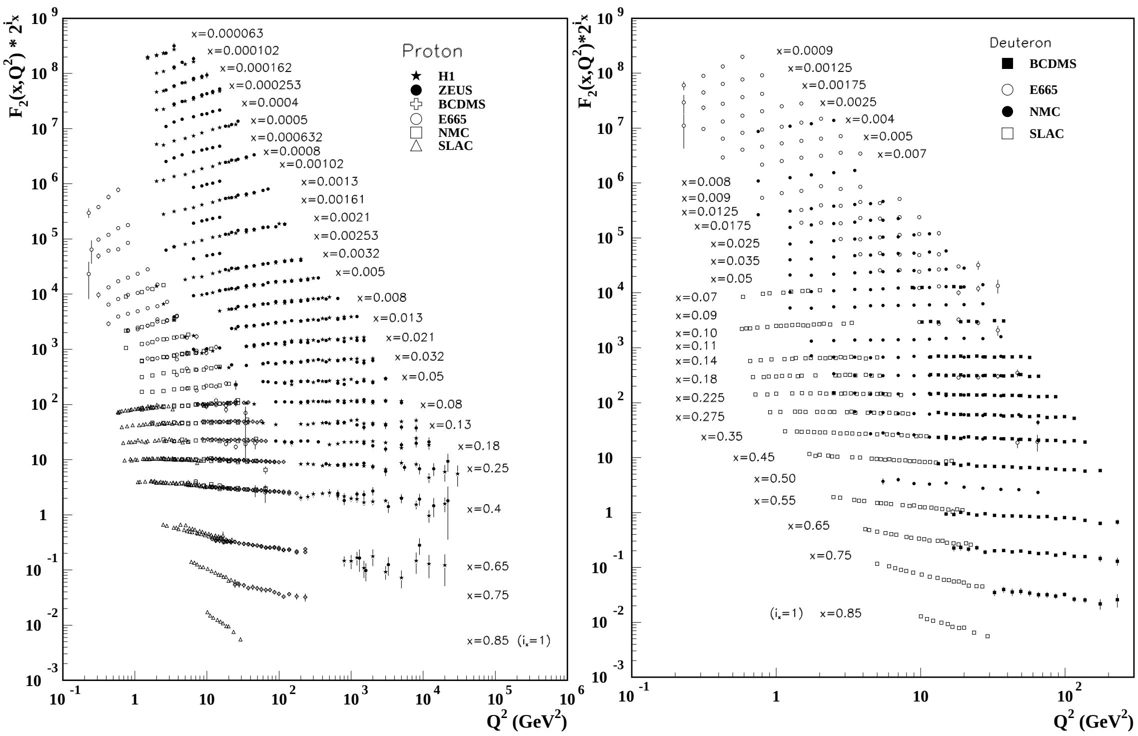

Figure 2.2: The proton and the deuteron structure functions F_2^p and F_2^d as measured in deep inelastic scattering of positrons (ZEUS [7], H1 [8]), electrons (SLAC [9]) and muons (BCDMS [10], E665 [11], NMC [12]) on proton and deuteron, respectively. F_2^p and F_2^d are shown as functions of Q^2 for constant values of x and for the purpose of plotting, a constant $c(x)$ has been added.

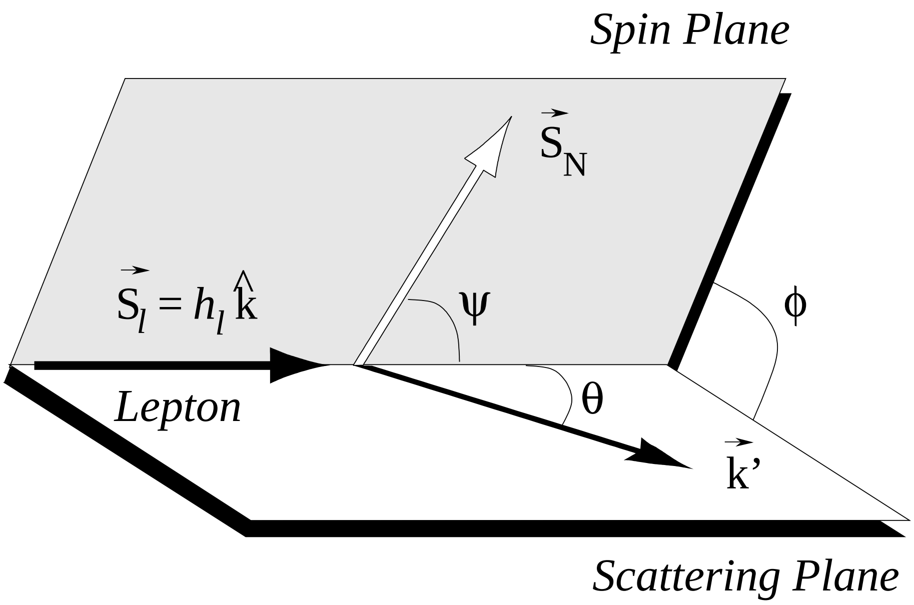

Figure 2.3: Kinematics of polarised lepton scattering from a fixed polarised target.

Eq. (2.11) is polarisation independent and is given by the expression

$$\frac{d^2\overline{\sigma}}{d\Omega dE'} = \frac{4\alpha^2 E'^2}{Q^4}\left(\frac{2F_1(x,Q^2)}{M}\sin^2\frac{\theta}{2} + \frac{F_2(x,Q^2)}{\nu}\cos^2\frac{\theta}{2}\right). \tag{2.12}$$

The two polarisation dependent terms containing $\Delta\sigma_{\parallel}$ and $\Delta\sigma_{\perp}$ refer to the experimentally interesting configurations where the nucleon spin is (anti)parallel ($\psi = 0, \pi$) or orthogonal ($\psi = \pm\pi/2$) to the lepton spin. In the following the lepton spin will be symbolised using $\leftarrow$, whereas for the nucleon spin $\Leftarrow$ will be used. $\Delta\sigma_{\parallel}$ denotes the difference between the cross sections for parallel ($\overset{\leftarrow}{\Leftarrow}$) and antiparallel ($\overset{\leftarrow}{\Rightarrow}$) spin orientations, whereas $\Delta\sigma_{\perp}$ is the difference between the cross sections for the configurations where the target spin points upward ($\leftarrow\Uparrow$) and downward ($\leftarrow\Downarrow$). The corresponding differential expressions are the following [13, 14]:

$$\begin{aligned} \frac{d^2\Delta\sigma_{\parallel}}{d\Omega dE'} &= \frac{d^2(\sigma^{\overset{\leftarrow}{\Leftarrow}} - \sigma^{\overset{\leftarrow}{\Rightarrow}})}{d\Omega dE'} \qquad (2.13) \\ &= \frac{4\alpha^2}{Q^2 M\nu}E'\left[(1 - \frac{y}{2}g_1(x,Q^2) - \frac{Q^2y^2}{4\nu^2} - \frac{m_\mu^2 y}{Q^2}) - \frac{Q^2 y}{2\nu^2}g_2(x,Q^2)\right], \\ \frac{d^2\Delta\sigma_{\perp}}{d\Omega dE'} &= \frac{d^2(\sigma^{\leftarrow\Downarrow} - \sigma^{\leftarrow\Uparrow})}{d\Omega dE'} \qquad (2.14) \\ &= -\cos\phi\frac{4\alpha^2}{Q^2M\nu}E'\sqrt{\frac{Q^2}{\nu^2} - \frac{Q^2y}{\nu^2} - \frac{Q^4y}{\nu^4}}\left[\frac{y}{2}\left(1 + \frac{2m_\mu^2}{Q^2}y\right)g_1(x,Q^2) + g_2(x,Q^2)\right]. \end{aligned}$$

Since the term containing g_2 in Eq. (2.13) is kinematically suppressed, the corresponding longitudinal polarisation constellation is best suited for a determination of g_1, whereas having a measurement of g_1 at hand, g_2 can be determined using the orthogonal polarisation constellation.

2.1.3 Cross Section Asymmetries

The spin-dependent parts of the cross sections appear as contributions on top of the spin-independent part. Spin-dependent effects can thus be determined from differences of cross sections, which, however, are sensitive even to small changes in the experimental setup. One therefore studies cross section asymmetries, where these systematic effects largely cancel. The photon-nucleon asymmetries A_1 and A_2 are given by [15]

$$A_1 = \frac{\sigma^{1/2} - \sigma^{3/2}}{\sigma^{1/2} + \sigma^{3/2}} = \frac{g_1 - \gamma^2 g_2}{F_1}, \tag{2.15}$$

$$A_2 = \frac{2\sigma^{\mathrm{TL}}}{\sigma^{1/2} + \sigma^{3/2}} = \gamma \frac{g_1 + g_2}{F_1}, \tag{2.16}$$

where

$$\gamma = \frac{2Mx}{\sqrt{Q^2}} = \frac{\sqrt{Q^2}}{\nu}. \tag{2.17}$$

The cross sections $\sigma^{1/2}$ ($\sigma^{3/2}$) are the photon-nucleon absorption cross sections for transversely[§] polarised virtual photons with a total photon-nucleon angular momentum component along the direction of the photon momentum of 1/2 (3/2). σ^{TL} is the interference cross section between the transverse and the longitudinal polarisation components of the virtual photon.

The asymmetries A_1 and A_2 are related to the experimentally accessible lepton-nucleon asymmetries $A_{\|}$ and $A_{\perp}$, which are given by

$$A_{\|} = \frac{\sigma^{\overset{\leftarrow}{\Rightarrow}} - \sigma^{\overset{\leftarrow}{\Leftarrow}}}{\sigma^{\overset{\leftarrow}{\Rightarrow}} + \sigma^{\overset{\leftarrow}{\Leftarrow}}} \quad \text{and} \tag{2.18}$$

$$A_{\perp} = \frac{\sigma^{\leftarrow\Downarrow} - \sigma^{\leftarrow\Uparrow}}{\sigma^{\leftarrow\Downarrow} + \sigma^{\leftarrow\Uparrow}} \tag{2.19}$$

via

$$A_{\|} = D(A_1 + \eta A_2) \quad \text{and} \tag{2.20}$$

$$A_{\perp} = d(A_2 - \xi A_1). \tag{2.21}$$

In these expressions the virtual photon depolarisation factor D and the kinematic factors d, η and ξ are given by

$$D = \frac{y[(1+\gamma^2 y/2)(2-y) - 2y^2 m_\mu^2/Q^2]}{y^2(1-2m_\mu^2/Q^2)(1+\gamma^2) + 2(1+R)(1-y-\gamma^2 y^2/4)}, \tag{2.22}$$

[§]The term "transversely" refers to the orientation of the polarisation vector of the photon field relative to the direction of motion. The photon helicity, on the other hand, is ± 1, which corresponds to right- and left-circular polarisation.

$$d = \frac{\sqrt{1-y-\gamma^2 y^2/4}(1+\gamma^2 y/2)}{(1-y/2)(1+\gamma^2 y/2)-y^2 m_\mu^2/Q^2} D, \tag{2.23}$$

$$\eta = \frac{\gamma(1-y-\gamma^2 y^2/4-y^2 m_\mu^2/Q^2)}{(1+\gamma^2 y/2)(1-y/2)-y^2 m_\mu^2/Q^2} \quad \text{and} \tag{2.24}$$

$$\xi = \frac{\gamma(1-y/2-y^2 m_\mu^2/Q^2)}{1+\gamma^2 y/2}, \tag{2.25}$$

where R is the ratio of longitudinal and transverse photo-absorption cross sections, $R = \sigma_L/\sigma_T$.

For a measurement of g_1 or g_2 one in principle needs to determine both asymmetries $A_\parallel$ and $A_\perp$. For further discussion it is useful to express g_1 and g_2 in terms of $A_\parallel$ and A_2:

$$g_1 = \frac{F_1}{1+\gamma^2}\left(\frac{A_\parallel}{D} + (\gamma-\eta)A_2\right) \tag{2.26}$$

$$g_2 = \frac{F_1}{1+\gamma^2}\left(-\frac{A_\parallel}{D} + (\eta+\frac{1}{\gamma})A_2\right). \tag{2.27}$$

The photon-nucleon asymmetries obey the positivity relations $|A_1| \leq 1$ and $|A_2| \leq \sqrt{R}$ [16]. Taking advantage of the latter bound and the fact that the terms with A_2 of Eqs. (2.20) and (2.26) are suppressed by small kinematic factors, one can neglect the contribution of A_2 and gets for these expressions

$$A_1 \simeq \frac{A_\parallel}{D} \quad \text{and} \tag{2.28}$$

$$g_1 \simeq \frac{F_1}{1+\gamma^2}\frac{A_\parallel}{D}. \tag{2.29}$$

The formalism introduced so far covers the scattering from spin-$\frac{1}{2}$ targets. Generalising it to spin-1 targets like the deuteron introduces a new structure function, commonly denoted by b_1. This new structure function has recently been measured and was found to be different from zero but small [17]. In the case of the COMPASS solid-state target its influence is in addition strongly suppressed by the small tensor polarisation¶ and can thus be neglected. Under this assumption the photon-deuteron asymmetry is given by [15]

$$A_1 = \frac{\frac{1}{2}(\sigma^0-\sigma^2)}{\frac{1}{3}(\sigma^0+\sigma^1+\sigma^2)}, \tag{2.30}$$

implying that the lepton-deuteron asymmetry is determined, as in the spin-$\frac{1}{2}$ case, by

$$A_\parallel = \frac{\sigma^{\overleftarrow{\Rightarrow}} - \sigma^{\overleftarrow{\Leftarrow}}}{\sigma^{\overleftarrow{\Rightarrow}} + \sigma^{\overleftarrow{\Leftarrow}}}. \tag{2.31}$$

¶The tensor polarisation is given by $T = 1/2(1-3p_0)$, where p_0 is the relative population of the state with spin projection equal to zero.

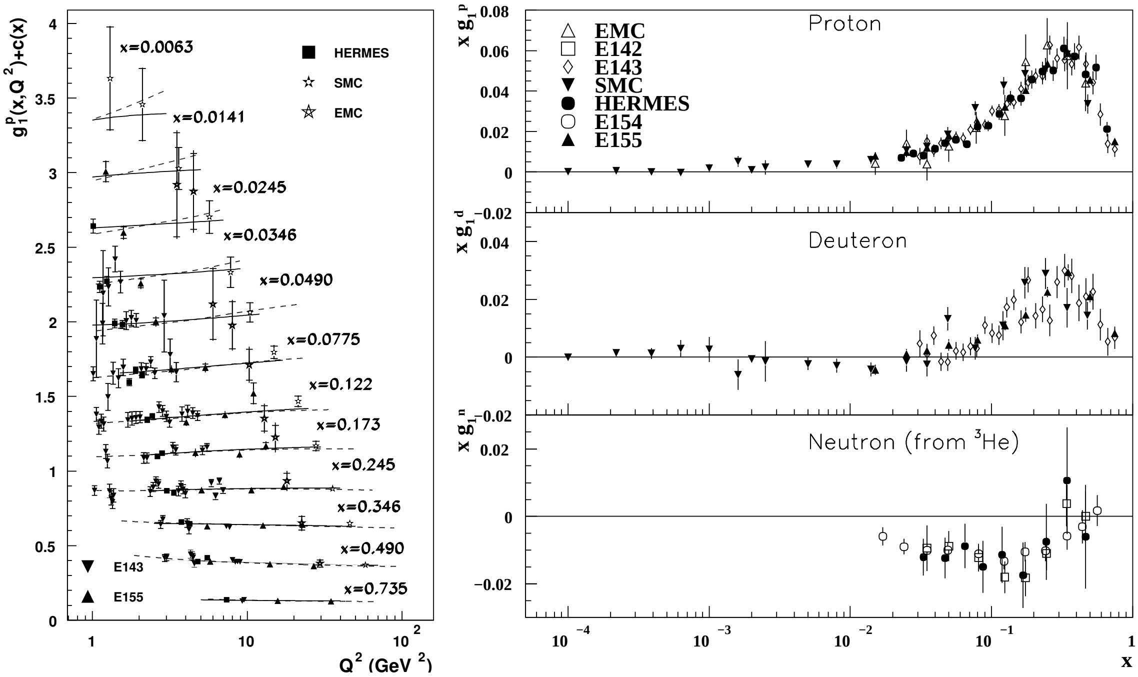

Figure 2.4: Left: A compilation of data on the polarised proton structure function $g_1(x, Q^2)$ for various fixed values of x [18]. Right: The polarised structure function $xg_1(x)$ of the proton, deuteron and neutron as measured in deep inelastic scattering of polarised electrons/positrons (E142 [19], E143 [20], E154 [21], E155 [22], HERMES [23]) and muons (EMC [24], SMC [25]), shown at the measured Q^2 (except for EMC data given at $Q^2 = 10.7\,(\mathrm{GeV}/c)^2$ and E155 data given at $Q^2 = 5\,(\mathrm{GeV}/c)^2$).

Fig. 2.4 presents a compilation of data on the structure function g_1. The plot on the left shows the structure function for the proton g_1^p as a function of Q^2 for various fixed x. Compared to the unpolarised case the kinematic range in which information is available is less extensive. This is due to the fact that the data have exclusively been collected by fixed-target experiments. The other plots show xg_1 for the proton, deuteron and neutron as functions of x, based on the world data up to 2004. The result of a recent measurement of g_1^{d} by COMPASS [26] is plotted in Fig. 2.5 and shows the capability of the experiment to contribute significantly especially in the region of small x.

2.2 Quark Parton Model

The Quark Parton Model (QPM) allows an interpretation of the structure functions of the nucleon in terms of the nucleon's constituents. This section is devoted to the "leading order" (LO) QPM, in which only quarks take part, the QCD-improved "next-to-leading order" (NLO) version of the model also takes into account gluon radiation by the quarks and is covered in Sec. 2.3.1.

In the "LO" Quark Parton Model [27] the nucleon is described as an ensemble of point-like, massless, spin-$\frac{1}{2}$ particles called quarks, which can be assumed as free particles when

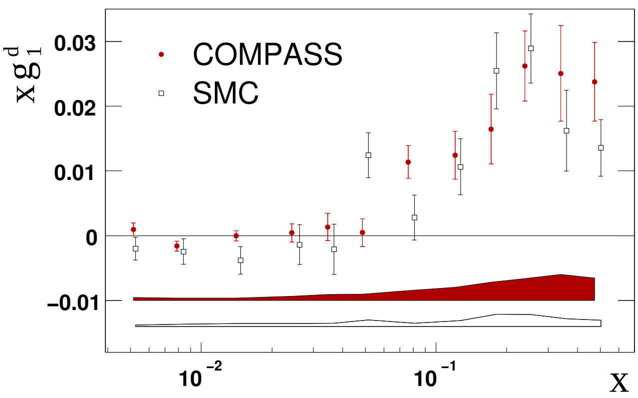

Figure 2.5: The plot shows the result for g_1^{d} as measured by COMPASS, compared to the values obtained by SMC [25]. The COMPASS points are shown at the measured Q^2. The SMC points are evolved to the Q^2 of the corresponding COMPASS points and shifted in x for clarity. The upper and lower error bands show the systematic errors for the COMPASS and SMC points, respectively. The error bars give the statistical error and show that the COMPASS measurement improves our knowledge of this structure function especially at small x.

probed in the Bjørken limit (ν, $Q^2 \to \infty$, fixed x). Under these conditions deep inelastic lepton-nucleon scattering can be interpreted as elastic scattering from quarks and the structure functions can be conveniently expressed in terms of quark distribution functions. The model is formulated in the infinite momentum frame, in which the nucleon moves with infinite momentum, allowing to neglect the rest masses as well as the transverse momentum components of the quarks. In this frame the scaling variable x can be identified with the fraction of nucleon momentum carried by the quark which has been struck by the virtual photon.

An important implication of the QPM is the Bjørken-scaling of the structure functions, i.e. the phenomenon that in the Bjørken limit, where Q^2 and ν go to infinity, leaving x fixed, $F_i(x, Q^2)$ become functions of x only [28]:

$$F_{1,2}(x, Q^2) \stackrel{(\nu,\mathrm{Q}^2 \to \infty)}{\longrightarrow} F_{1,2}(x). \tag{2.32}$$

Only a relatively small dependence of the structure functions on Q^2 was experimentally observed in experiments at SLAC in the early 1970s. This was one of the motivations for the QPM. Another important implication is the Callan-Gross relation [29]

$$F_2(x) = 2xF_1(x), \tag{2.33}$$

a consequence of the assumption that the massless quarks carry spin 1/2. Also this was experimentally confirmed.

The unpolarised structure functions are given as a sum over all quark flavours f [30]:

$$F_1(x) = \frac{1}{2}\sum_f e_f^2 q_f(x) \tag{2.34}$$

$$F_2(x) \quad = \quad x\sum_f e_f^2 q_f(x), \tag{2.35}$$

where e_f is the charge of the quark of given flavour f and $q_f(x)$ is the probability to find a quark of flavour f and fractional momentum x.

The polarised structure function g_1 can also be conveniently interpreted in the QPM. Fig. 2.6 shows a schematic view of polarised photon-quark scattering in the infinite momentum frame. In order to conserve helicity, the polarised photon will have to flip the

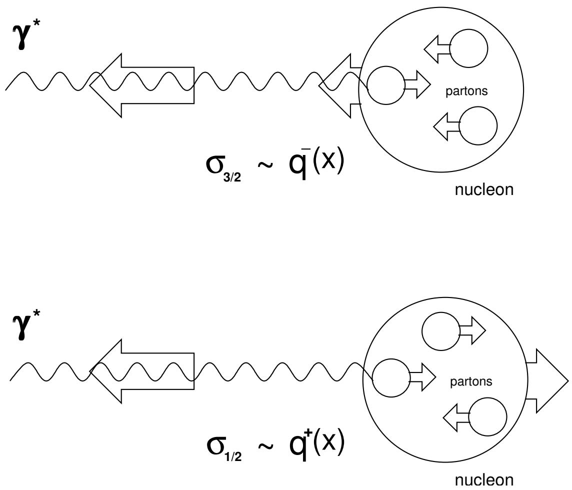

Figure 2.6: A schematic view of polarised DIS in the infinite momentum frame. As dictated by helicity conservation, the polarised photon hits a quark with spin anti-parallel (top) or parallel (bottom) to the nucleon spin, depending on the orientation of the target spin.

spin of the quark in the collision. This requirement allows the photon to couple only to such quarks whose spin is aligned anti-parallel to the photon spin. Therefore the photon-nucleon absorption cross section $\sigma^{1/2}$ ($\sigma^{3/2}$) is proportional to $\sum_f e_f^2 q^+$ ($\sum_f e_f^2 q^-$), where $q^{+(-)}$ is the probability of finding a quark with flavour f and spin aligned parallel (anti-parallel) to the nucleon spin. These probabilities are correlated with the unpolarised quark distributions q_f via $q_f(x) = q_f^+(x) + q_f^-(x)$. The polarised structure function g_1 is given by [30]

$$g_1(x) = \frac{1}{2}\sum_f e_f^2 \Delta q_f(x), \tag{2.36}$$

where the polarised quark distribution is given by

$$\Delta q_f(x) = q_f^+(x) - q_f^-(x). \tag{2.37}$$

The structure function g_2 does not have an interpretation in the QPM.

Up to now the theoretical models are not capable of making predictions for $g_1(x)$. However, theoretical predictions have been made for the first moment of $g_1(x)$, explaining its importance. The first moment is defined as

$$\Gamma_1 = \int_0^1 g_1(x)dx. \tag{2.38}$$

For the first moment one thus gets for the proton

$$\Gamma_1^p = \frac{1}{2}\left(\frac{4}{9}\Delta u + \frac{1}{9}\Delta d + \frac{1}{9}\Delta s\right), \tag{2.39}$$

where $\Delta q_f = \int_0^1 dx \Delta q_f(x)$. The expression for the neutron is obtained by $\Delta u \leftrightarrow \Delta d$ assuming isospin symmetry.

2.2.1 Operator Product Expansion

The operator product expansion (OPE) is an alternative approach to the QPM and gives the possibility to derive sum rules for the structure functions directly from QCD and thus in a model independent way. It relates the first moment of $g_1(x)$ (Eq. (2.38)) to a product of perturbatively calculable coefficient functions and the proton matrix element $a_k = S_\mu^{-1}\langle \mathbf{P},\mathbf{S}|J_{5\mu}^k|\mathbf{P},\mathbf{S}\rangle$ of the axial-vector currents for a proton with four-momentum $\mathbf{P}$ and covariant polarisation vector $\mathbf{S}$. The currents are given in terms of the generators of λ_k of flavour SU(3), as [31]

$$J_{5\mu}^k = \overline{\psi}\frac{\lambda_k}{2}\gamma_5\gamma_\mu\psi, \tag{2.40}$$

where $\lambda_0 = \mathbb{1}$ and $\psi = (\psi_\mathrm{u}, \psi_\mathrm{d}, \psi_\mathrm{s})$. Assuming free quark fields and considering only the lightest three quark flavours, the relations simplify and OPE gives for the proton (neutron)

$$\Gamma_1^{\mathrm{p(n)}} = \frac{1}{9}a_0 + \frac{1}{12}\left(\pm a_3 + \frac{1}{\sqrt{3}}a_8\right). \tag{2.41}$$

The matrix elements a_k can be decomposed in terms of contributions from different flavours as

$$\begin{aligned} a_0 &= a_u + a_d + a_s, \\ a_3 &= a_u - a_d \qquad \text{and} \\ a_8 &= \frac{1}{\sqrt{3}}(a_u + a_d - 2a_s). \end{aligned} \tag{2.42}$$

Assuming isospin symmetry, the matrix element a_3 is equal to the ratio $|g_A/g_V|$ of the axial vector and vector coupling constants, which are known from neutron decay [6]. This gives rise to the Bjørken sum rule [32]

$$\Gamma_1^p - \Gamma_1^n = \frac{1}{6}\left|\frac{g_A}{g_V}\right|. \tag{2.43}$$

This prediction can be used to test the theory when data on both nucleons are at hand. The Bjorken sum rule has been confirmed by various experiments, such as SMC, E143 and HERMES.

If $\mathrm{SU}(3)_f$ flavour symmetry is assumed, the elements a_3 and a_8 can be expressed in terms of coupling constants F and D, as [33]

$$a_3 = \left|\frac{g_A}{g_V}\right| = F + D \qquad \text{and} \qquad a_8 = 3F - D. \tag{2.44}$$

With this assumption a_0 can be determined from a measurement of $\Gamma_1^{\mathrm{p(n)}}$ using Eq. (2.41), since the coupling constants F and D can be experimentally obtained from neutron and hyperon β-decays.

In the LO QPM, where a_q ($q \in \{u, d, s\}$) can be identified with the first moment Δq_f, a_0 is the spin contribution of the quarks: $a_0 = \Delta\Sigma$ and Eq. (2.39) is equal to Eq. (2.41) [33]. Applying the above mentioned assumptions, one can in this picture deduce the quark contribution to the nucleon spin, namely $\Delta\Sigma$, from a measurement of the first moment of $g_1(x)$. This is how the well known result of the EMC, $\Delta\Sigma = 0.12 \pm 0.09$ [24] was obtained, which, however, is very different from the naive expectation and gave rise to more sophisticated theoretical tools that will be sketched in the following sections.

2.3 The Gluon in the Nucleon

2.3.1 QCD improved Parton Model

As shown in Fig. 2.2 and Fig. 2.4, the prediction of scale invariance of the structure functions is only approximately fulfilled. The dependence of the structure functions on Q^2 for a fixed x is explained in Quantum Chromodynamics (QCD) by the interaction of quarks via gluons, leading to a cloud of gluons and a sea of quark-antiquark pairs surrounding each quark [34]. This cloud is resolved better with increasing Q^2. A quark at a given scale could thus at a different scale appear as a quark and a gluon which it just has emitted. This leads to a Q^2 dependence of the parton distributions $\Delta q(x, Q^2)$ and thus to the scale dependence of the structure functions.

The evolution of the parton-distribution functions with Q^2 is described by the Dokshitzer-Gribov-Lipatov-Altarelli-Parisi (DGLAP) equations [35–37], given here for the singlet and non-singlet combinations of the polarised quark distributions $\Delta\Sigma$ and Δq^{NS} as well as the polarised gluon distribution ΔG

$$\frac{d}{d\ln Q^2}\Delta q^{\mathrm{NS}}(x, Q^2) = \frac{\alpha_s(Q^2)}{2\pi}\Delta P_{qq}^{\mathrm{NS}} \otimes \Delta q^{\mathrm{NS}}(x, Q^2) \tag{2.45}$$

$$\frac{d}{d\ln Q^2}\begin{pmatrix} \Delta\Sigma(x, Q^2) \\ \Delta G(x, Q^2) \end{pmatrix} = \frac{\alpha_s}{2\pi}\begin{pmatrix} \Delta P_{qq}^{\mathrm{S}} & 2n_f \Delta P_{qg}^{\mathrm{S}} \\ \Delta P_{gq}^{\mathrm{S}} & \Delta P_{gg}^{\mathrm{S}} \end{pmatrix} \otimes \begin{pmatrix} \Delta\Sigma(x, Q^2) \\ \Delta G(x, Q^2) \end{pmatrix}, \tag{2.46}$$

where

$$\Delta\Sigma(x, Q^2) = \sum_{i=1}^{n_f}(\Delta q_i(x, Q^2) + \Delta\overline{q}_i(x, Q^2)), \tag{2.47}$$

$$\Delta q^{\mathrm{NS}}(x, Q^2) = \sum_{i=1}^{n_f}\left(\frac{e_i^2}{\langle e^2\rangle} - 1\right)(\Delta q_i(x, Q^2) + \Delta\overline{q}_i(x, Q^2)). \tag{2.48}$$

with the number of active quark flavours denoted by n_f and the mean quadratic charge given by

$$\langle e^2\rangle = \frac{1}{n_f}\sum_f e_f^2. \tag{2.49}$$

The convolution is defined by

$$(a \otimes b)(x) = \int_x^1 \frac{dx'}{x'} a\left(\frac{x}{x'}\right) b(x'). \tag{2.50}$$

The DGLAP equations involve the so-called splitting functions $\Delta P_{ij} = P_{i^+j^+} - P_{i^-j^+}$, where $P_{i^-j^+}(x/x')$[‖] gives the probability that a parton j with positive helicity and momentum $x'\mathbf{P}$ radiates another parton i with negative helicity and momentum $x\mathbf{P}$ (cf. Fig. 2.7).

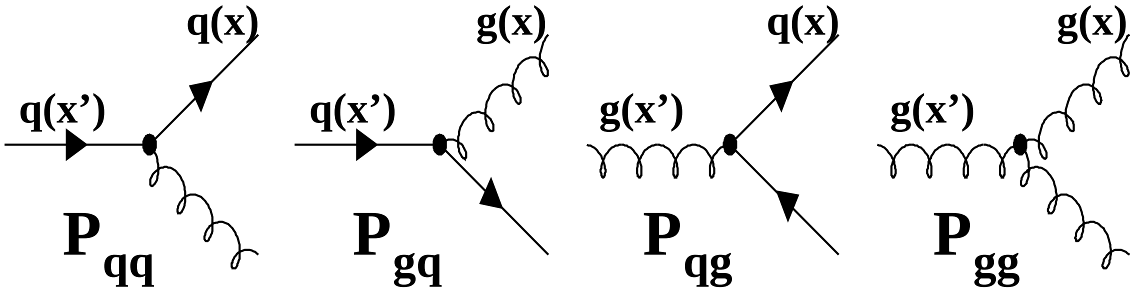

Figure 2.7: Schematic view of the processes related to the splitting functions, which enter the DGLAP equations. For simplicity the helicities have been omitted.

An advantage of the grouping of the parton distributions in singlet and non-singlet combinations is that the non-singlet version evolves independently of the gluon distribution as opposed to the individual parton densities. Given a parton density at a specific scale Q_0^2 one can transform this function to a different scale Q^2 using these DGLAP equations. However, this knowledge on the shape at Q_0^2 is mandatory. The DGLAP formalism by itself is not sufficient to deduce the shape of the distribution.

Taking into account QCD effects leads to corrections in the expressions for the structure functions and consequently in the expressions for the first moments of g_1 and the corresponding sum rules. The polarised structure function g_1 is then given by [34]

$$\begin{aligned} g_1(x,Q^2) &= \frac{1}{2}\langle e^2\rangle\{C_q^{\mathrm{NS}}(x,Q^2)\otimes\Delta q^{\mathrm{NS}}(x,Q^2) \\ &+ C_q^{\mathrm{S}}(x,Q^2)\otimes\Delta\Sigma(x,Q^2)+2n_fC_g(x,Q^2)\otimes\Delta G(x,Q^2)\}. \end{aligned} \tag{2.51}$$

The coefficient functions C_q^{NS}, C_q^{S} and C_g as well as the splitting functions P_{ij} of the DGLAP formalism can be expanded in a power series in the strong coupling constant α_s. The leading order of the expansion of the coefficient functions recovers the "LO" QPM described in Sec. 2.2.

Due to the non-abelian character of QCD the strong coupling constant is a decreasing function of Q^2. For small Q^2 the coupling constant is of the order of one and a perturbative treatment is not possible. This regime is called soft. For the hard regime of large Q^2, however, the coupling constant decreases making perturbative calculations possible. The

‖The splitting function $\Delta P(x)$ is then obtained by integrating over all possible initial fractions x'.

structure of Eq. (2.51) reflects the principle of factorisation. The perturbatively calculable hard part of the interaction namely the photon-parton scattering is presented by the coefficient functions C_i^j, whereas the soft part, i.e. the structure of the nucleon, is absorbed in the parton distributions. However, the way of separating these two parts is ambiguous, leading to different so-called factorisation schemes and scales, where the latter refers to the scale at which the separation takes place. This ambiguity enters at next-to-leading order and makes the interpretation of experimental results difficult as we shall see. One should stress that the g_1 structure function as a physical observable does not depend on the choice of factorisation scheme.

Two prominent factorisation schemes are the Modified Minimal Subtraction scheme ($\overline{\mathrm{MS}}$) and the Adler-Bardeen scheme (AB). The following discussion of these schemes is simplified when one considers the first moment of g_1, since in this case the convolution is turned into a simple product of the first moments of coefficient functions and parton densities

$$\Gamma_1(Q^2) = \frac{1}{2}\langle e^2\rangle \left\{ C_q^{\mathrm{NS}}(Q^2)\Delta q^{\mathrm{NS}}(Q^2) + C_q^{\mathrm{S}}(Q^2)\Delta\Sigma(Q^2) + 2n_f C_g(Q^2)\Delta G(Q^2)\right\}. \quad (2.52)$$

The two schemes differ in how they treat certain soft contributions. In the $\overline{\mathrm{MS}}$ scheme these contributions reside in the coefficient function, whereas in the AB scheme they are absorbed in the parton distributions [38]. As a consequence, the first moment of $C_g(x, Q^2)$ vanishes in the $\overline{\mathrm{MS}}$ scheme up to next-to-next-to-leading order (NNLO) and therefore the first moment of g_1 decouples from the gluon distribution ΔG. In contrast to this, the first moment of $C_g(x, Q^2)$ does not vanish in the AB scheme, leading to a direct contribution of $\Delta G(Q^2)$ to g_1 and Γ_1. This results in the following relation

$$\Delta\Sigma^{\overline{\mathrm{MS}}}(Q^2) = \Delta\Sigma^{\mathrm{AB}} - \frac{n_f\alpha_s(Q^2)}{2\pi}\Delta G(Q^2). \quad (2.53)$$

The fact that $\Delta\Sigma^{\mathrm{AB}}$ is independent of Q^2 is conserved to all orders in α_s due to the Adler-Bardeen theorem [39], which states that the gluon anomaly covered in the next section does not receive higher order corrections.

2.3.2 Anomalous Gluon Contribution

The previous section showed how the QPM can be expanded to accommodate the scaling violation, so this section is devoted to bringing the OPE to an equivalent level of sophistication. In Chapter 2.2 it was mentioned that the OPE relates the first moment of g_1 to a product of perturbatively calculable coefficient functions and the proton matrix element a_k of the axial-vector currents. If an interaction among the partons is allowed, i.e. the assumption of free quark fields is dropped, OPE yields [40]

$$\Gamma_1^{p(n)} = \frac{1}{9}a_0(Q^2)C^{\mathrm{S}}(Q^2) + \frac{1}{12}\left(\pm a_3 + \frac{1}{\sqrt{3}}a_8\right)C^{\mathrm{NS}}(Q^2), \quad (2.54)$$

where the coefficient functions $C^i(Q^2)$ can be expanded in a power series in α_s and the LO recovers Eq. (2.41). In this picture the Bjørken sum rule now reads [40]

$$\Gamma_1^p - \Gamma_1^n = \frac{1}{6}\left|\frac{g_A}{g_V}\right| C^{\mathrm{NS}}. \tag{2.55}$$

Whether the matrix element a_k is a function of Q^2 depends on whether the corresponding current is conserved. The currents $J^3_{5\mu}$ and $J^8_{5\mu}$ are conserved to the extent that $\mathrm{SU}(2)_f$ and $\mathrm{SU}(3)_f$ are exact symmetries**. In contrast to that $\partial^\mu J^0_{5\mu} \neq 0$ even in the limit $m_q \to 0$. This is called the axial anomaly and was rediscovered in the analogy to an anomaly in QED [41] in the aftermath of the first measurement of Γ_1 by the EMC. The matrix element of $J^0_{5\mu}$ is modified in the following way

$$a_0(Q^2) = a_0^{\mathrm{LO}} - \frac{n_f \alpha_s(Q^2)}{2\pi} \Delta G(Q^2), \tag{2.56}$$

where a_0^{LO} corresponds to the matrix element in Eq. (2.41), i.e. to $\Delta\Sigma$ in the LO QPM. Even though the anomalous gluon contribution may look like an ordinary correction, which decreases like α_s with rising Q^2, it does not vanish in the limit $Q^2 \to \infty$:

$$\frac{d\alpha_s(Q^2)\Delta G(Q^2)}{d \ln Q^2} = 0 + \mathcal{O}(\alpha_s^2(Q^2)). \tag{2.57}$$

Eqns. (2.56) and (2.53) show that what is measured in a polarised DIS experiment, namely $a_0(Q^2)$, cannot easily be interpreted due to the scheme dependence. In the two schemes mentioned in Chapter 2.3.1 we get for the spin contribution of the quarks

$$\Delta\Sigma^{\overline{\mathrm{MS}}}(Q^2) = a_0(Q^2) \tag{2.58}$$

$$\Delta\Sigma^{\mathrm{AB}} = a_0(Q^2) + \frac{n_f \alpha_s(Q^2)}{2\pi}\Delta G(Q^2). \tag{2.59}$$

This means that in the AB scheme the unexpected smallness of the measured value can be explained by a reduction due to the anomalous gluon contribution, which has to be added back to arrive at the quark contribution. This, however, has to be confirmed by a measurement of ΔG.

The discussion above has shown that the spin-sum rule (Eq. (2.1)) is more subtle, i.e the contributions are in general scheme and scale dependent

$$\frac{1}{2} = \frac{1}{2}\Delta\Sigma^{\mathrm{fs}}(Q^2) + \Delta G^{\mathrm{fs}}(Q^2) + L_q^{\mathrm{fs}}(Q^2) + L_g^{\mathrm{fs}}(Q^2), \tag{2.60}$$

where fs denotes a chosen factorisation scheme.

The conclusion is that in order to further pin down the contributions to the nucleon spin, a measurement of the polarised gluon distribution ΔG is mandatory. It is needed on the one hand to fix the gluon contribution to the spin-sum rule and on the other to be able to extract the quark contribution from the g_1 measurement in the case of the AB scheme. The next sections will discuss how such a measurement of ΔG can be done.

**The fact that these symmetries are slightly broken due to the different quark masses leads to a partial conservation of the currents and thus to a small scale dependence of a_3 and a_8. This dependence, however, can be neglected [33].

2.4 QCD Analysis of g_1

The knowledge of how the parton distributions evolve with Q^2 provides a handle to extract them from a measurement of the structure function in the x-Q^2 plane. The Q^2 dependence of the structure functions in particular makes this approach sensitive to the gluon distribution. The basis of the analysis are the DGLAP equations and thus the splitting functions up to a given order. In addition to that there is the ansatz for the structure functions, e.g. $g_1(x, Q^2)$ given in Eq. (2.51), for which one needs the coefficient functions also calculated up to a given order. This, however, implies a choice of a factorisation scheme. Currently the splitting and coefficient functions for the polarised case are available up to NLO [42,43].

The starting point of the analysis is a parametrisation of the parton densities, namely $\Delta\Sigma$, Δq^{NS} and ΔG, at a given scale Q_0^2. The parametrisation is then evolved to the Q^2 of the g_1 measurement and the parameters are optimised such that the following χ^2 is minimised:

$$\chi^2 = \sum_i \frac{[g_1^{\mathrm{calc}}(x, Q^2) - g_1^{\mathrm{data}}(x, Q^2)]^2}{[\delta g_1^{\mathrm{data}}(x, Q^2)]^2}, \tag{2.61}$$

where the sum runs over the experimental data points g_1^{data} with a statistical error $\delta g_1^{\mathrm{data}}$ and g_1^{calc} is computed from the parametrisation. The analysis crucially depends on how extensively the structure function has been measured in the mentioned kinematic plane. In the unpolarised case (cf. Fig. 2.2) the coverage in this plane and the statistical accuracy are excellent and as a consequence the parton densities can be determined rather well. The situation is different in the polarised case, where the data sample has not yet reached the same kinematic extent (cf. Fig. 2.4) due to the fact that it exclusively comes from fixed target experiments. As can be concluded from Fig. 2.8 the singlet and non-singlet distributions $\Delta\Sigma$ and Δq^{NS} are well determined. The gluon distribution ΔG, however, is hardly constrained at all with an error of 50-100 %.

The QCD analysis of $g_1(x, Q^2)$ is a powerful tool to extract the parton densities, but suffers from the limited kinematic coverage of the polarised data, very much in contrast to the unpolarised case. In addition there is the handicap that there is no equivalent to the momentum sum rule for the polarised quantities, which certainly helps to constrain the distribution in the unpolarised analysis due to the fact that it links the NLO-quantity $G(x, Q^2)$ to the directly probed LO-quantity $\Sigma(x, Q^2)$:

$$1 = \int_0^1 x\Sigma(x, Q^2)dx + \int_0^1 xG(x, Q^2)dx. \tag{2.62}$$

It is therefore necessary to have a direct measurement of ΔG using a process where the gluon is probed directly. The possibilities at hand for such a measurement are introduced in the next section.

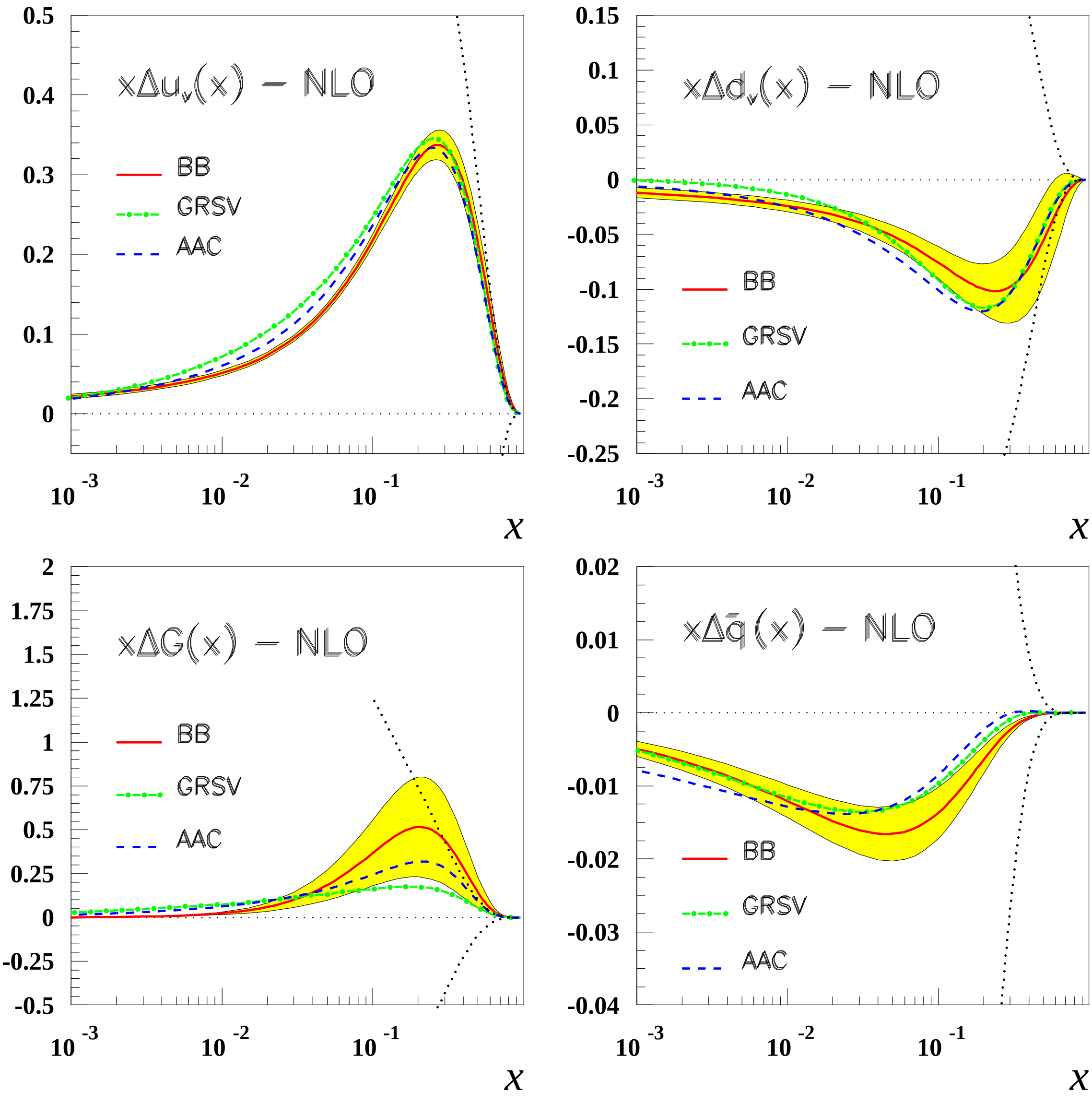

Figure 2.8: The polarised parton distributions at $Q^2 = 4\,(\mathrm{GeV}/c)^2$ resulting from a NLO QCD analysis. Shown are analyses by Blümlein/Böttcher (BB, [44]), Glück et al. (GRSV, [45]) and the Asymmetry Analysis Collaboration (AAC, [46]). The quark distributions and thus also their singlet and non-singlet combinations are well determined. The gluon distribution, however, is hardly constrained.

2.5 Direct Measurement of ΔG

This section will cover the most important approaches to measure the polarised gluon distribution ΔG directly. The possible reactions can be classified by looking at the probe used. Technically feasible at the moment are electromagnetic and strong probes corresponding to experiments where polarised lepton beams are scattered off polarised fixed targets or experiments at polarised pp colliders.

2.5.1 Electromagnetic Probes

In polarised lepton-nucleon scattering the photon-gluon fusion process (PGF) provides direct access to ΔG. In the PGF process (cf. Fig. 2.9) the virtual photon interacts with a gluon from the nucleon via exchange of a virtual quark, resulting in a $q\overline{q}$ pair, that is produced back-to-back in the photon-gluon centre-of-mass (c. m.) frame. There are currently two strategies how to tag this process and thus to enhance it in the data sample. One is the analysis of hadron pairs with high transverse momentum relative to the virtual photon and the other is the use of open charm events. Both strategies are currently used in COMPASS. Since the analyses proceed via the extraction of asymmetries, they are sensitive to the gluon polarisation $\Delta G/G$ as will be shown in the coming sections. Thus in order to extract ΔG one needs a measurement of the unpolarised distribution G from e.g. experiments at HERA.

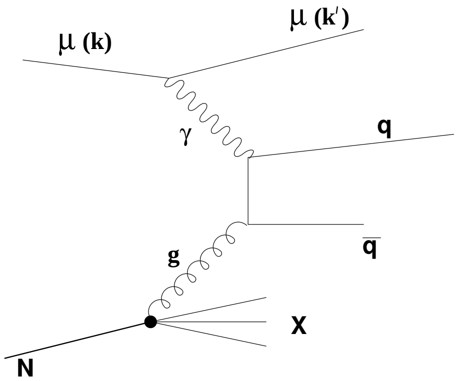

Figure 2.9: Schematic view of the photon-gluon fusion process.

High p_t Hadrons

This approach is mainly based on the assumption that a large transverse momentum (p_t) relative to the photon can only be generated by the PGF and the QCD-Compton processes (cf. Figs. 2.9 and 2.10), whereas in the LO process the quark typically emerges in the direction of the virtual photon. If one in addition assumes that properties of the quarks like direction of motion and flavour are reflected in the properties of the resulting hadrons, the PGF process can be enhanced by cutting on the p_t of the produced hadrons. The remaining

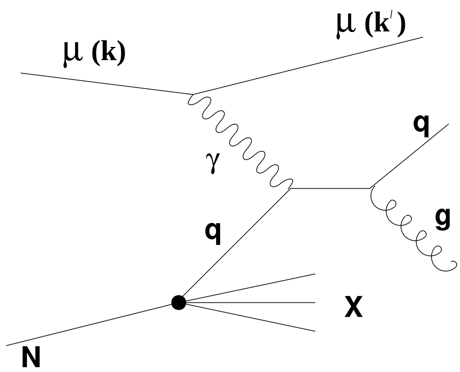

Figure 2.10: Schematic view of the QCD Compton process.

asymmetry contributions of the LO and QCD Compton processes can be calculated and thus be subtracted from the measured asymmetry. In order to be able to correct for the background processes, one needs to know their relative contributions to the data sample. This information is obtained from Monte Carlo simulations which have been tuned to describe the data. For the case of $Q^2 > 1(\mathrm{GeV}/c)^2$ the high-p_t asymmetry is then given by

$$A^{\mu N \to h_1 h_2} = \langle \frac{\Delta G}{G} \rangle \langle a_{\mathrm{LL}}^{\mathrm{PGF}} \rangle R^{\mathrm{PGF}} + \langle A_1 \rangle \langle a_{\mathrm{LL}}^{\mathrm{QCDC}} \rangle R^{\mathrm{QCDC}} + \langle A_1 \rangle \langle a_{\mathrm{LL}}^{\mathrm{LO}} \rangle R^{\mathrm{LO}}, \tag{2.63}$$

where $\langle a_{\mathrm{LL}}^i \rangle$ are the analysing powers of the contributing processes given by the partonic cross-section ratios and R^i are the corresponding relative contributions of the processes to the data sample. The photon-nucleon asymmetry A_1 is introduced by the fact that in the case of QCD Compton and LO processes the photon probes Δq and not ΔG. In order to justify the perturbative treatment of the photon-parton interaction, a hard scale is needed. This scale is provided by the p_t of the process, which is assured to be sufficiently large by asking for a minimum p_t of 1-1.5 GeV/c. COMPASS has analysed the 2002–2003 data and obtained $\Delta G/G = 0.049 \pm 0.296(\mathrm{stat}) \pm 0.105(\mathrm{syst})$, using the described high-p_t approach for $Q^2 > 1(\mathrm{GeV}/c)^2$ [47].

If one extends the analysis to cover the entire Q^2 acceptance of the experiment there is an additional source of background, namely so-called resolved photon events, where the hadronic structure of the photon allows for an interaction with the parton from the nucleon. The information on the polarised parton distributions of the photon is scarce, however, one can deduce limits from the knowledge on the unpolarised distributions and thus calculate the contribution of the resolved photon processes to the measured asymmetry and subsequently subtract. The COMPASS result for this analysis is $\Delta G/G = 0.024 \pm 0.089(\mathrm{stat}) \pm 0.057(\mathrm{syst})$ [48], again for the data of 2002 and 2003.

As a conclusion it should be stressed that the approach of tagging the PGF process via the analysis of high-p_t hadron pairs is statistically favoured compared to the open charm approach covered in the next section. It is, however, strongly model dependent due to the use of Monte Carlo simulations in order to extract the relative contributions of the contributing processes.

Open Charm

In this approach the quark-antiquark pair produced in the PGF process is required to be a $c\bar{c}$ pair. Assuming that due to the large charm-quark mass the intrinsic charm content of the nucleon is negligible and the generation of charm during the fragmentation process is suppressed, the $c\bar{c}$-pair is a clean tag for PGF. In principle the virtual photon could not only interact directly, but also via its hadronic structure, however, these resolved contributions are small for COMPASS energies, as LO estimates have shown [49]. This makes the open charm approach theoretically free of background.

The charm quarks produced in the PGF process subsequently fragment into charmed hadrons. The production of charmonia from PGF is suppressed and in addition the formation of a bound state from the $c\bar{c}$ pair introduces large theoretical uncertainties. Therefore only open charm will be discussed in the following and Tab. 2.1 summarises the corresponding fragmentation probabilities. The PGF events can then be recognised in the detector via the characteristic decay of the charmed hadrons, in the case of COMPASS mainly $D^0 \to K\pi$.

Table 2.1: Summary of the charm fragmentation probabilities. The values are given for a centre-of-mass energy of 10 GeV [6]. Note that the probabilities include all decays into the corresponding hadron, e.g. $D^\star \to D^0\pi$ contributes to the first line.

Hadron	Quark Content	Probability
D^0	$c\bar{u}$	50 %
D^+	$c\bar{d}$	20 %
D_s^+	$c\bar{s}$	20 %
Λ_c^+	udc	10 %

As a proof of principle one can look at the unpolarised case, where the open charm tag has already been used to extract the gluon distribution $G(x)$ from e.g. HERA data. Fig. 2.11 shows the result for $xG(x)$ extracted from a QCD analysis (cf. Chapter 2.4) compared to the distribution extracted from photoproduction data for $D^\star$.

Having established the principle of the open charm approach to extract information about the gluon in the nucleon, it will now be discussed how the measurable asymmetries are related to the gluon polarisation. The photon-nucleon asymmetry is given by

$$A_{\gamma N}^{c\bar{c}} = \frac{\Delta\sigma_{\gamma N \to c\bar{c}}}{\sigma_{\gamma N \to c\bar{c}}} = \frac{\int_{4m_c^2}^{2M\nu} \Delta\hat{\sigma}_{\gamma g \to c\bar{c}}(\hat{s}) \Delta G(\eta, \hat{s}) d\hat{s}}{\int_{4m_c^2}^{2M\nu} \hat{\sigma}_{\gamma g \to c\bar{c}}(\hat{s}) G(\eta, \hat{s}) d\hat{s}}, \tag{2.64}$$

where η is the fraction of the nucleon momentum carried by the interacting gluon. The photon-gluon c.m. energy is given by

$$\hat{s} = (\mathbf{q} + \eta\mathbf{P})^2 \overset{Q^2=0}{\approx} 2\eta\nu M_N. \tag{2.65}$$

The integration limits are given by the production threshold for a $c\bar{c}$ pair and Eq. (2.65) for $\eta = 1$.

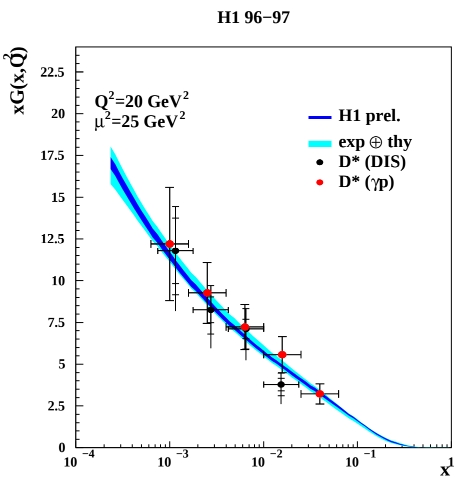

Figure 2.11: The gluon momentum distribution extracted from a QCD analysis compared to the result obtained with an open charm tagging approach. The line ("H1 prel") shows $xG(x)$ as extracted via a QCD fit on NMC and H1 data, error bands taking into account theoretical and experimental uncertainties are indicated. The points are obtained from a $D^\star$ meson cross-section measurement by the H1 collaboration. For the DIS measurement $Q^2 > 2\,(\mathrm{GeV}/c)^2$ was required, whereas for the photoproduction (γp) $Q^2 < 0.01\,(\mathrm{GeV}/c)^2$ was used [50].

The interpretation of the muon beam as a source of photons leads to the following factorisation of the muon-nucleon cross section [1]

$$\frac{d^2\sigma_{\mu N\to c\bar{c}}}{dQ^2 d\nu} = \Gamma(E, Q^2, \nu)\sigma_{\gamma N\to c\bar{c}}(Q^2, \nu), \tag{2.66}$$

with the virtual photon flux

$$\Gamma(E, Q^2, \nu) = \frac{\alpha}{2\pi}\frac{2(1-y)+y^2+Q^2/2E^2}{Q^2(Q^2+\nu^2)^{1/2}}. \tag{2.67}$$

Since this flux behaves like $1/Q^2$ for small Q^2 and finite ν, it is important to make use of the entire photon spectrum, even down to quasi-real photons with $Q^2 \to 0$. This requirement strongly influences the design of the spectrometer, such as the detector components for the detection of the scattered muon and the trigger system.

The perturbative treatment of the cross sections is in the case of quasi-real photons justified by the hard scale given by the production threshold of the $c\bar{c}$ pair, which is $4m_c^2$. Eq. (2.64) can be modified such that it reads

$$A^{c\bar{c}}_{\gamma N} = \frac{\Delta\sigma_{\gamma N\to c\bar{c}}}{\sigma_{\gamma N\to c\bar{c}}} = \frac{\int_{4m_c^2}^{2M\nu}\hat{a}_{\mathrm{LL}}\frac{\Delta G(\eta,\hat{s})}{G(\eta,\hat{s})}\hat{\sigma}_{\gamma g\to c\bar{c}}(\hat{s})G(\eta,\hat{s})d\hat{s}}{\int_{4m_c^2}^{2M\nu}\hat{\sigma}_{\gamma g\to c\bar{c}}(\hat{s})G(\eta,\hat{s})d\hat{s}} \tag{2.68}$$

$$= \langle\hat{a}_{\mathrm{LL}}\frac{\Delta G}{G}\rangle, \tag{2.69}$$

thus giving a relation between the photon-nucleon asymmetry and $\Delta G/G$, where the partonic (photon-gluon) asymmetry is defined as

$$\hat{a}_{\mathrm{LL}} = \frac{\Delta\hat{\sigma}_{\gamma g\to c\bar{c}}}{\hat{\sigma}_{\gamma g\to c\bar{c}}}. \tag{2.70}$$

The partonic cross sections in the limit $Q^2 \to 0$ are given in LO as [51]

$$\Delta\hat{\sigma}_{\gamma g\to c\bar{c}}(\hat{s}) = \frac{4}{9}\frac{2\pi\alpha\alpha_s(\hat{s})}{\hat{s}}\left(3\beta - \ln\frac{1+\beta}{1-\beta}\right) \tag{2.71}$$

$$\hat{\sigma}_{\gamma g\to c\bar{c}}(\hat{s}) = \frac{4}{9}\frac{2\pi\alpha\alpha_s(\hat{s})}{\hat{s}}\left(-\beta(2-\beta^2) + \frac{1}{2}(3-\beta^4)\ln\frac{1+\beta}{1-\beta}\right), \tag{2.72}$$

with $\beta = \sqrt{1-4m_c^2/\hat{s}}$.

These cross sections and the partonic asymmetry are shown in Fig. 2.12 as functions of $\hat{s}$. A small partonic asymmetry results in a small photon-nucleon asymmetry and thus makes it difficult to extract the gluon polarisation. The fact that the partonic asymmetry changes sign is therefore a motivation to use it in the event weight later on in the analysis.

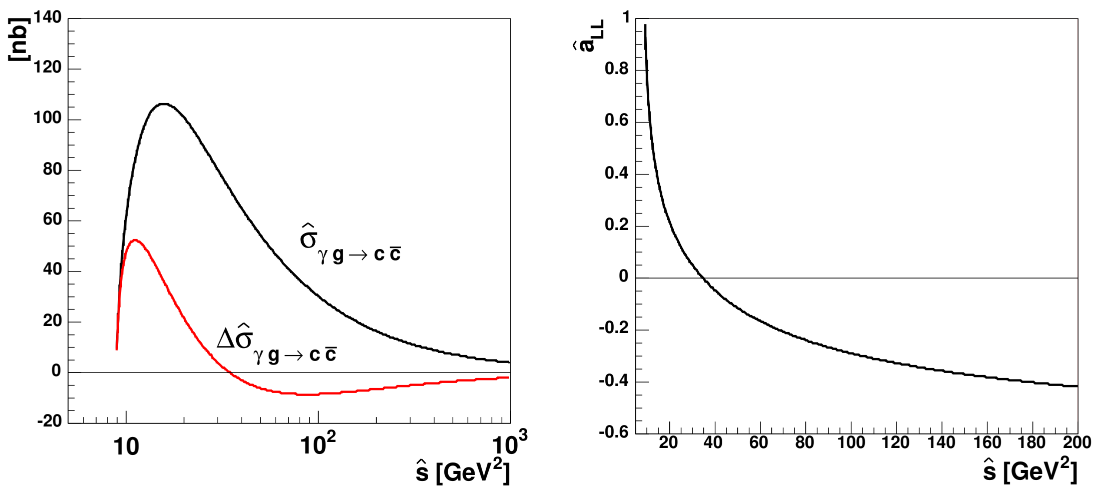

Figure 2.12: Spin-averaged and spin-dependent partonic cross sections (left) and partonic asymmetry (right) as functions of the photon-gluon c.m. energy $\hat{s}$ for $m_c = 1500\,\mathrm{GeV}/c^2$. COMPASS kinematics yield $\langle\hat{s}\rangle \approx 21$ GeV^2.

The photon-nucleon asymmetry $A_{\gamma N}^{c\bar{c}}$ is related to the measured counting-rate asymmetry A^m via several 'diluting' factors

$$A^m = \frac{N_{c\bar{c}}^{\overset{\leftarrow}{\Rightarrow}} - N_{c\bar{c}}^{\overset{\rightarrow}{\Leftarrow}}}{N_{c\bar{c}}^{\overset{\leftarrow}{\Rightarrow}} + N_{c\bar{c}}^{\overset{\rightarrow}{\Leftarrow}}} = P_\mu P_t f D A_{\gamma N}^{c\bar{c}}. \tag{2.73}$$

The depolarisation factor D was already introduced in Eq. (2.22), P_μ and P_t are the beam and target polarisations and f is the dilution factor, which takes into account interactions in unpolarisable material in the target.

The main part of this thesis is devoted to the extraction of the gluon polarisation from the COMPASS data by using the open charm approach. More details on the reconstruction of the charmed hadrons and the actual extraction of $\Delta G/G$ will be given in Chapters 5 and 6, the final result is presented in Chapter 7.

2.5.2 Strong probes

The polarised proton beams at RHIC (BNL) provide the opportunity to extract ΔG by using the partons of one proton as a probe of the gluons in the other. Here the main processes are the prompt photon production and the jet production.

In the case of prompt photon production the desired process is $qg \to \gamma q$, whereas the process $q\bar{q} \to \gamma g$ contributes as background (cf. Fig. 2.13). The latter, however, is suppressed to 10 % due to the small intrinsic $\bar{q}$ content of the proton. In the case of jet production the process in question is $gq \to gq$ and $gg \to gg$ (cf. Fig. 2.14 (a) and (b)). In addition to that there is the possibility to study heavy flavour production $gg \to q\bar{q}$.

As opposed to the clean photon probe of the lepton-nucleon scattering covered in the last section, there are now parton densities on both sides of the reaction, resulting in a measurement that is sensitive only to a convolution of the gluon density and another parton density. For example in the case of prompt photon production the measured double spin asymmetry is given as

$$A_\parallel \propto \hat{a}(qg \to \gamma g)\frac{\Delta G}{G}\frac{\sum_i e_i^2 \Delta q_i}{\sum_i e_i^2 q_i}. \tag{2.74}$$

The measurement of ΔG at RHIC is based on the mentioned processes [52] and is performed as part of the STAR and PHENIX experiments.

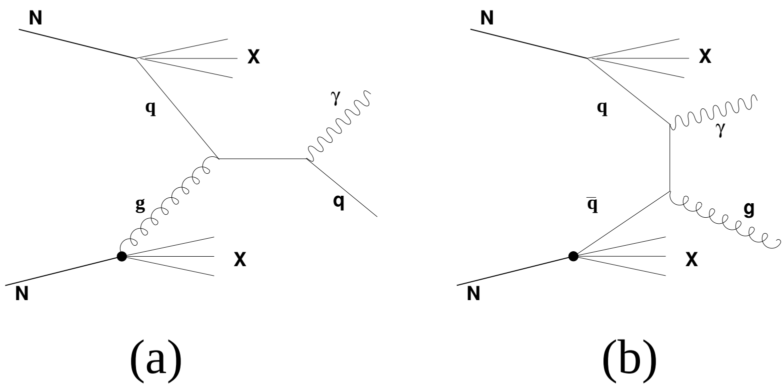

Figure 2.13: Schematic view of the prompt photon production (a) and the background process (b).

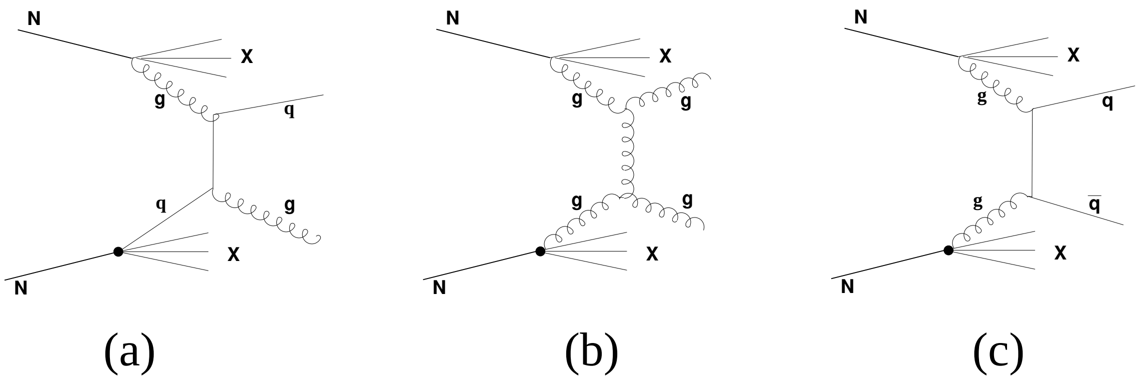

Figure 2.14: Schematic view of the jet production ((a) and (b)), as well as the heavy flavour production (c) in pp reactions.

Chapter 3

The COMPASS Experiment

This chapter is dedicated to the setup of the COMPASS experiment. After covering the prerequisites of polarised DIS, namely the polarised beam and the polarised target in Sec. 3.1 and Sec. 3.2, the design principle of the spectrometer will be discussed in Sec. 3.3 along with its most important components. The depth at which they will be covered varies with their importance for the analysis described in the following chapters. In the open-charm analysis the data from the years 2002 to 2004 are used and it is therefore interesting to know the changes in the spectrometer during this period. This will be subject of Sec. 3.3.4. There are many overviews on the COMPASS spectrometer [5,53–55], which can be consulted for details in addition to the references explicitly given in the text.

3.1 The Beam

The COMPASS experiment is situated at the end of the M2 beamline of the SPS* at CERN. This beamline can be adjusted to deliver muon as well as hadron beams, which makes the rich physics programme of COMPASS possible. In the following this beamline will be described as it is used for the measurements with muon beam. For more details see [5, 56].

The muon beam supplied by the M2 beamline (cf. Fig. 3.1) is a tertiary beam, originating from the protons accelerated in the SPS up to 400 GeV. These protons are extracted from the SPS into M2 during 4.8 s in a 16.8 s cycle leading to the so-called spill structure of the beam. The secondary beam of mainly pions and kaons is produced by the proton beam in the T6 production target. The length of this beryllium target can be varied in order to adjust the intensity of the resulting beam. For a subsequent nominal intensity of $2.8 \cdot 10^8 \mu^+$/spill a target length of 500 mm is used. A setup of dipole magnets and scrapers selects pions and kaons in a given momentum interval. Most of these pions and kaons then decay into muons while travelling through the following 600 m long section of the beam line. After removing the remaining pions and kaons in a hadron absorber the tertiary muon beam is momentum selected and transported to the COMPASS hall at ground level.

*Super Proton Synchrotron

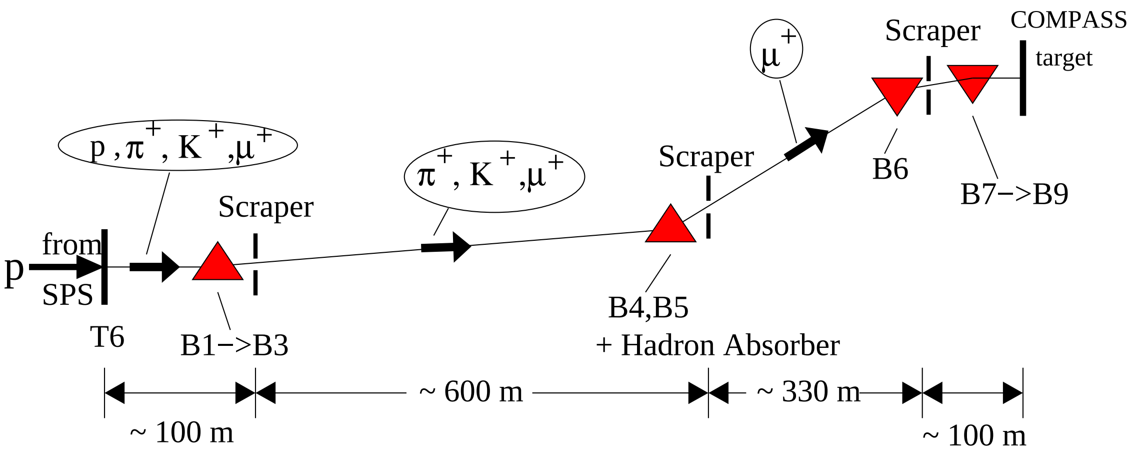

Figure 3.1: The M2 beamline providing the COMPASS experiment with a tertiary muon beam. The secondary beam of mostly charged pions and kaons is produced at the T6 target, which is impinged by the SPS proton beam. At the end of the decay tunnel the remnants of the secondary beam are filtered out by the hadron absorber housed in the B4 dipole setup, resulting in a clean muon beam.

One of the dipole setups which steer the beam towards COMPASS is used together with the Beam Momentum Stations as a spectrometer to determine the momentum of the beam on an event-by-event basis. The detectors of this setup will be described in Sec. 3.1.1 and the principle of reconstruction will be covered in Chapter 4. The muon beam, which finally arrives at the COMPASS target, has a momentum of $p_\mu = 160\,\mathrm{GeV}/c$ with a spread of 3 %.

Owing to the parity violating nature of the pion (kaon) decay the muon beam is naturally longitudinally polarised. The polarisation of the muon in the lab frame is determined by the kinematics of the muon and its parent particle

$$P_\mu = -\frac{m_{\pi,K}^2 + (1 - \frac{2E_{\pi,K}}{E_\mu})m_\mu^2}{m_{\pi,K}^2 - m_\mu^2}, \tag{3.1}$$

where E_i and m_i ($i \in \{\pi, K, \mu\}$) are the energies and masses of the pion, kaon and muon, respectively. The momentum selection of the pions/kaons and the resulting muons thus makes it possible to adjust the polarisation of the muon beam.

A parametrisation of the polarisation as a function of the momentum is obtained from a Monte Carlo simulation of the beamline. During the years 2002 and 2003 the momentum of the secondary pions and kaons was selected to be $p_{\pi,K} = 177\,\mathrm{GeV}/c$ resulting in an average muon polarisation of $\langle P_\mu \rangle = -0.76$. In 2004 the selected momentum was $p_{\pi,K} = 172\,\mathrm{GeV}/c$ yielding a 7 % larger polarisation of $\langle P_\mu \rangle = -0.81$. The corresponding parametrisations of the polarisation as a function of the momentum are shown in Fig. 3.2. Making use of the knowledge of the momentum of the beam muon the polarisation is thus available on an event-by-event basis. The polarisation, which enters in the analysis as a diluting factor (cf. Eq. (2.73)), can thus be used in a weighting of the events.

The M2 beamline has already been used by the SMC. During that time the polarisation of the muon beam was measured [57, 58] and the result was found to agree well with the

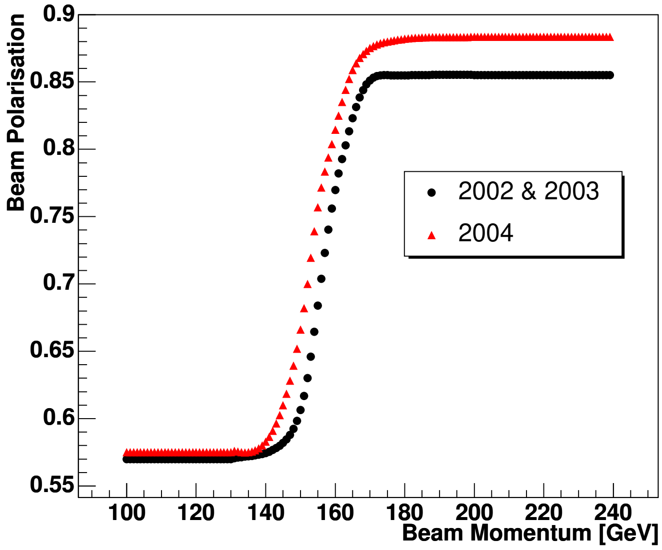

Figure 3.2: The beam polarisation as obtained from a parametrisation as a function of the beam momentum. The circles show the situation during the data taking of 2002 and 2003, where $p_{\pi,K} = 177\,\mathrm{GeV}/c$. During 2004 $p_{\pi,K} = 172\,\mathrm{GeV}/c$ was used, resulting in a increased beam polarisation (triangles).

Monte Carlo simulations. Based on this cross check it was decided that the parametrisation of the polarisation obtained from Monte Carlo is sufficient for COMPASS.

The most important parameters of the beam are summarised in Tab. 3.1. It should be pointed out that the values for the beam diameter give the dimensions of the gaussian core of the beam. In addition to this core there is a considerable amount of beam halo, which constitutes an important source of background.

Table 3.1: Summary of the beam parameters.

proton rate at T6 / spill	$1 \cdot 10^{13}$
muons / spill	$2 \cdot 10^{8}$
beam momentum $\langle p_\mu \rangle$	$160\,\mathrm{GeV}/c$
beam polarisation $\langle P_\mu \rangle$	-0.76 (-0.81)
beam diameter at target ($\sigma_\mathrm{x} \times \sigma_\mathrm{y}$)	$8 \times 8\,\mathrm{mm}^2$

3.1.1 Beam Momentum Station

The Beam Momentum Station (BMS) setup is situated at about 100 m upstream of the COMPASS target. It takes advantage of the deflection of the beam in the field of the B6 dipole magnet in order to measure the momentum of the beam on an event-by-event basis.

The BMS setup consists of two telescopes installed upstream and downstream of the B6 magnet (cf. Fig. 3.3). Each telescope originally consisted of two hodoscope planes composed of scintillator elements of 5 mm pitch and 20 mm thickness [56]. Since the association of information from the BMS setup and the beam measuring detectors in the spectrometer heavily relies on time correlation, an excellent time resolution is required. For the original planes it was found to be 262 ps [5]. This setup was supplemented in 2003 by a fifth station BMS05, a plane similar to the Scintillating Fibre planes used in the spectrometer. The geometry of this plane is similar to that of the original planes apart from the 2.5 mm pitch. The plane is mounted half-way in between the stations BMS01 and BMS02. However, the impact of this station on the reconstruction is limited (cf. Chapter 4) due to its time resolution of about 900 ps, related to problems with the photomultiplier used [59].

For the data taking of 2004 there were further modifications to the setup. Due to the age of the original BMS setup[†] spare parts for the front-end electronics were no longer available. This lead to a refurbishment of the electronics of stations BMS01 to BMS04 according to the COMPASS philosophy of digitising as close to the detector as possible. As a side-effect the timing is more stable in this configuration compared to the situation before, where a strong temperature dependence was caused by long cables between the BMS setup and the readout hut. In addition to the changes in electronics an additional station called BMS06 was mounted between the stations BMS03 and BMS04. This station is made of scintillating fibres just like BMS05 and also its dimensions are equal to those of station BMS05, except for the pitch of 1.25 mm resulting in 128 channels. The two stations use the same multi-anode photomultiplier technology, whose performance has been improved considerably compared to 2003.

3.2 The Polarised Target

The high luminosity needed for the physics programme of the COMPASS experiment is achieved by using thick solid state targets. The target material that is used for the measurements of the spin structure of the proton and the deuteron are NH_3 and ^{6}LiD, respectively. The combined knowledge on proton and deuteron can then be used to extract information on the spin structure of the neutron. So far the COMPASS experiment has taken data with the ^{6}LiD target material. Since ^{6}Li can be interpreted as consisting of an unpolarisable alpha particle and a deuteron, the polarisable fraction is large making ^{6}LiD an efficient deuteron target (cf. Eq. (2.73)).

The polarisation of the target material is achieved using the technique of dynamic nuclear polarisation (DNP) [60], where the polarisation of impurity electrons is transferred to the polarisable nucleons. The low temperatures and strong magnetic fields needed for the DNP are provided by a complex setup of a cryostat and superconducting magnets (cf. Fig. 3.4). The setup used by COMPASS so far corresponds to the one also used by SMC and will now be described in more detail. For the data taking of 2006 onwards the use of a magnet system with larger acceptance (180 mrad instead of 70 mrad) is planned.

[†]The BMS was used already by the EMC in the 1980s.

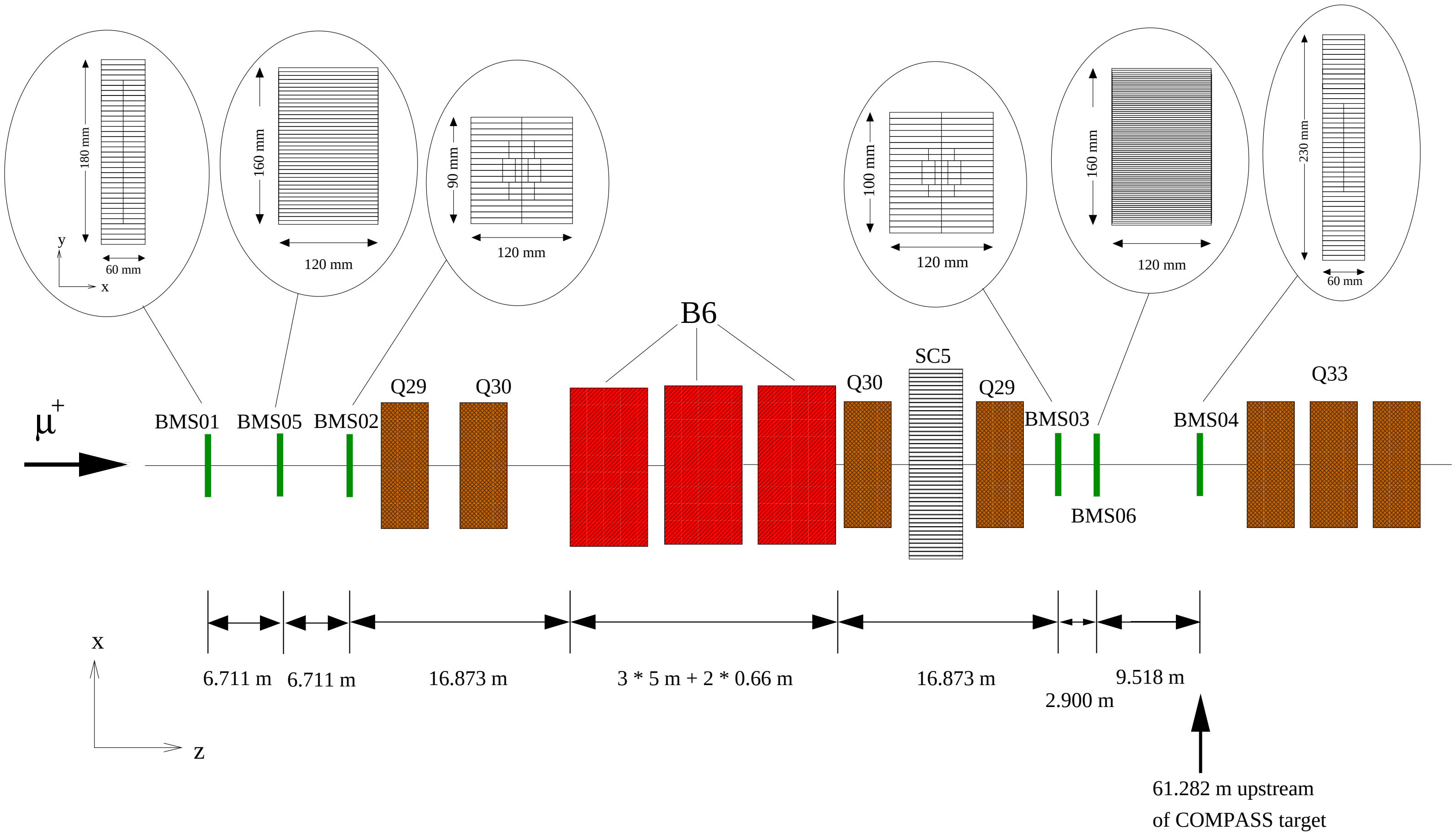

Figure 3.3: Schematic view of the setup of the Beam Momentum Stations (BMS) around the B6 magnet group of the M2 beamline. The purpose of the setup is to determine the momentum of the beam muons by measuring their deflection in the field of the three bending dipole magnets of B6. The elements marked with "Qi" are quadrupole magnets, whereas SC5 is a scraper. (The plot is not to scale)

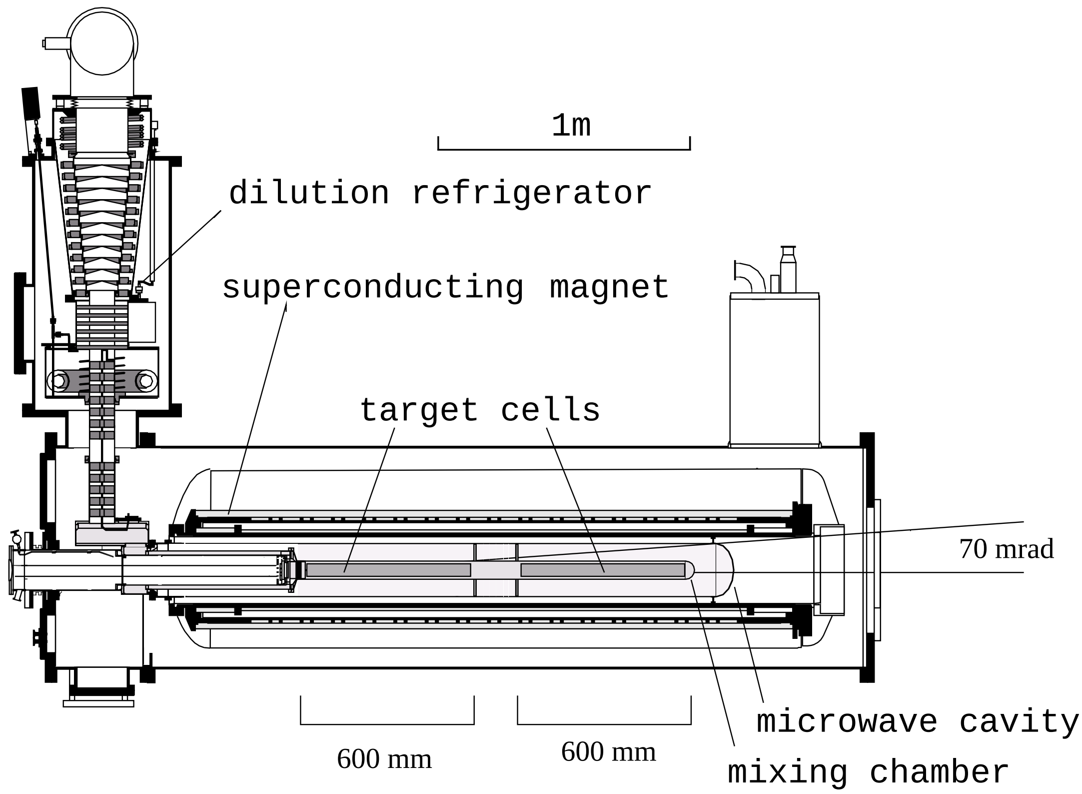

Figure 3.4: The SMC target setup, as used by COMPASS so far, consisting of the dilution refrigerator and the magnet system, which contains the microwave cavity and the mixing chamber. The dimensions of the target cells are indicated.

The target material is contained in two oppositely polarised cylindrical target cells of 60 cm length and 3 cm diameter, which are installed one after the other along the beam inside the mixing chamber of a ^{3}He-^{4}He dilution refrigerator. This means that the two target cells are exposed to the same muon flux, making the measured asymmetries independent of the flux and thus avoiding possible false asymmetries due to variations of the beam flux. The target cells are labelled according to their position relative to the beam direction as upstream and downstream cell.

During the DNP the dilution refrigerator provides a temperature of about 0.4 K. As soon as the desired polarisation is achieved, the polarising process is stopped and the spin configuration is frozen by cooling the target material to 50 mK. One can then take advantage of the long relaxation time, which exceeds 1000 h. The mixing chamber is situated inside the microwave cavity which provides the necessary radiation for the DNP. There is a separate microwave system for each of the two target cells, since for opposite polarisations two different microwave frequencies are needed. The two target cells are separated by a 10 cm gap in which a microwave stopper prevents radiation intended for one cell from leaking into the other one. Another reason for the separation is to make sure that later on in the analysis of the data the primary vertices can be safely attributed to one of the target cells. The polarisation is constantly monitored by five NMR-coils along each of the cells. Typical polarisations are about 50 %, which can be seen from Fig. 3.5, where the average cell polarisation is plotted for the years 2002 to 2004.

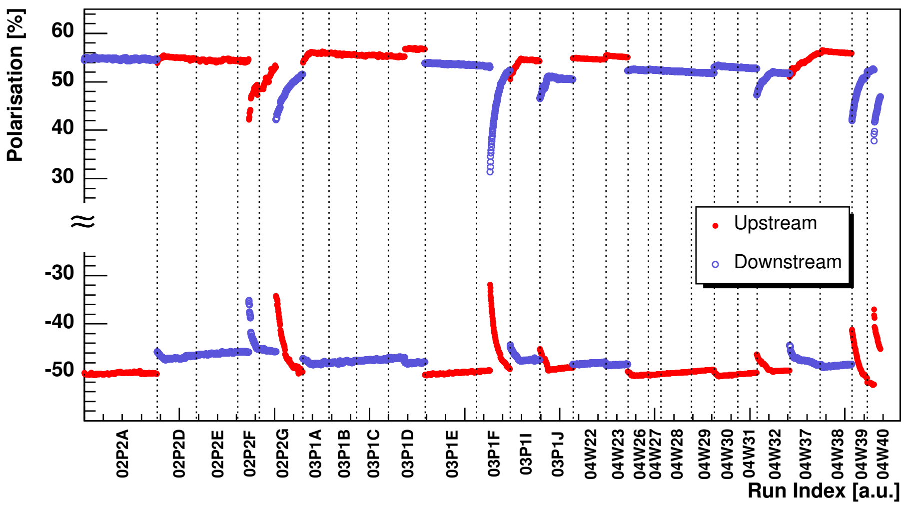

Figure 3.5: The average cell polarisation for the years 2002 to 2004 plotted for each run which is used in the analysis of this thesis. The data-taking periods are indicated. One period typically corresponds to one week. The average polarisation achieved was about 50 %.

The magnet system consists of a solenoid and a dipole magnet. The strong longitudinal field of about 2.5 T necessary for the polarisation is supplied by the solenoid magnet with a relative homogeneity of about $\pm 2 \cdot 10^{-5}$ [15]. In order to reduce false asymmetries due to acceptance effects, it is possible to rotate the target-spin orientation (cf. Fig. 3.6). This is done by superimposing the field of the dipole magnet on the partially ramped down longitudinal field [15]. The rotation of the spin configuration is done 2-3 times a day. Possible systematic effects correlated to the direction of the solenoid field are suppressed by reversing the target spins by means of the microwave setup leading to a reversed relative orientation of the target spin and the longitudinal field (cf. Fig. 3.6). This, however, is a lengthy procedure of about two days, since it involves the loss of polarisation and thus a subsequent repolarisation. Therefore this is done only about once per month.

3.3 The COMPASS Spectrometer

The COMPASS experimental setup consists of a two-stage forward magnetic spectrometer optimised for high rates and large angular and dynamic acceptances, which are requirements for all aspects of the proposed physics programme and the muon programme in particular. In the proposed final setup of the experiment both stages will be fully equipped with spectrometer magnets, tracking, particle identification via Ring Imaging Čerenkov counter (RICH), electromagnetic and hadronic calorimetry and muon identification. Com-

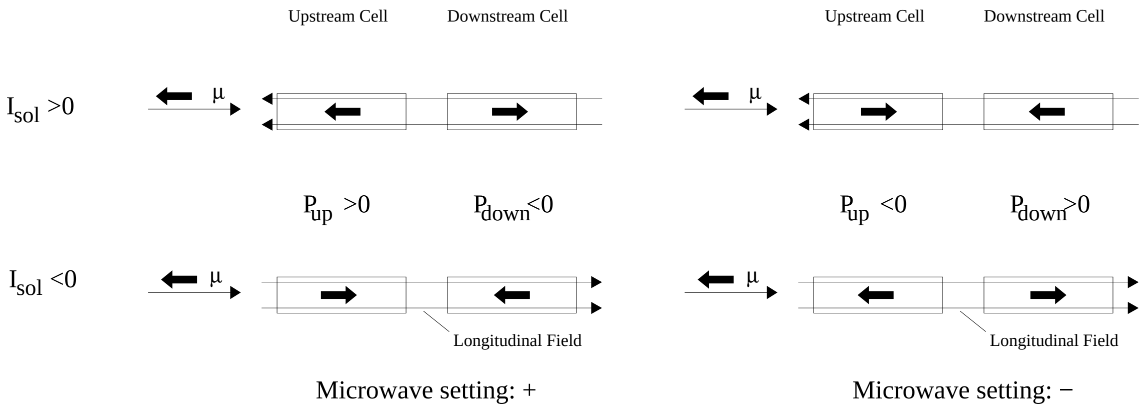

Figure 3.6: Schematic view of the different longitudinal spin configurations. Shown is the situation corresponding to the different microwave settings, where a given setting gets its label corresponding to the sign of the upstream polarisation. The orientations of the field of the solenoid magnet is indicated along with the corresponding sign of the current in the magnet I_{sol}. The sign of a given polarisation is relative to the solenoid field orientation, i.e. parallel orientation of polarisation and field means positive sign. The situations on the top and on the bottom of the plot correspond to the orientations before and after a solenoid field reversal.

pared to this final scenario, the setup used for data taking up to now (cf. Fig. 3.7) is lacking part of the setup for the electromagnetic calorimetry and the RICH of the second spectrometer stage.

The reason to use a two-stage setup is to optimise the momentum resolution, which is especially important for the open charm approach to measure $\Delta G/G$ due to the fact that the charmed meson can only be identified via its invariant mass. The large angle spectrometer, which makes up the first stage, is meant for the detection of tracks with angles up to about 180 mrad and low momenta, whereas the small angle spectrometer covers the angular acceptance range smaller than 30 mrad and is used for the reconstruction of high momentum tracks.

The fact that the two stages are similar in their setup implies that also the principle of measurement and reconstruction is the same for the two. The momentum of detected particles is measured via their deflection in the fields of the spectrometer dipole magnets (SM), which have a bending power of 1.0 Tm and 4.4 Tm, respectively. The deflection is detected with tracking stations installed upstream and downstream of the magnets. More details on these detectors are given in Sec. 3.3.1.

The hadrons in the final state of the reaction can be identified by measuring their velocity with the RICH. This information, combined with the momentum measurement, gives access to the mass of the particle and therefore its identity. Since the hadronic calorimeters (HCAL) absorb most of the particles whose energy they are to measure, they are installed in the rear part of each of the spectrometer stages. Muons are identified with the μFilter setups, which conclude each stage. The particles with large momenta and small angles are able to cross the first spectrometer through holes in the calorimeters and the μFilter. The μFilter of the second stage is followed by detectors needed for the trigger, which will be described in more detail in Sec. 3.3.3.

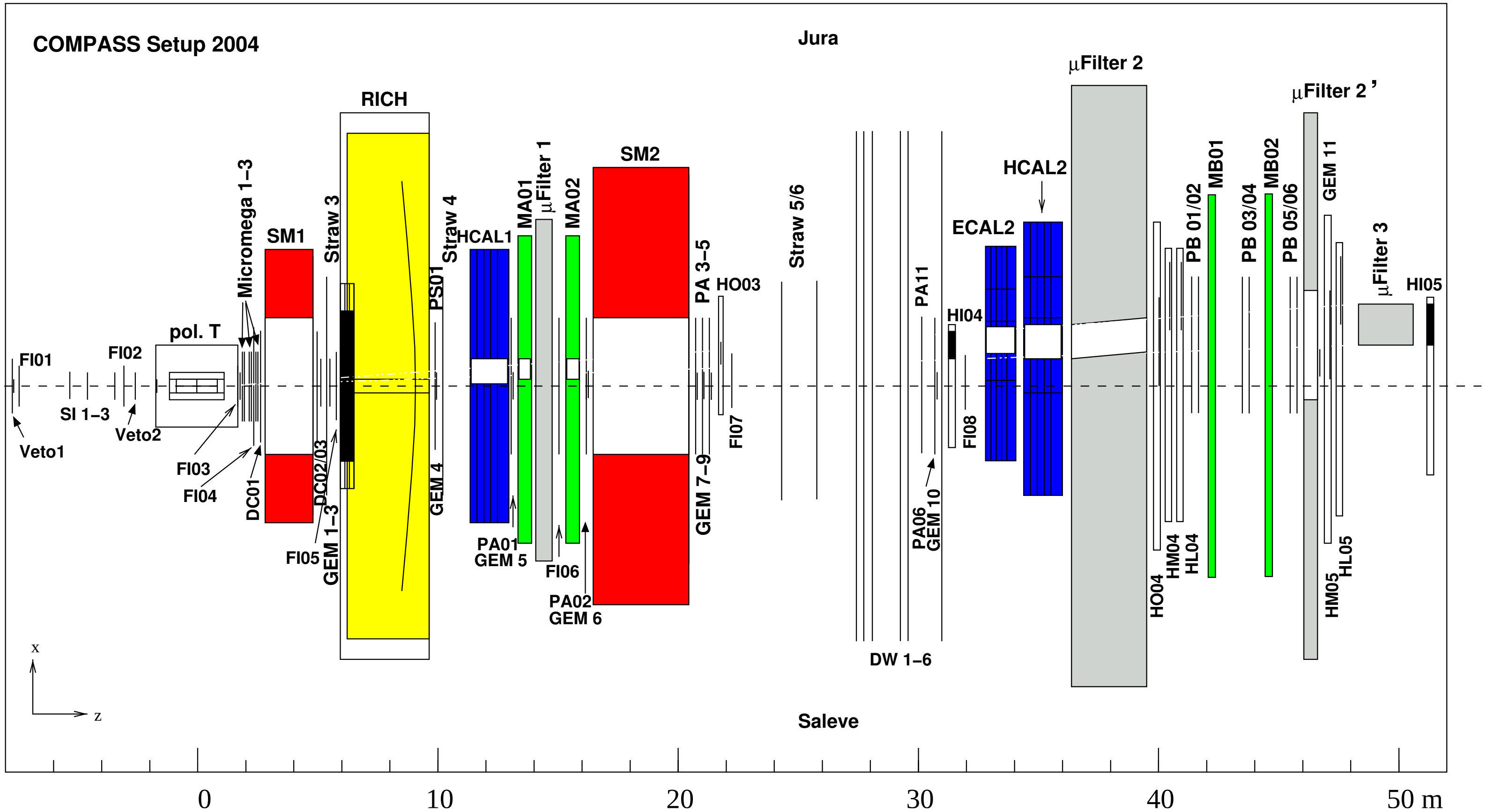

Figure 3.7: The COMPASS spectrometer during the 2004 data taking. The polarised muon beam enters from the left, is detected by the pre-target SciFi/Silicon Microstrip telescope and impinges on the polarised target. The remnants of the reaction in the target are detected with the two-stage spectrometer. The large angle spectrometer, which makes up the first stage, is meant for the detection of tracks with angles up to 180 mrad and low momenta, whereas the small angle spectrometer covers the kinematic range of angles smaller than 30 mrad and large momenta. In the COMPASS main reference system (CMRS) the x-axis points towards the Jura, the y-axis points upwards and the z-axis points along the direction of the beam. The MWPCs are denoted as PS, PA or PB depending on their position, the W4-5 planes as DW and the tracking detectors belonging to μFilter1 (μFilter2) are denoted as MA (MB). (The plot is not to scale in the x-direction)

3.3.1 Tracking Detectors

The purpose of tracking detectors is to sample the track of a charged particle at discrete points along the spectrometer. One plane of a tracking detector typically measures the impact of a particle along the coordinate perpendicular to its wire or fibre direction. This means that for one space point at least two planes are needed. In order to be able to sort out ambiguities, often additional projections to the typical x and y planes are measured.

The required characteristics of a tracking detector vary with its position in the spectrometer and the angular acceptance it is to cover. A detector meant to detect particles which travel through the setup under very small angles is likely to be exposed to the high intensity of the beam, whereas a detector meant for the large angle coverage does not need to be designed for such high rates. In addition to that, a detector mounted upstream of SM1 is exposed to all the low energy debris produced in the reaction, which is then swept away by the magnetic fields of the spectrometer magnets and thus does not reach the detectors further downstream. The tracking detectors used in COMPASS can be classified in three groups, according to their acceptance, as summarised in Tab. 3.2.

Table 3.2: Summary of the different classes of tracking detectors, which are characterised by the angular acceptance covered. Abbreviations are used for Scintillating Fibres (SciFi), Micro Mesh Gas detector (Micromega), Gas Electron Multiplier detectors (GEM) and Multi Wire Proportional Chambers (MWPC).

Very small angles	SciFi, Silicon Microstrips
Small angles	Micromega, GEM
Large angles	Drift Chamber, Straw Tubes, MWPC

The rate that a gaseous detector can stand is limited by the space charge caused by the ions, which drift only very slowly. In order to be able to use gaseous detectors in relatively high rate areas, COMPASS takes advantage of new developments, namely the Micro Mesh Gas detector (Micromega) and the Gas Electron Multiplier (GEM). Both approaches are based on the idea to limit the distance between the volume where the amplification takes place and the cathode. This effectively limits the drift time of the ions and subsequently makes the detector capable of standing higher rates. In case of the Micromega the amplification takes place in the volume between the micro mesh and the anode strips, which are separated by 0.1 mm (cf. Fig. 3.8, left). The GEM detector is constructed in such a way that the amplification takes place only in the holes of the GEM foil (cf. Fig. 3.8, right). In addition to an improved high-rate capability (up to $450\,\mathrm{kHz/cm^2}$ [61]) these designs result in a reasonable time resolution of about 9 ns and 12 ns in the case of Micromegas and GEMs, respectively.

One complete tracking station in the COMPASS spectrometer typically consists of one detector from each of the three categories. In front of SM1 Scintillating Fibres and Silicon Microstrip detectors cover the beam area as well as the very small angles. The tracking in that region is completed by Micromegas and Drift Chambers for the small and the large angles. For the remaining part of the large angle spectrometer GEM detectors replace the Micromegas and there are Straw Tube detectors as a supplement to the Drift Chambers. In

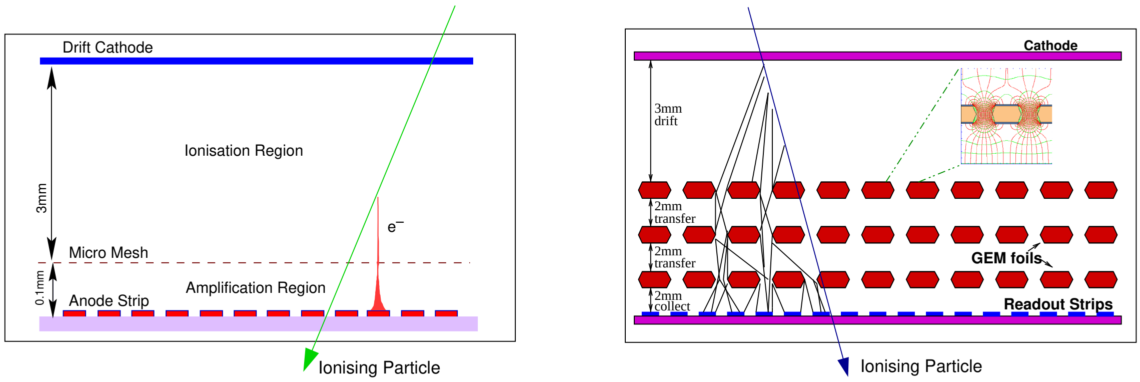

Figure 3.8: Schematic view of Micromegas (left) and GEMs (right). In both cases traversing particles ionise the gas atoms. In case of the Micromega detector the amplification takes place between the mesh and the anode strips, whereas in the case of the GEM detector it takes place in the holes of the GEM foil. These designs are the basis for the capability of these detector types to stand relatively high rates.

the small angle spectrometer Scintillating Fibres and GEM detectors are again used for the very small and the small angles, whereas now the large angles are covered by Multi Wire Proportional Chambers (MWPC), Straw Tubes and Large Area Drift Chambers (W4-5). The properties of the tracking detectors used in COMPASS are summarised in Tab. 3.3 along with references to sources of further details.

3.3.2 Detectors for Particle Identification

Ring Imaging Čerenkov Counter (RICH)

A charged particle crossing a medium with a speed greater than the speed of light in that medium radiates photons according to the Čerenkov effect. The photons are emitted under an angle θ_C relative to the direction of motion of the particle

$$\cos\theta_C = \frac{1}{n\beta} = \frac{1}{n}\sqrt{1+\frac{m^2c^2}{p^2}}, \tag{3.2}$$

where n is the refractive index of the medium crossed by the particle and β is the velocity v/c. From Eq. (3.2) the threshold condition for the Čerenkov effect can be deduced:

$$\beta \geq \frac{1}{n}. \tag{3.3}$$

A RICH takes advantage of the Čerenkov effect in order to identify charged particles. Knowing their momenta from a measurement in the spectrometer, one can deduce their mass from the measured Čerenkov angle (cf. Eq. (3.2)), provided the momentum is above the Čerenkov limit. For growing momenta the Čerenkov angle approaches the asymptotic limit $\cos\theta_C = 1/n$ and it becomes more and more difficult to separate the different particle types, thus a given setup has a design limit up to which the particle identification is expected to work reasonably. In the case of COMPASS the radiator material is C_4F_{10} gas

Table 3.3: The most important properties of the tracking detectors used in COMPASS. In some cases the values for active areas and dead zones vary, depending on the position in the spectrometer. In case of the drift detectors the information on space and time resolution is not independent, since the latter is used in the extraction of the space information. The values for the time resolution are therefore not given. Further details can be found in: SciFi [55, 62, 63], Silicon Microstrip [64], Micromega [61], GEM [65, 66], Drift Chamber [67, 68], Straw Tubes [69, 70], MWPC [53], W4-5 [71].

Detector Type	Active Area	Dead Zone	Time Resolution	Space Resolution	Projections
SciFi (target region)	$39.4\times39.4\,\mathrm{mm}^2$- $52.5\times52.5\,\mathrm{mm}^2$	–	430 ps	120 μm	0°,45°,90°
SciFi (spectrometer)	$84\times84\,\mathrm{mm}^2$- $123\times123\,\mathrm{mm}^2$	–	370 ps	200 μm	0°,±45°,90°
Silicon Microstrip	$70\times50\,\mathrm{mm}^2$	–	3 ns	14 μm	0°,±5°,90°
Micromega	$380\times380\,\mathrm{mm}^2$	Ø5 cm	9 ns	70 μm	0°,±45°,90°
GEM	$300\times300\,\mathrm{mm}^2$	Ø5 cm	12 ns	70 μm	0°,±45°,90°
Drift Chamber	$140\times124\,\mathrm{cm}^2$	Ø30 cm	–	220 μm	0°,±20°,90°
Straw Tube	$325\times277\,\mathrm{cm}^2$	$23\times16\,\mathrm{cm}^2$	–	250 μm	0°,±10°,90°
MWPC	$150\times120\,\mathrm{cm}^2$	Ø16 cm- 22 cm	–	500 μm	0°,±10°,90°
W4-5	$552\times262\,\mathrm{cm}^2$	Ø0.5 m-1 m	–	1900 μm	0°,±30°,90°

with a refractive index of $n_{\mathrm{C_4F_{10}}} = 1.00153$ at 1 bar and 20 °C. Under these conditions the threshold momenta for pions, kaons and protons are 2.5 GeV/c, 8.9 GeV/c and 16.9 GeV/c, respectively. The mentioned design limit is about 50 GeV/c. For the open charm analysis the RICH is used to identify the kaons resulting from the decay of charmed mesons. The expected momentum distribution for the kaons from the channel $D^0 \rightarrow K\pi$ is shown in Fig. 3.9 along with the kinematic acceptance of the RICH. It can be deduced from the plot that roughly 80 % of the kaons are in the momentum acceptance of the RICH.

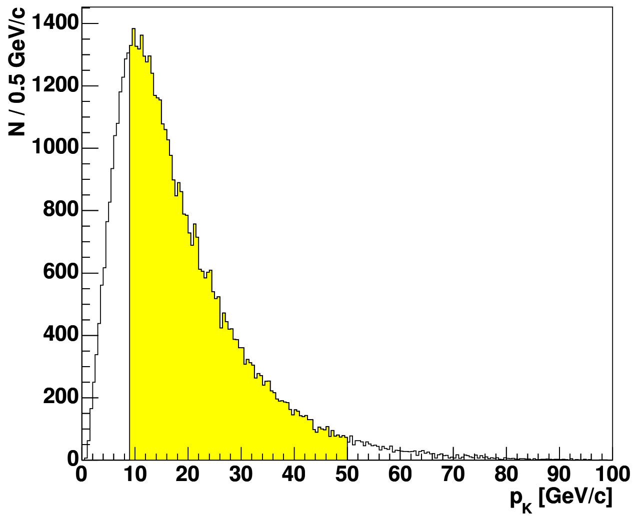

Figure 3.9: The reconstructed momentum of the kaons from the decay of the D^0 extracted from a Monte Carlo simulation. The filled area shows the momentum acceptance of the RICH.

The intensity of Čerenkov photons emitted by a given particle increases with decreasing photon wavelength and it is thus useful to design a system which works in the very ultra-violet (VUV) range ($\lambda_C > 150$ nm). This has implications for all components of the setup. The Čerenkov photons typically have to travel several meters through the radiator gas, thus the gas has to be as transparent as possible. Crucial is the absence of O_2 and H_2O contaminations, because of their large absorption cross section in the VUV range. The goal is to keep their contributions below 5 ppm [72]. The photons produced in the radiator are reflected by two spherical mirror systems [73] and focused onto photon detectors (cf. Fig. 3.10). The centres of the spheres are vertically displaced in order to be able to focalise outside the spectrometer acceptance. This means that the photon detectors can be installed such that they are shielded by SM1. Since parallel rays are focused into one point by the mirror system, the photons emitted by a given particle give a ring in the plane of the photon detectors. The radius of this ring is related to the focal length $f = R_m/2$ of the mirror-system and the Čerenkov angle

$$r = \theta_C \frac{R_m}{2} \tag{3.4}$$

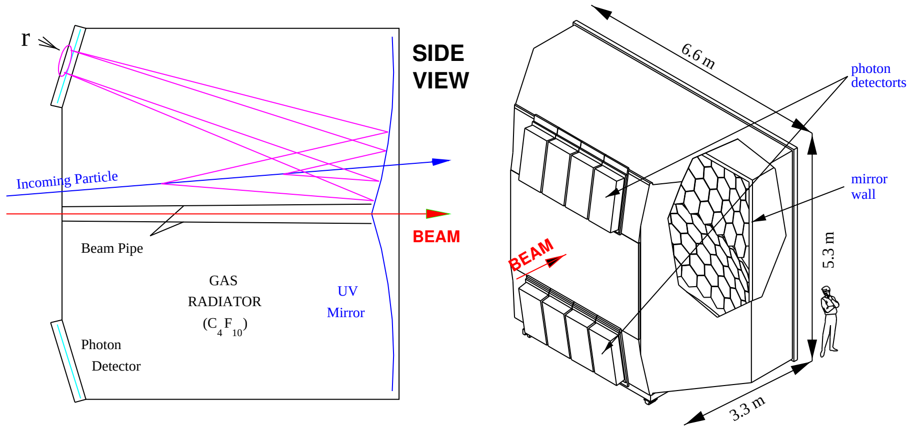

Figure 3.10: A schematic view of the RICH detector. The side view on the left shows how the photons radiated by a traversing charged particle are reflected by a mirror system onto photon detectors. Parallel rays are focused into points in the plane of these detectors, meaning that the photons emitted by a given particle result in a ring. The dimensions of the setup and the arrangement of the photon detectors are shown on the right.

where the radius of the sphere R_m is 6.6 m. The measurement of the ring radius thus gives access to the Čerenkov angle, requiring an excellent resolution of the photon detector.

In order to detect the Čerenkov photons they are first converted to electrons in a layer of CsI. This layer is situated on the cathode plane of a MWPC which is to detect the resulting electrons. The segmentation of the read-out cathode of $8 \times 8\,\mathrm{mm}^2$ is meant to provide a sufficient resolution and leads to 80000 channels with a total active area of $5.3\,\mathrm{m}^2$. The transmission properties of the quartz window which separates the radiator gas volume from the photon detectors yields a lower limit of the sensitive region of the RICH detector of 165 nm [74]. The quantum efficiency of CsI, which vanishes beyond 200 nm, gives the upper limit of this region [75].

A major source of background for the RICH are pile-up muons‡ crossing the detector. This effect is limited by the installation of a beam pipe, which is shielding the photon detectors from photons originating from the beam region. The pipe is filled with He in order to reduce the material budget, exploiting the larger radiation length of He compared to the radiator gas. However, not the entire beam can be contained in the pipe, which means that the halo of the beam still leads to a substantial amount of background. Upgrade projects to be implemented by 2006 are aiming at improving the time resolution of the photon detection. This will allow a better discrimination of the background [76].
More details on the RICH detector can be found in [77–79].

Muon Filters

In principle the two μFilters are very similar. Both are made up of an absorber, which filters out the hadrons, and tracking devices, which are to detect particles that manage to

‡Beam muons which have not interacted in the target are called pile-up muons. Therefore they do not primarily belong to the event in question.

penetrate the absorbers. The ability to cross the amount of material as provided by the absorbers gives a strong indication that the particles in question are muons.

In the case of μFilter1 the absorber consists of 1 m iron and for the tracking part Plastic Iarocci Tubes (PIT) are used [1], denoted in Fig. 3.7 as MA01 and MA02.

The setup of Muon Filter 2 has several parts. The main absorber of μFilter2 consists of 2 m iron and the corresponding trackers are drift-tube detectors with an active area of about $4.0 \times 2.0\,\mathrm{m}^2$. The second absorber of this setup, μFilter2$'$, is made of 50 cm concrete and is to protect the trigger hodoscopes installed downstream of it (HM05 and HL05 in Fig. 3.7) from hadrons, which made their way through the hole of μFilter2. μFilter2$'$ also has a hole in the centre for the beam, otherwise muons could react with the material of the absorber and contaminate the trigger with remnants of this interaction. A third absorber, μFilter3, is to protect the hodoscopes of the HI05 setup from hadrons, which travelled through the beam holes of μFilter2 and μFilter2$'$. It is arranged in such a way that it is not illuminated by the beam.

Calorimetry

The final COMPASS setup foresees a set of electromagnetic (ECAL) and hadronic (HCAL) calorimeters for each of the spectrometer stages. For the data taking up to now only the HCALs were completely equipped and read out, whereas the ECALs are still in a construction and commissioning phase.

HCAL1 and HCAL2 [5] consist of iron/scintillator-sandwich modules and exhibit a relative energy resolution σ_E/E of $60\,\%/\sqrt{E/\mathrm{GeV}} + 8\,\%$ and $65\,\%/\sqrt{E/\mathrm{GeV}} + 5\,\%$, respectively. In addition to the possibility of using the HCAL to separate strongly interacting particles from electromagnetically interacting ones, the HCAL signal is also used in the trigger as will be pointed out in the next section.

3.3.3 Muon Trigger

The purpose of the trigger is to enhance the fraction of events with certain topological and kinematic properties and to suppress the recording of events which are not interesting. The decision has to be taken quickly, since the buffering of data in the detector electronics is limited ($< 600\,\mathrm{ns}$) especially in the case of the HCALs. The trigger thus needs information from quickly responding detectors. In the case of COMPASS it is based on signals from dedicated hodoscope systems and the hadron calorimeters. The events selected by this trigger can be classified in two groups:

Quasi-real photon events: For the open-charm measurement it is important to make use of the entire photon spectrum, even down to quasi-real photons due to the flux increase at small Q^2 (cf. Sec. 2.5.1, Eq. (2.67)). Small Q^2 are related to small scattering angles of the muon, providing a first requirement for the trigger. For the production of a pair of charm quarks $\hat{s} \approx 2\eta y E M_N > 4m_c^2$ is required (cf. Eq. (2.65)). In addition a sufficient photon polarisation is needed. It enters the analysis in form of the depolarisation factor D (cf. Eq. (2.73)), which is approximately proportional to the relative energy of the photon y.

So the minimum requirement for the trigger was chosen to be $y > 0.2$. The trigger classes which cover the mentioned kinematic range are called Inner Trigger (IT) and Ladder Trigger (LT) (cf. Fig. 3.11).

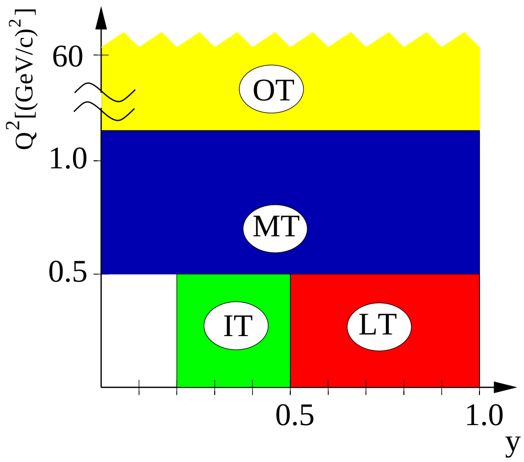

Figure 3.11: The approximate kinematic ranges of the various trigger categories.

The magnetic fields of the spectrometer dipoles serve to separate the beam from muons which encountered energy loss in the target. But a single measurement of the deflection in the bending plane of the magnets is not enough. Especially for events at the lower end of the desired y-range the deflection due to scattering in the target (θ_X-effect) can be of the same order as the bending due to magnetic deflection. These two effects can be disentangled by measuring the deflection in the x coordinate at two different points along the setup. This is done by dedicated hodoscope setups, two for each one of the trigger classes named Hx04 and Hx05, where x$\in${I,L} for Inner Trigger and Ladder Trigger. The desired events populate a certain region in a plane given by the hit positions in the two corresponding hodoscope planes. Appropriate combinations of coincident hits in the hodoscopes are subsequently selected in specially designed trigger matrices (cf. Fig. 3.12).

Inclusive Deep Inelastic Scattering: In order to be able to draw conclusions from DIS events, there has to be a hard scale in the process, justifying a perturbative treatment. In the case of DIS this hard scale is given by the momentum transfer Q^2. As a trigger requirement $Q^2 > 0.5\,(\mathrm{GeV}/c)^2$ was chosen. The trigger classes selecting these events are called Middle Trigger (MT) and Outer Trigger (OT) (cf. Fig. 3.11) and are again produced using two hodoscope setups for each of the triggers. For the Middle Trigger they are called HM04 and HM05 and consist of hodoscopes oriented along the x and the y-axis providing a check whether a given muon track points to the target in the horizontal and vertical planes, in addition to the disentanglement of magnetic deflection and scattering angle in the target. The Outer Trigger, which extends the kinematic coverage up to very large Q^2, uses signals from horizontally oriented hodoscopes and thus checks target pointing in the non-bending plane only.

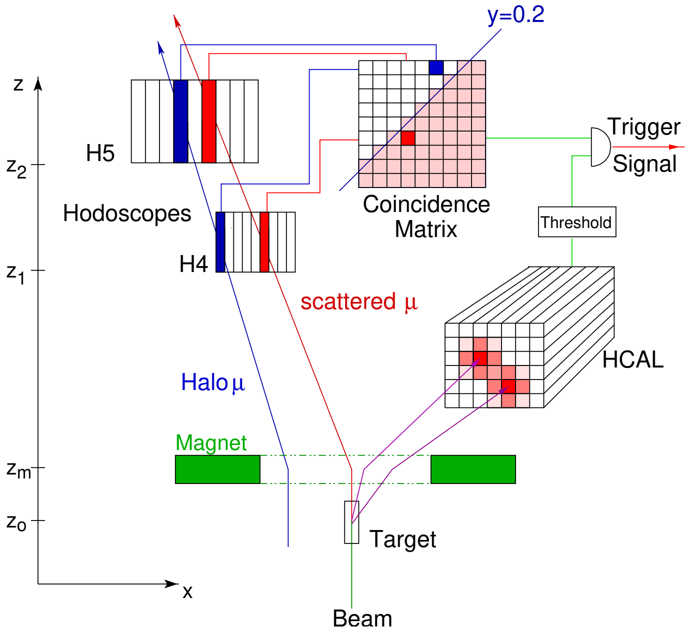

Figure 3.12: Principle of the trigger based on energy loss and the requirement of an associated hadron in the final state. The interaction at z_0 yields a scattered muon, which is deflected in a magnetic field at z_m (for simplicity the two spectrometer magnets are combined here) and detected in hodoscopes at z_1 and z_2. The two measurements make it possible to independently select low Q^2 and a chosen range of energy loss. The required HCAL signal suppresses background due to elastic processes [80].

A common source of background to all of the three trigger classes are halo muons. In order to suppress triggers where a halo muon has been mistaken by the trigger logic as a scattered muon, systems of hodoscopes, which can be used as a veto, are installed at various locations upstream of the target. In addition to these dedicated trigger hodoscopes, selected horizontally oriented channels from the SciFi stations upstream of the target are used to suppress particles with large angles. Since the use of a veto introduces a significant dead time in the system, there are two versions of veto combinations which differ in how stringent they perform the veto and thus in how much they reduce the trigger rate. The most stringent form is used with the Middle and Outer Trigger, whereas the less stringent version is used with the Ladder Trigger. No veto is applied to the Inner Trigger.

Events resulting from elastic muon-electron scattering and (quasi) elastic radiative scattering off target nuclei are a source of background especially for the quasi-real photon triggers. They can be suppressed by asking for a minimum energy deposit in one of the hadronic calorimeters. The use of the calorimeter in the trigger is a possible source of bias, e.g. due to different acceptances for positively and negatively charged hadrons. Therefore it was chosen to use the Middle and Outer Trigger without asking for a coincident signal in the calorimeter, explaining the use of the veto mentioned before[§].

A standalone version of the calorimeter signal was used as a trigger (CT) in order to

[§]A semi inclusive version of these triggers was recorded to allow for the determination of efficiencies.

further extend the Q^2 range on the one hand and on the other to provide a means of determination of efficiencies for the hodoscope based triggers.

The final trigger signal is then combined as "IT or MT or LT or OT or CT" and the time of generation of this signal is measured defining a global time scale for the event. More details on the trigger system can be found in [80, 81].

3.3.4 Evolution of the Spectrometer

The schematic drawing of the COMPASS spectrometer in Fig. 3.7 shows the state during the data taking of 2004, which contributes more than one half to the charmed-meson statistics used in the analysis of this thesis, the other half being contributed by the years 2002 and 2003. In order to be able to interpret the data properly, one needs to know how the spectrometer looked like during the corresponding data-taking periods. The modifications to the spectrometer during the years 2002 to 2004 will be described in the following. The evolution of the BMS setup was already covered in Sec. 3.1.1.

In 2002 the SI03 station was still in a commissioning phase and the beam telescope upstream of the target was therefore supplemented with a Scintillating Fibre prototype. It was found that the additional SciFi station did not significantly contribute to the beam reconstruction due to its limited size and it was removed after 2002 and the corresponding electronics re-used for the station BMS05.

In the category of the tracking detectors downstream of the target the changes effected mainly the reconstruction of particles with large scattering angles and were thus aiming at an improvement of the reconstruction of events with large Q^2. In this context two stations of Straw Tube detectors (Straw 5 and Straw 6) were added to the spectrometer in 2003. The two stations of W-45 used in 2002 were backed up with two more stations each in 2003 and 2004. The reconstruction of the scattered muon, which in rare events suffered from missing redundancy in the case of small scattering angles, was improved by an additional station of GEMs (GEM11) in 2004.

In the final setup the ECAL1 and ECAL2 will be situated directly upstream of the respective HCAL and will thus protect the HCAL from electromagnetic showers initiated by photons or electrons. In the absence of ECAL2 in 2002 a lead wall of 10 cm thickness was used in front of HCAL2. This lead wall was then removed in 2003, when the ECAL2 was sufficiently equipped with lead glass.

3.4 The Data Acquisition and Data Analysis Model

The Data Acquisition System (DAQ) [53, 54, 82] was designed to fulfil the requirements imposed by the need for high rates. The innovation in the DAQ system is, that the data are digitised right at the detector on front-end cards (cf. Fig. 3.13) or very close to it on dedicated Mezzanine Cards. The data are then received by the COMPASS readout driver, called CATCH¶, which is common to all detectors except the GEM detectors and

¶COMPASS Accumulate, Transfer & Control Hardware the Silicon Microstrip detectors. Already at this stage a basic event building is performed and the data are put into a common format.

After being transferred via optical links to the DAQ barrack, the data are stored in so-called readout-buffer PCs and then processed in an event builder farm (cf. Fig. 3.13), which combines the pieces of data belonging to an event. Finally, the data are transferred via a dedicated network to the central data recording on the Meyrin site, where they are temporarily stored on disc. For longterm storage the data are eventually written to tape.

The readout driver is not only used to collect data from the detectors, but also to pass information to the detectors. Among this information are configuration data, which are passed to the front-end electronics attached to the detectors, as well as the trigger signal, which arrives at the CATCH via optical fibres from the Trigger Control System.

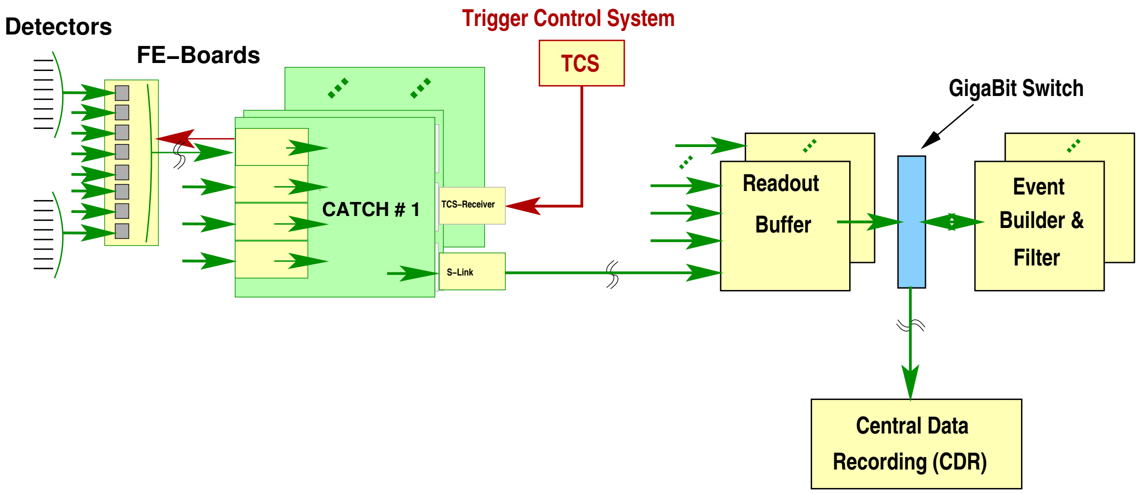

Figure 3.13: The data acquisition system of the COMPASS experiment. The data flow from the detectors via the front-end electronics, the read-out driver CATCH and the read-out buffers to the event building is shown. The CATCH is also used to pass the trigger signal, which it receives from the Trigger Control System, to the front-end electronics of the detectors.

The data recorded by the DAQ are organised in so-called runs which typically contain 100 or 200 spills. These runs are grouped together in periods which contain the data of about one week. During such a week of data taking the access to the spectrometer is strictly limited in order to ensure the stability of its properties. This stability is the basis for the measurement of small asymmetries. Since asymmetries are calculated separately for each period, modifications done to the spectrometer setup in between these periods are not harmful to the physics result.

During the years 2002 to 2004 a grand total of 700 TB of data have been written to tape. This number shows the need for a powerful data analysis framework in order to cope with this amount of data.

As soon as detector calibrations and alignment information are ready, the raw data can be processed using the COMPASS Reconstruction and Analysis Framework (CORAL) [5]. Before the data pass this first stage, runs are excluded which exhibited pathological features already during data taking. Among these features are irregularities in the accelerator system and the beam line or failure of important parts of the spectrometer or the DAQ system.

Many physics aspects covered by COMPASS involve the measurement of asymmetries, where data taken for different target configurations enter (cf. eg. Eq. (2.73)). If an important detector fails for one configuration but is perfectly working for the other, this could lead in the worst case to false asymmetries. Therefore care is taken in this kind of situations to artificially switch off parts of crucial tracking detectors in the analysis which have failed in the corresponding partner configuration.

In CORAL the data recorded by the DAQ are decoded and the different steps of the data reconstruction are performed, like track and vertex reconstruction and also for example the processing of the RICH information. The most important outcome of the data production are the so-called mDSTs[‖], where the amount of information is strongly limited as compared to the raw data. The mDSTs essentially contain completely reconstructed objects like vertices and tracks to which information on particle identification is associated. In addition only events which satisfy the minimum requirement of having at least one vertex reconstructed are saved. The reduction in size achieved by these limitations, and also the fact that no further reconstruction is necessary, results in an essential gain in processing speed of the mDSTs. This is a prerequisite for an effective physics analysis of the data. The mDST files can eventually be analysed using the PHAST[**] framework, which has also been internally developed in COMPASS [83]. In the case of the open charm analysis of this thesis the data were further condensed and only the most essential information was written to a ROOT-tree [84], filled with only such events which showed strong hints of charmed mesons having been produced in the interaction.

The behaviour of the COMPASS spectrometer can be simulated with a dedicated software package called COMGEANT [85]. The output of this package can then be processed by CORAL and PHAST similar to real data. The physics events, which are eventually taken as input to COMGEANT, are produced by an event generator. For this work mainly the AROMA [86] generator was used, which is a dedicated tool to produce heavy quarks through boson-gluon fusion.

[‖]mini Data Summary Tape

[**]Physics Analysis Software and Tools

Chapter 4

The Beam Reconstruction

The momentum vector of the incident beam muons can be determined on an even-by-event basis using the BMS setup described in Sec. 3.1.1 and the beam telescope just upstream of the COMPASS target. The event-by-event reconstruction is important, since many analyses rely on accurate determination of the muon kinematics to be used in cuts to suppress physical background. An example for this aspect will be given in Chapter 5, where the fractional energy of the D meson is used in order to enhance the signal fraction. In addition, the beam kinematics are needed event-by-event, since they are used for the computation of information like the beam polarisation $P_\mu(p_\mu)$ and the depolarisation factor $D(y)$, which are used as an event weight in many analyses.

The principle of reconstruction of the beam momentum will be covered in Sec. 4.1. A method of how the efficiency of the involved setup can be determined unambiguously is introduced in Sec. 4.2. This method was then used to monitor the optimisation of the efficiency of the beam reconstruction by several improvements of the reconstruction algorithm. This aspect will be discussed in Sec. 4.3. It was already mentioned in Sec. 3.1.1 that the experimental setup evolved during the period 2002–2004 affecting also the reconstruction algorithms and efficiencies. The analysis described in this chapter covers the years 2002 and 2003, for information on the reconstruction in 2004 the reader is referred to [87].

4.1 Reconstruction of the Beam Momentum

In order to fully reconstruct the beam particles, information about the momentum of the particle and its direction of flight is needed. The absolute value of the momentum is obtained from the BMS setup, whereas the direction is measured by a telescope of Scintillating Fibre (FI) and Silicon Microstrip (SI) detectors. The two pieces of information then have to be correlated trying to optimise the efficiency of the reconstruction, while at the same time suppressing fake combinations. This task, however, is complicated by the fact that the contributing detector groups are installed 100 m apart.

The measurement of the absolute value of the momentum in the BMS setup is based on the deflection of the beam in the dipole field of the B6 magnet (cf. Figs. 3.1 and 3.3). In the original setup used in 2002 the trajectory of the beam particle is detected by four BMS stations, yielding in the ideal case four measurements of the y coordinate along the track. Since three measurements are needed to fix the momentum, the possible additional measurement can be used for a consistency check (χ^2_{space}). The momentum and the χ^2_{space} are taken from parametrisations, an approach which minimises computing time. The parametrisations are obtained from a Monte Carlo simulation of the beam line [5].

In order to suppress fake combinations of hits in the BMS stations, time correlation is used. The BMS hits, which enter in the computation of momentum and χ^2_{space} and thus subsequently form a "track" in the BMS setup, must not exceed a certain time difference among each other (3σ). The spectrum of time differences between hits of a possible combination is shown in Fig. 4.1 (left). The use of the time difference has the advantage that the trigger time, which poses a possible source of uncertainty, cancels. Remaining fake combinations are further suppressed by not allowing tracks to have more than one hit in common and by checking that they are not too similar in momentum and χ^2_{space}. If a choice has to be made it will be based on the quality of the time correlation.

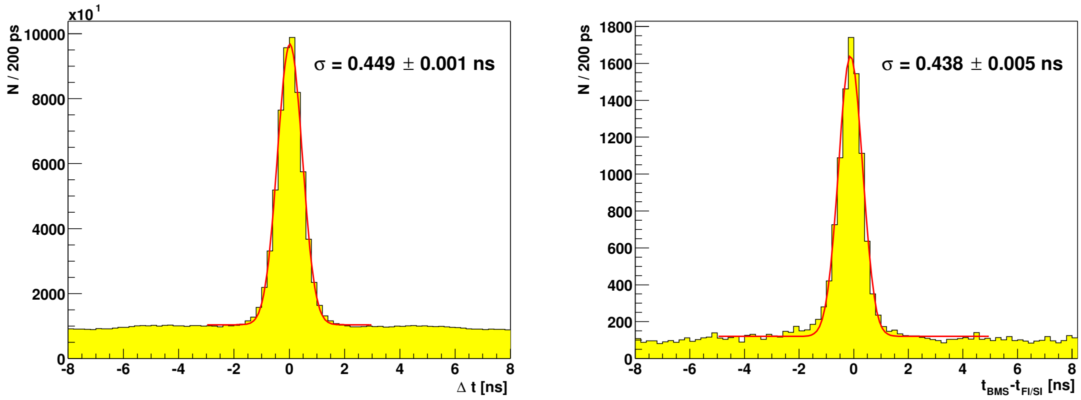

Figure 4.1: Time differences used to suppress fake combinations of information in the beam reconstruction. Left: Distribution of the time difference between hits which are to be combined to a "track" in the BMS setup. Right: Distribution of the difference between the time of the BMS "track" and the track in the FI/SI telescope.

The track pieces in the FI/SI telescope are reconstructed by the usual CORAL tracking package (TRAFDIC), which is used also for the other zones of the spectrometer* [88].
A so-called beam candidate is then obtained by combining the momentum measurement from the BMS with the direction measurement from the FI/SI telescope. Again, the time difference between the combined information is not to exceed a certain limit (3σ). The corresponding distribution is shown in Fig. 4.1 (right). Finally, the beam candidate has to be correlated to the trigger, which is achieved by cutting on the track time of the beam candidate (3σ). This is the only place where the reconstruction algorithm depends on the trigger time.

The time spectrum of the beam candidates is shown in Fig. 4.2 (left). The momentum

*The target and spectrometer magnets as well as the second muon filter divide the spectrometer in zones for tracking purposes.

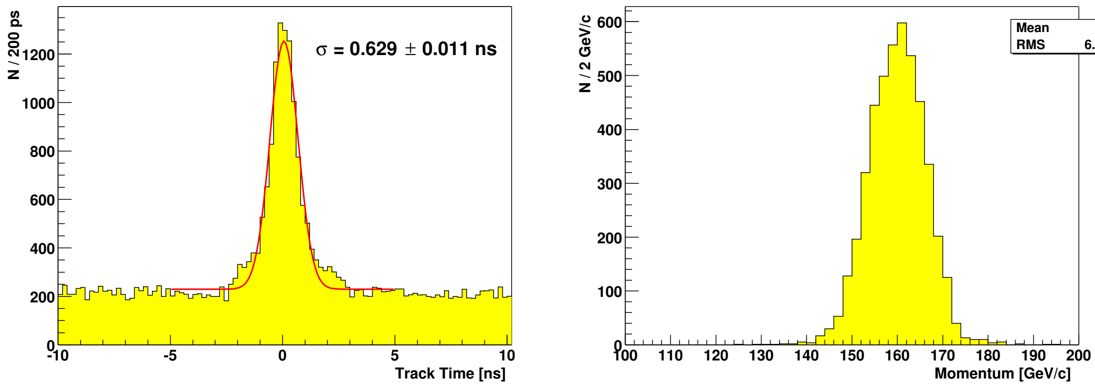

Figure 4.2: Time spectrum of the beam candidates (left) and the momentum spectrum of the final sample after correlation to the trigger by cutting on the track time of the candidates (right). Only unambiguously reconstructed events enter the momentum distribution.

spectrum of the final set of beam candidates is shown in Fig. 4.2 (right). More details on the beam reconstruction and the event timing can be found in [5].

The result of the beam reconstruction is then among one of the following three categories:

- No beam candidate correlated to the trigger can be reconstructed. There will not be a primary vertex and this event is therefore lost for those physics analyses which require the knowledge of the virtual photon kinematics or the position of the primary interaction for asymmetry extractions.

- Exactly one beam candidate can be reconstructed, which is the ideal case.

- More than one beam candidate can be reconstructed. In case only one BMS "track" is participating in all the beam candidates, i.e. is combined to several different FI/SI tracks, the vertexing will be performed on all of the candidates. This procedure possibly results in more than one primary vertex. The user can then decide which of the provided choices is the best primary vertex, so in principle these events can be used in the analysis. If the information from the BMS is ambiguous, i.e. if several different BMS "tracks" are combined with tracks in the beam telescope, the event has to be discarded.

The typical statistics for a nominal intensity run from 2003 is summarised in Tab. 4.1, showing large differences between the beam reconstruction efficiencies for the different trigger types. From these values it is difficult to deduce the efficiency of the beam reconstruction, since here this efficiency is convoluted with the trigger purity. This results in the conclusion that physics data are not useful to estimate the efficiency of the setup involved in the beam reconstruction and the applied algorithms.

Table 4.1: Statistics of the beam reconstruction for a typical physics run from 2003. The results are shown separately for the main trigger types, where e.g. LTCV means LT AND Calorimeter Trigger AND $\overline{\text{Veto}}$.

	0 Candidate	1 Candidate	>1 Candidate
ITC	28 %	54 %	18 %
LTCV	49 %	36 %	15 %
MTV	34 %	53 %	13 %
OTV	69 %	24 %	7 %

4.2 Evaluation of the Efficiency using Random Trigger

In order to estimate the efficiency of the beam reconstruction, an event sample is needed where it is safe to assume that there really was a beam particle travelling through the involved detectors, i.e. BMS and FI/SI. Those events where e.g. the trigger fired due to a halo muon, which probably did not cross all active areas of the BMS stations, need to be suppressed. One approach is to select events where there is a beam particle detected and reconstructed in the spectrometer. This event category is, however, suppressed in the physics trigger, because there the sample of events is enhanced where the muon has interacted in the target and thus has lost a given amount of energy, leading to a stronger deflection in the spectrometer magnets compared to the nominal beam axis. The wanted event sample could be enhanced in the so-called Beam Trigger, where a coincidence of certain channels of the Scintillating Fibre stations upstream of the target gives the trigger. However, since the Scintillating Fibre detectors, which are to be evaluated as part of the beam detecting setup, are included in the choice of the event sample this introduces a bias.

A clean way to obtain the needed event sample is to use data recorded with random triggers (RT), which are generated from the noise of a diode [89]. In order to be able to use the resulting event sample to evaluate the beam reconstruction efficiency, an additional software trigger has to be defined. The main principle of this trigger is to find events with a reconstructed beam muon in the spectrometer.

The method searches for tracks which cross the acceptance of both target cells and are reconstructed in all of the FI stations between the target and SM2 (FI03-FI06). The second spectrometer stage is ignored in the reconstruction of these tracks, since there the necessary redundancy is missing, leading to a distortion of the sample. The effect is shown in Fig. 4.3, which displays the slope of the resulting tracks in the y-z plane. The double peak structure is due to the fact that the reconstruction algorithm is in need of a space point in addition to the one from FI07, which is just downstream of SM2. A possible source of such a space point can be the stations GEM07-GEM09, which, however, have a dead zone in the centre leading to only a small overlap between FI and GEM. This, in turn, selects tracks with a special and pathological slope useless for the evaluation of the efficiency.

In order to optimise the selection of tracks a time-correlated hit in station FI07 is required. This increases the lever-arm and at the same time takes advantage of the large

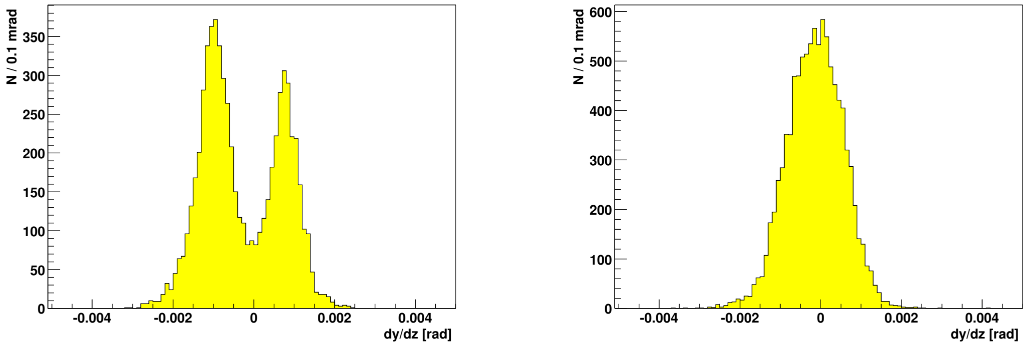

Figure 4.3: The distribution of the slope dy/dz of beam particles reconstructed in the spectrometer. For the distribution on the left both stages of the spectrometer have been used. The double peak structure is caused by the small overlap between SciFi station 7 and GEM stations 7-9. Only the first spectrometer stage has been used for the distribution on the right.

bending power of SM2 improving the momentum measurement. The momentum distribution of the selected sample of tracks in the spectrometer is shown in Fig. 4.4, displaying a peak at 160 GeV/c and thus giving evidence that really a sample of events with a beam particle in the spectrometer has been selected.

Having this sample at hand, the timing of these events has to be considered. It was pointed out that the trigger time is used throughout the experiment to define a global time scale (cf. Sec. 3.3.3). However, in the case of random triggers this trigger time is uncorrelated to what is happening in the spectrometer, making it useless for the purpose of defining a time scale. Since the reconstruction of the BMS information as well as the correlation of the BMS to the FI/SI telescope is based purely on cuts on time differences, this part of the algorithm is not affected by an ill-defined trigger time in contrast to the final absolute cut on the track time for which a proper event-timing is needed.

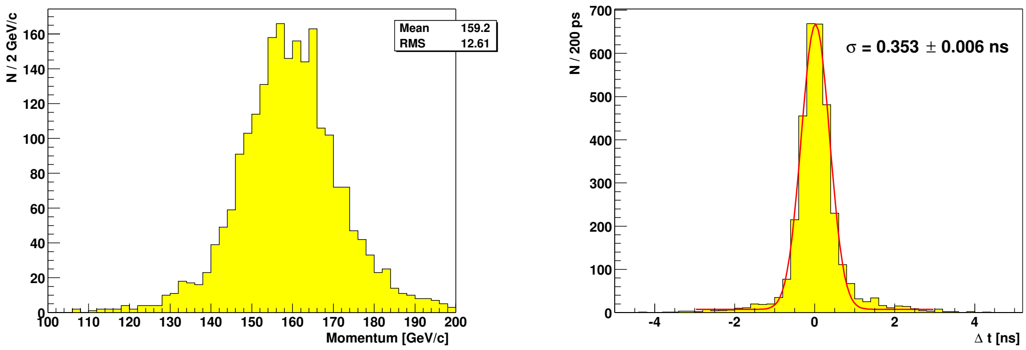

Figure 4.4: The momentum distribution of the beam particles detected in the first stage of the spectrometer (left). The peak at 160 GeV/c shows that really a sample of beam particles has been selected. The difference between the t_{track} of the beam candidates and the t_{track} of the beam particle reconstructed in the spectrometer is plotted on the right, featuring a clear correlation.

Here the method takes advantage of the fact that all FI stations in the first spectrometer stage contribute to the beam-particle track. This means that the track time is measured with an excellent resolution due to the properties of the Scintillating Fibres and can thus be used as a substitute for the trigger time. The time difference between the track time of the beam candidates and the track time of the beam particle in the spectrometer is shown in Fig. 4.4 (right).

With the redefined event-timing the analysis of the random trigger data can proceed just like it does for data obtained with physics trigger. The result of the analysis is summarised in Tab. 4.2 for the years 2002 and 2003. Since the reconstruction algorithm is the same for the two years, the differences in Tab. 4.2 can only be due to changes in the experimental setup.

Table 4.2: Beam reconstruction statistics for random trigger for 2002 and 2003. The numbers in brackets show the absolute fraction which can be resolved by the vertexing.

	0 Candidate	1 Candidate	>1 Candidate
Random Trigger (2002)	17 %	72 %	11 % (3 %)
Random Trigger (2003)	8 %	78 %	14 % (3 %)

It is now interesting to find out, which part of the beam-detecting setup has failed to deliver information in those cases where there is no beam candidate reconstructed. For this purpose a time window is opened around the track time of the spectrometer track and it is checked whether there is a BMS "track" or a FI/SI track, respectively. The resulting statistics are summarised in Tab. 4.3. It turns out that the BMS setup is contributing most to this category and that the improvement from 2002 to 2003 seen in Tab. 4.2 is due to an increased efficiency of the BMS hardware. In fact these improvements can be related to a reshuffling and refurbishment of BMS electronics.

Table 4.3: The table shows the behaviour of the BMS setup and the FI/SI setup respectively in those events with no beam candidate reconstructed. The BMS is responsible for the largest fraction of these events and improving its performance from 2003 compared to 2002 helped to decrease the non-reconstructable fraction. The numbers are obtained by checking whether there is BMS or FI/SI information in a given time window around the event time. The approach can therefore only approximately simulate the behaviour of the nominal analysis which is based on cuts on time differences. This leads to the entries in the last column, which seem to be contradictory to the fact that there is no beam candidate reconstructed in the corresponding event.

	FI/SI failed	BMS failed	FI/SI and BMS failed	FI/SI and BMS are ok
2002	1 %	14 %	1 %	1 %
2003	1 %	6 %	0 %	1 %

4.3 Optimisation of the Reconstruction

The method of evaluating the beam reconstruction efficiency developed in the last section can be used to monitor the optimisation of the reconstruction algorithm. Several approaches to improve the reconstruction efficiency are discussed in this section. The clustering in the BMS and the back-propagation are aiming at resolving ambiguities in the event sample with more than one beam candidate reconstructed. The BMS rescue procedure and the implementation of the fifth BMS station are to decrease the fraction where there is no beam candidate reconstructed due to the BMS setup. The analysis described in this section is performed on 2003 data.

4.3.1 Clustering in the BMS

The scintillator strips in the stations BMS01 to BMS04 overlap by a few hundred μm, therefore a clustering of hits can be useful. The need for the clustering is shown in Fig. 4.5, where for BMS04 the time difference between hits is plotted versus the difference in their y coordinate. A crowded area is clearly seen at small time differences ($< 0.5\,$ns) and differences of Δy/mm $\in (0, 5]$ and Δy/mm $\in (5, 10]$, which correspond to horizontally and vertically neighbouring strips, respectively. A clustering method has been developed [5], which results in an increase of the unambiguous event sample of 3 % (cf. Tab. 4.4).

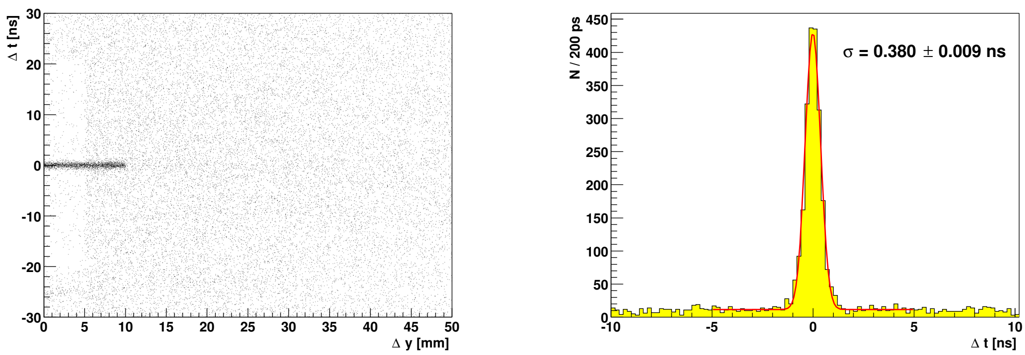

Figure 4.5: The plot on the left shows the time difference between hits in the BMS04 station versus their difference in the y coordinate. The crowded area at small time differences and small differences in the y coordinate (<10 mm) is a motivation to use a clustering procedure. The plot on the right shows the projection on the Δt-axis, the time correlation between neighbouring hits displays a σ of about 380 ps.

4.3.2 Back-Propagation

The correlation in space of the BMS measurement with the one in the FI/SI telescope is complicated by the beam optics in between, consisting of dipole and quadrupole magnets. But in principle the beam optics are known and also used in the Monte Carlo simulation of the beam line [90]. With this knowledge the y coordinate at a given BMS station k can be deduced from the values of $y_{\mathrm{FI/SI}}$, $dy/dz_{\mathrm{FI/SI}}$ as measured by the FI/SI setup and the

Table 4.4: The influence of the clustering in the BMS on the beam reconstruction statistics for random trigger for 2003. The numbers in brackets show the absolute fraction which can be resolved by the vertexing.

	0 Candidate	1 Candidate	>1 Candidate
Random Trigger	8 %	78 %	14 % (3 %)
+ clustering	8 %	81 %	11 % (3 %)

relative deviation of the momentum from the nominal value dp/p_0

$$\mathrm{y}^k_{\mathrm{BMS}} = M_{33}\mathrm{y}_{\mathrm{FI/SI}} + M_{34}\frac{dy}{dz}_{\mathrm{FI/SI}} + M_{36}\frac{dp}{p_0}, \tag{4.1}$$

where M_{ij} is the corresponding element of the transfer matrix of the beamline [91]. The actual values of these matrix elements are summarised in the appendix (cf. Sec. A). The proof of this principle is given in Fig. 4.6, where the difference between the y coordinates as measured in a given BMS station and the back-propagated value is plotted showing a very clean correlation. The spread of the distributions is about a factor of two larger in

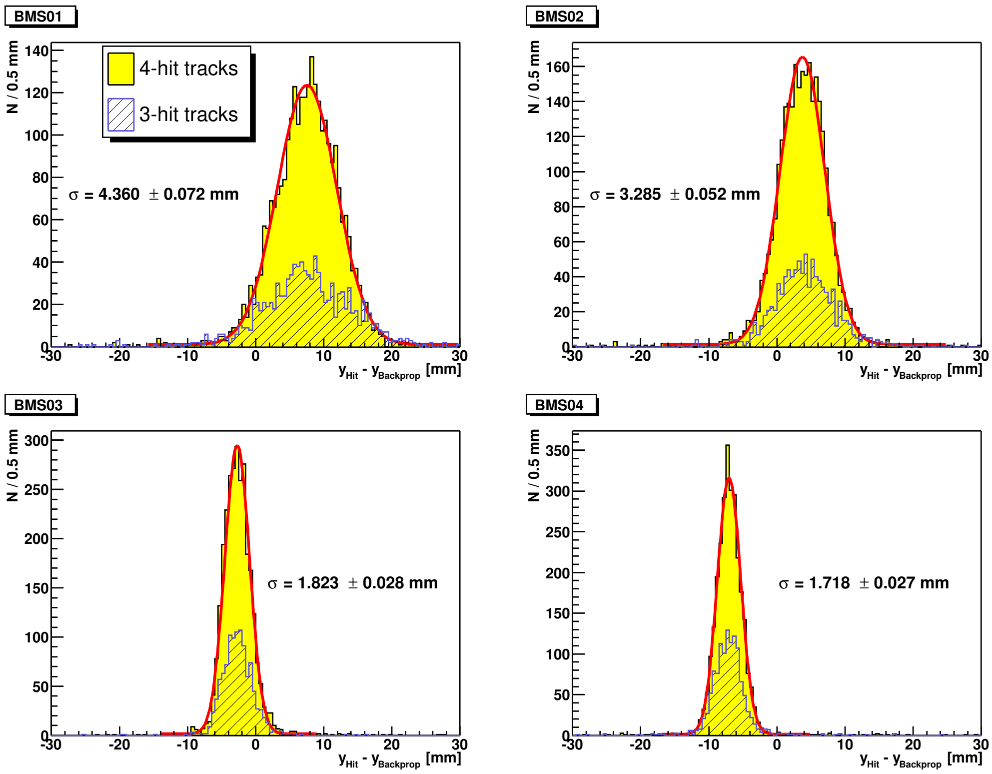

Figure 4.6: Proof of principle for the back-propagation approach. The difference between the y coordinates as measured in a given BMS station and the back-propagated value is plotted. The spread of the distributions obtained from a fit of a Gaussian is indicated.

the stations upstream of the bending dipole B6 as compared to those downstream of it. This difference is caused by the significant vertical dispersion in the transfer matrix due to B6, giving more weight to the momentum and therefore also to its relatively large spread. The offset in the distributions with respect to zero is due to misalignments of beam-line elements and BMS stations.

Based on the correlation between the coordinate from the back-propagation and the measured value, the spatial information can now be used in addition to the time information in order to resolve ambiguities in the association of BMS measurements to those from the FI/SI setup. As a measure of how well two given measurements match a χ^2-probability is used, shown in Fig. 4.7. Those combinations with very low probability (<0.005) are

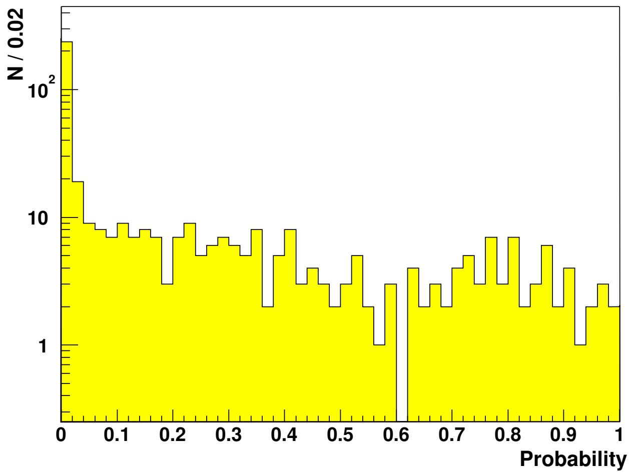

Figure 4.7: Probability distribution for the correlation between back-propagated and measured y coordinate in the BMS. The distribution is sufficiently flat except for the expected enhancement at low probabilities from combinations which do not match.

discarded and from the remaining combinations the one with the largest probability is chosen. This results in a significant improvement of the reconstruction efficiency. Of the formerly ambiguous fraction of 11 % now all but 2 % can be resolved (cf. Tab. 4.5).

Table 4.5: The influence of the back-propagation on the beam reconstruction statistics for random trigger in 2003. The fraction of those events not usable for analysis has decreased from 16 % to 10 % as compared to the situation with just the BMS clustering applied. The numbers in brackets show the absolute fraction which can be resolved by the vertexing.

	0 Candidate	1 Candidate	>1 Candidate
Random Trigger with clustering	8 %	81 %	11 % (3 %)
+ back-propagation	8 %	90 %	2 % (0 %)

4.3.3 BMS Rescue Procedure

In Sec. 4.2 it turned out that the largest fraction of those events with no reconstructed beam candidate is due to failure in the BMS setup. Further investigations show that in about 2/3 of these events the absolute value of the momentum cannot be reconstructed because two BMS planes have failed, however, at least three fired planes are needed for the standard reconstruction.

This situation calls for a rescue procedure, which uses the information from two BMS stations and supplements it with additional measurements from outside the BMS setup. An idea for such a procedure was developed, which uses the slope dy/dz as measured in the FI/SI setup to fix the third degree of freedom in the momentum reconstruction [92]. The procedure requires that at least one of the BMS hits is situated upstream of the B6 dipole. In order to test the rescue procedure, two hits are removed from BMS "tracks", where all planes BMS01 to BMS04 have contributed, and the momentum is computed using the new approach. The difference of the 2-hit result and the original 4-hit momentum is shown in Fig. 4.8, where hits from stations BMS01 and BMS04 have been used. The σ of 0.72 GeV $/c$

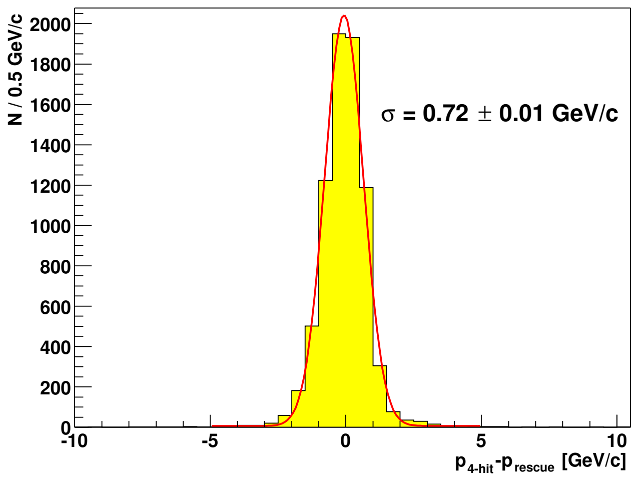

Figure 4.8: Difference between the momentum obtained with 4 BMS stations and the rescued value using two hits (here the hits in BMS01 and BMS04) and the slope dy/dz of the candidate as measured in the FI/SI telescope. The width of the distribution is indicated as obtained from the fit of a Gaussian.

is reasonable relative to the resolution of the default reconstruction of $0.8\,\mathrm{GeV}/c$. However, the resolution of the rescue procedure varies with the combination of available stations. The most unfavoured combination is BMS02/BMS03 due to the small lever arm relative to the dipole with $\sigma = 1.38 \pm 0.01\,\mathrm{GeV}/c$. The average over the event sample, which is to be rescued, is about $1.1\,\mathrm{GeV}/c$.

Using the rescue procedure on the random-trigger data it turns out that it works very efficiently, the fraction of events with no beam candidate decreases by an absolute 3 % to the benefit of the unambiguous sample. The result is summarised in Tab. 4.6 and compared to the situation when using the back-propagation procedure only.

Table 4.6: The influence of the rescue procedure on the beam reconstruction statistics for random trigger in 2003. The fraction of those events with no beam candidate has decreased by an absolute 3 % to the benefit of the unambiguous sample. The ambiguous event sample cannot be further resolved by the vertexing.

	0 Candidate	1 Candidate	>1 Candidate
Random Trigger with back-propagation	8 %	90 %	2 % (0 %)
+ rescue procedure	5 %	93 %	2 % (0 %)

4.3.4 The Rôle of BMS05

The station BMS05 was added for the data taking of 2003 in order to back up the original setup and help to decrease the fraction of events not reconstructable due to too little information from the BMS setup. However, the time resolution of the new plane was about 900 ps during 2003, a performance which is not sufficient for an efficient contribution to the beam reconstruction. In order to avoid that uncorrelated hits from the station BMS05 degrade the overall reconstruction efficiency, it was implemented in the algorithm only in a rescue mode. This means that the new plane is only used if it is not possible to reconstruct at least one trigger-correlated beam candidate with the default procedure or the rescue procedure described in Sec. 4.3.3.

For the use of the new station it is required to have a hit from at least two stations of the original setup and one of the two has to be downstream of the dipole. The gain in reconstruction efficiency as evaluated from random trigger data is about 1 % absolute. The performance of the reconstruction is summarised in Tab. 4.7 and compared to the previous steps in the optimisation procedure.

Table 4.7: The influence of the station BMS05 on the beam reconstruction statistics for random trigger in 2003. The fraction of those events with no beam candidate has decreased by 1 % to the benefit of the unambiguous sample. The table also summarises the optimisation of the beam reconstruction on the basis of random trigger data. The numbers in brackets show the absolute fraction which can be resolved by the vertexing.

	0 Candidate	1 Candidate	>1 Candidate
Random Trigger	8 %	78 %	14 % (3 %)
+ clustering	8 %	81 %	11 % (3 %)
+ back-propagation	8 %	90 %	2 % (0 %)
+ rescue procedure	5 %	93 %	2 % (0 %)
+ BMS05	4 %	94 %	2 % (0 %)

The conclusion of the effort to improve the efficiency of the beam reconstruction is a decrease of the not reconstructable fraction of events from 19 % to 6 %. This result was obtained on random trigger data from the year 2003, however, except for the limited influence of the station BMS05 it is also applicable to the data of 2002.

Since the reconstruction of the charmed mesons as well as the subsequent extraction of $\Delta G/G$ as described in the following chapters depend on the information on the beam momentum, they benefit directly from this improved efficiency.

Chapter 5

The Reconstruction of D Mesons

The aim of this part of the analysis is to provide a set of events where the fraction of photon-gluon fusion (PGF) is enhanced. As was already discussed in Chapter 2, PGF events can be tagged by requiring charmed mesons in the final state. These mesons can be reconstructed by detecting their decay products in the spectrometer. The following decay with a branching ratio of 3.83 % is exploited for this analysis

$$D^0 \to K^-\pi^+ \text{ and } \overline{D^0} \to K^+\pi^-. \tag{5.1}$$

A fraction of 40 % of the D^0 sample originates from the decay of a $D^\star$, where in addition to the D^0 a characteristically soft pion is produced [6].

Assuming a momentum of the D^0 of about 40 GeV/c and a $c\tau$ of 124.4 μm [6], the distance between the primary vertex, where the D^0 is produced, and its decay vertex is about 2.67 mm. The use of the large cold solid state target (cf. Sec. 3.2) prohibits dedicated vertex detectors, which are commonly installed in detector setups at collider machines. The resolution of the z component of the vertex in COMPASS is about 1 cm, which makes the direct reconstruction of the D^0 via its decay vertex impossible, leaving only the identification via its invariant mass.

In order to control combinatorial background, efficient particle identification is needed. This explains that the RICH detector (cf. Sec. 3.3.2) is of great importance for this analysis. The reconstruction of the RICH data is described in Sec. 5.1 along with the subsequent use of the resulting information on the identity of the particles in question.

The basic data selection will be described in Secs. 5.2 and 5.3. Two samples of events are used in the analysis. One sample consists of D^0s originating from a $D^\star$, where the $D^\star$ could be tagged using the soft pion in the final state. Those events where only the decay of the D^0 could be detected constitute the second sample. The reconstruction methods will be described in Secs. 5.4 and 5.5, respectively, on the basis of 2003 data. The final sample of events which will be used for the extraction of ΔG/G is shown in Sec. 5.6.

5.1 RICH Reconstruction

5.1.1 Reconstruction in RICHONE

The RICHONE software package is responsible for the reconstruction of the data from the RICH detector. It is implemented in the CORAL framework (cf. Sec. 3.4) where it is executed during the "production" of the data. Only the most essential parameters needed for particle identification are written to the mDST files. Among these parameters are the likelihood and χ^2 for the various mass hypotheses, whose origin will be described in the following.

The input to the reconstruction are the hits from the photon detectors of the RICH as well as the particle trajectories of the given events. In addition to this information the refractive index of the radiator gas is needed. The reconstruction of the RICH data starts with a clustering procedure. This procedure combines individual hits from the photon detectors to clusters, which are expected to better correspond to the real photon impact point. The next step is to find the ring and extract the Čerenkov angle θ_C. The procedure of fitting the ring in the photon-detector plane is technically rather involved. An alternative is to perform a transformation of the cluster coordinates to the θ-ϕ plane, the plane of the polar and azimuthal angles relative to the particle trajectory. In this plane the clusters from a given particle distribute along a fixed θ uniformly in ϕ, thus the ring search in the detector plane is equivalent to searching for a peak in the θ-projection.

After a first estimation of θ_C corrections can be applied for e.g. mirror misalignments and distortions due to the quartz window, which separates the radiator volume from the photon detectors. Finally the actual particle identification takes place, for which two strategies exist. A χ^2 for the ring can be computed

$$\chi_i^2 = \frac{1}{N_{\mathrm{DOF}}} \sum_{k=1}^{N_\gamma} \frac{\left(\theta_k^\gamma - \theta_i^{\mathrm{ring}}\right)^2}{\left(\sigma_\theta^\gamma\right)^2} \qquad i \in \{\pi, K, p\}, \tag{5.2}$$

where the sum runs over all N^γ photons in the signal, θ_k^γ is the angle of the k-th photon in the ring, θ_i^{ring} is the expected Čerenkov angle for a given mass hypothesis i and σ_θ^γ is the resolution in θ. This χ_i^2 is obtained for three mass hypotheses, namely pion, kaon and proton.

Alternatively, a likelihood can be constructed as follows

$$L_N^i = \prod_{k=1}^{N_\gamma} \left[(1-\epsilon) G(\theta_k^\gamma, \phi_k^\gamma, \theta_i^{\mathrm{ring}}) + \epsilon B(\theta_k^\gamma, \phi_k^\gamma)\right] \qquad i \in \{\pi, K, p\}, \tag{5.3}$$

where ϵ is the background fraction taken from the θ^γ distribution and $G(\theta_k^\gamma, \phi_k^\gamma, \theta_i^{\mathrm{ring}})$ and $B(\theta_k^\gamma, \phi_k^\gamma)$ parametrise the signal and background contributions, respectively. A normalised version of the likelihood $L = \sqrt[N]{L_N}$ is then available for the analysis, in order to allow the comparison of different particles.

The signal contribution $G(\theta_k^\gamma, \phi_k^\gamma, \theta_i^{\mathrm{ring}})$ to the likelihood can be conveniently described as a Gaussian centred at the expected angle θ_i^{ring} with a spread $\sigma_\theta^\gamma(\phi_k^\gamma)$. The advantage of the likelihood as compared to the χ^2 is that it takes into account the background contribution explicitly. However, the difficulty is to describe the background correctly. The quality of this description determines whether the use of the likelihood yields better results in the subsequent analysis compared to a method based on χ^2. Possible contributions to the background are electronic noise, photons from other particles belonging to the same event, but also photons from particles belonging to different events resulting from the memory of the photon chambers. Most of these contributions are difficult to describe theoretically and thus have to be extracted from the data. This turned out to be an ambitious project which could only recently be successfully finished at the beginning of 2005. Up to the implementation of this improved background description the particle identification (PID) based on χ^2 was superior to the use of the likelihood, which is the reason for the fact that this analysis is using the χ^2 method. The gain in statistical significance of the charmed meson signal due to the improved background description is of the order of up to 10 % [93]. However, at the time of completion of this analysis it was only available for a fraction of the data, since it involves a complete reproduction.

5.1.2 The Rôle of the Refractive Index

The refractive index is needed for the calculation of the expected Čerenkov angle for a given mass hypothesis (cf. Eq. (3.2)) and the quality of the resulting information on the particle identity depends on the accuracy to which it is known.

First of all the index depends on the gas mixture in the radiator volume of the RICH. Since it cannot be filled completely with C_4F_{10} gas, there is always a mixture of N_2 and C_4F_{10}, so the refractive index deviates from the expected value of $n_{C_4F_{10}}$. In addition the refractive index depends on the temperature and the pressure of the gas [94],

$$\begin{aligned} \Delta T = +3^\circ \quad &\rightarrow \quad \frac{\Delta n}{n-1} \approx -1\,\% \\ \Delta P = +10\,\mathrm{mbar} \quad &\rightarrow \quad \frac{\Delta n}{n-1} \approx +1\,\%. \end{aligned} \tag{5.4}$$

It is difficult to measure the gas mixture with an accuracy needed for a determination of the refractive index with an uncertainty sufficiently small for the purpose of data reconstruction. Therefore the index has to be extracted from the data by measuring the Čerenkov angle of particles with $\beta \approx 1$, a procedure which requires a pre-production of the data. Practically this is done for a few runs distributed evenly over time and the refractive index is then interpolated between these runs. This estimated value of the index (production index) is then used for the production of the data. After all runs have been processed the refractive index can be exactly determined for the complete sample. The result of this procedure is shown in Fig. 5.1, where the upper row is characteristic for the current level of production of the 2003 data. The deviation from the true refractive index can be kept below 1 %, relative to the true value minus one. For the production of 2004 data, the procedure has been refined. Again a few runs were pre-produced, but now the interpolation was improved with data from temperature and pressure sensors in the RICH vessel. The result is a decreased deviation, which can now be kept below 0.1 %.

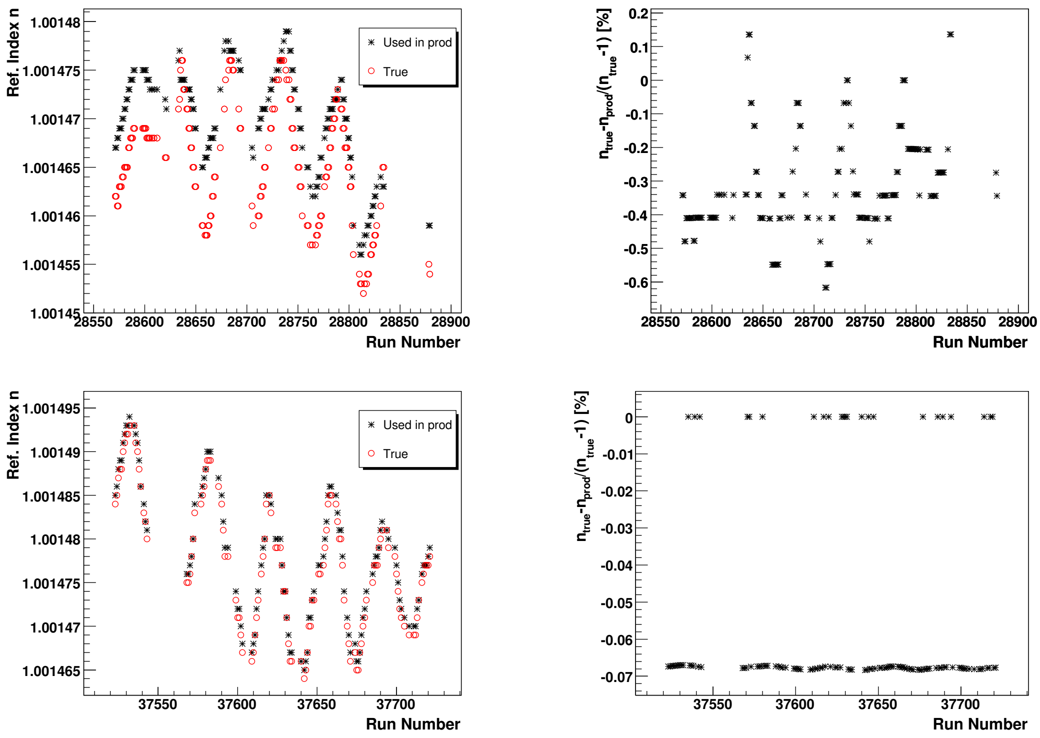

Figure 5.1: The plots on the left show the values of the index used during production as well as the true values extracted after a complete production of the data. The modulation in the distributions is due to day-night oscillations of the pressure and temperature of the radiator gas. The plots on the right give an impression of the relative deviation of the production index from the true index. The upper row shows the period 03P1C as a typical example for 2003, whereas the plots in the lower row contain information from the period 04W29, a typical period for 2004. The effect of the improvement of the interpolation procedure is obvious, in 2003 the relative deviation could be kept below 1 %, whereas in the production of the 2004 data it could be kept below 0.1 %. The gap in the lower right plot is due to the limited precision of the values stored in the data-base. The deviations are given relative to $(n_{\text{true}} - 1)$.

The fact that the true index is not available during the first iteration of production means that also the particle identification parameters written to mDST, namely the likelihoods and χ^2s, are determined only with the estimated value for the index. For both sets of PID parameters correction methods have been developed, which take into account the deviation of the production index from the true value.

For the correction of the likelihood the first derivative is stored in the mDST, which allows for the following correction

$$L(n_{\text{true}}) = L(n_{\text{prod}}) + \left.\frac{\partial L}{\partial n}\right|_{n_{\text{prod}}} (n_{\text{true}} - n_{\text{prod}}) \,, \tag{5.5}$$

where n_{prod} is the value of the refractive index available during the production and n_{true} is the true value.

The correction method for the χ^2 is only summarised here, details can be found in the appendix (Sec. B.1) [95]. The corrected χ^2 is given by

$$\chi_i^2 = a(\vec{\chi}^2_{\mathrm{prod}}) - 2 \cdot b(\vec{\chi}^2_{\mathrm{prod}}) \cdot \theta_i^{\mathrm{true}} + c(\vec{\chi}^2_{\mathrm{prod}}) \cdot (\theta_i^{\mathrm{true}})^2 \qquad i \in \{\pi, K, p\}, \tag{5.6}$$

where θ_i^{true} is the expected Čerenkov angle now computed with the true refractive index. The variables a, b and c depend on a set of χ^2s available from the mDST information:

$$\vec{\chi}^2_{\mathrm{prod}} = (\chi^2_{\mathrm{prod},\pi}, \chi^2_{\mathrm{prod},K}, \chi^2_{\mathrm{prod,ring}}), \tag{5.7}$$

where $\chi^2_{\mathrm{prod,ring}}$ is the χ^2 of a free ring fit. The advantage of the correction method for the χ^2 is that it is exact. In contrast to that, the correction of the likelihood neglects higher order terms in the expansion, since only the first derivative is available in the mDST. This makes the use of the χ^2 more robust against large index deviations.

5.1.3 Kaon Identification

For the identification of the kaons a χ^2 method is used. The kinematic acceptance of the RICH implies that the momentum of the kaon candidate has to be above the kaon threshold and below 50 GeV/c. The threshold is computed on a run-by-run level using the true refractive index. A Monte Carlo simulation of the momentum spectrum of the kaons resulting from D^0 decays is shown in Fig. 3.9 together with the kinematic acceptance of the RICH. The χ^2 has to comply with the following requirements:

- The χ^2 of the kaon hypothesis has to be smaller than the one of the pion hypothesis: $\chi^2(K) < \chi^2(\pi)$.
- In case the momentum of the kaon candidate is above the proton threshold, the equivalent condition needs to be fulfilled for the proton hypothesis: $\chi^2(K) < \chi^2(p)$.
- The purity of the resulting sample can be further improved by applying a cut on the χ^2 of the kaon hypothesis: $\chi^2(K) < \chi^2_{\mathrm{max}}$.

The result of this method is shown in Fig. 5.2 (left). There the mass spectrum of those particles is shown, which are identified by the described method. The choice of χ^2_{max} is governed by the usual trade-off between efficiency and purity. The optimisation of this cut will be done in Secs. 5.4 and 5.5. As an example the value 5 is used for χ^2_{max} in the figure, resulting in an improvement compared to the situation without cut.

The influence of the χ^2 correction described in Sec. 5.1.2 is shown in Fig. 5.2 (right). The distribution obtained by using the uncorrected χ^2 values is compared to the one where a correction has been applied. The relative deviation of the refractive index for this example is 0.6 %. The improvement in the purity of the sample, which can be concluded from the plot shows the importance of the correction.

5.1.4 Pion Identification

Two approaches are used for the purification of the pion sample. The veto method makes indirect use of the RICH. It requires that the particles in question cannot be identified

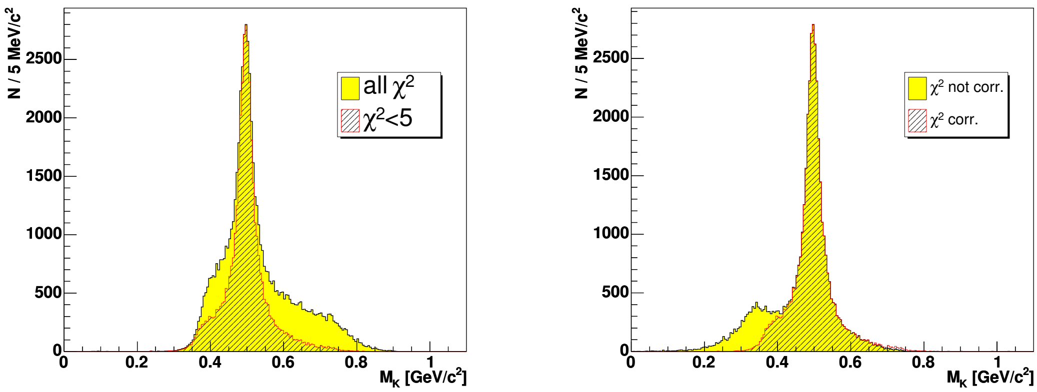

Figure 5.2: The left plot shows the mass spectrum reconstructed by the RICH for those particles, which have been identified as kaons by the χ^2 method. The situation where no cut on $\chi^2(K)$ is applied is compared to the one where $\chi^2(K) < 5$ is required. The spectrum is extracted from run 27876 from 2003. The right plot shows for the same data the influence of the χ^2 correction. The hatch-style histogram shows the distribution after the correction and corresponds to the distribution with $\chi^2(K) < 5$ on the left side. The relative deviation of the refractive index is 0.6 %.

as kaons by the method described in Sec. 5.1.3 otherwise they are excluded from the pion sample. This means that particles without RICH information or particles with a momentum below the RICH kaon threshold are considered as pions.

A stricter selection is done by positively identifying the particles using information from the RICH. The kinematic acceptance now implies that the momentum of the candidates has to be above the pion threshold and below 50 GeV/c. Since a comparison to the χ^2 of at least one other mass hypothesis can only be done for momenta above the RICH kaon threshold, the sample of candidates is divided into two categories. The momentum spectrum of pions coming from D^0 decays extracted from a Monte Carlo simulation is shown in Fig. 5.3.

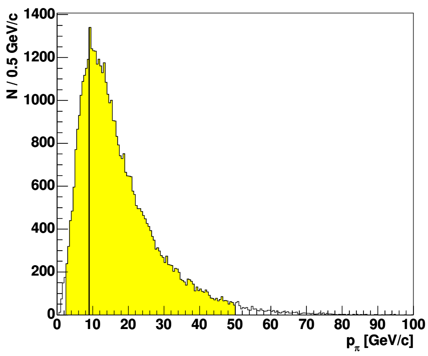

Figure 5.3: The reconstructed momentum of pions from the decay of the D^0 extracted from a Monte Carlo simulation. The filled histogram shows the momentum acceptance of the RICH. The black line indicates the division of the sample into two categories for which separate PID procedures are used.

For those particles with a momentum above the kaon threshold the following conditions have to be met:

- The χ^2 of the pion hypothesis has to be smaller than the one of the kaon hypothesis: $\chi^2(\pi) < \chi^2(K)$.
- In case the momentum of the pion candidate is above the proton threshold, the equivalent condition needs to be fulfilled: $\chi^2(\pi) < \chi^2(p)$.
- In addition a cut on the χ^2 of the pion hypothesis is applied: $\chi^2(\pi) < \chi^2_{\max}$.

The result of these cuts is shown in Fig. 5.4 (left). In the plot the mass distribution of the identified pions extracted without an absolute cut on χ^2 is compared to the distribution where $\chi^2_{\max} = 5$ has been used. Again this choice of $\chi^2_{\max}$ is an example to demonstrate the effect of the cut and the optimisation will be covered in Secs. 5.4 and 5.5.

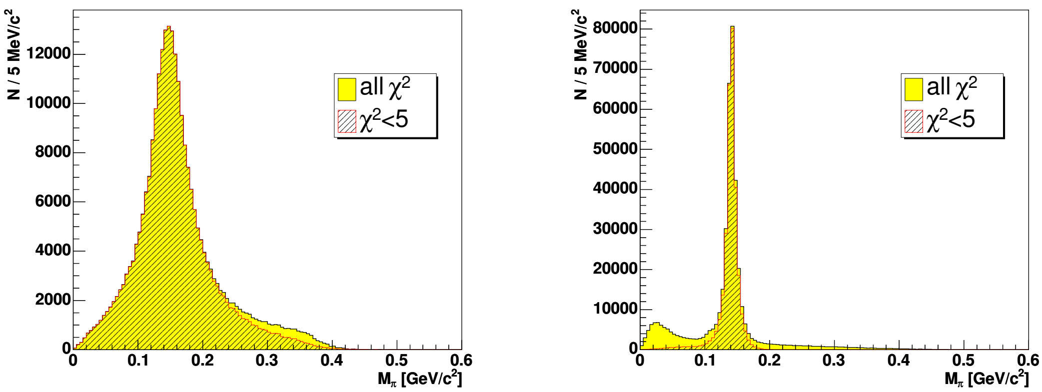

Figure 5.4: The plots show the mass spectrum reconstructed by the RICH for those particles which have been identified as pions by the χ^2 method. The left plot contains those particles with a momentum above the RICH kaon threshold. The situation where no cut on $\chi^2(\pi)$ is applied is compared to the one where $\chi^2(\pi) < 5$ is required. The right plot shows the spectrum for those particles with a momentum above the pion threshold but below the kaon threshold. The effect of a cut of $\chi^2(\pi) < 5$ is shown. The spectra are extracted from run 27876 from 2003.

In the case of those particles which have a momentum below the kaon threshold the identification via the minimum χ^2 is not possible. Thus a stricter absolute cut on $\chi^2(\pi)$ may have to be applied as a compensation. The mass spectrum resulting from this sample of events is shown in Fig. 5.4 (right).

5.2 Run Selection

The analysis presented in this thesis is based on all data taken in longitudinal target spin configuration during the years 2002 to 2004. Details on the data-taking periods like the production version and the status of the RICH are summarised in the appendix (Sec. B.2).

The extraction of the gluon polarisation involves the measurement of small asymmetries. This means that one has to pay special attention to the stability of the spectrometer. A few observables have been chosen to monitor the stability, among these are:

- Average number of primary vertices per event
- Average number of tracks in the SciFi/Silicon telescope per event
- Average number of tracks per event
- Average number of tracks associated to the primary vertex per event
- Integrated beam flux.

The quantities are monitored spill-wise and spills which are deviating from the main band by more than 5σ are excluded. The list of spills which were excluded from this analysis was obtained from the COMPASS stability web page [96]. In addition to this selection a few runs were excluded for various reasons. A summary of these runs is also included in Sec. B.2.

5.3 Basic Event Selection

In the following a few basic cuts are described, which are applied to the data before the actual reconstruction of D^0s and $D^\star$s takes place.

- Only events with at least one primary vertex are used for the analysis. A vertex is defined as primary vertex, if the incoming beam muon is associated to it. In case of several primary vertices the one with the largest number of associated tracks is chosen or, if the vertices are equal in this respect, the one with the best χ^2 of the fit.
- The scattered muon has to be associated to the primary vertex. It is mainly identified by looking for associated hits in those trigger hodoscopes which contribute to the trigger type of the event in question.
- Only tracks that are associated to the primary vertex and that are not identified as scattered muon are considered as hadron candidates possibly coming from the $D^\star$ or D^0 decay.
- The hadron candidates should not be exclusively reconstructed upstream of the first spectrometer magnet (SM1). For candidates not meeting this condition only the fringe field of the spectrometer magnet could be used for the momentum determination resulting in a degraded resolution.

In order to be able to extract the gluon polarisation from the data, one has to make sure that the interaction took place in one of the target cells filled with ^{6}LiD. The distributions of the three coordinates of the primary-vertex position are shown in Fig. 5.5. A clear separation of the two target cells can be seen in the distribution of the z coordinates, which means that events can be attributed to a given spin configuration with good accuracy.

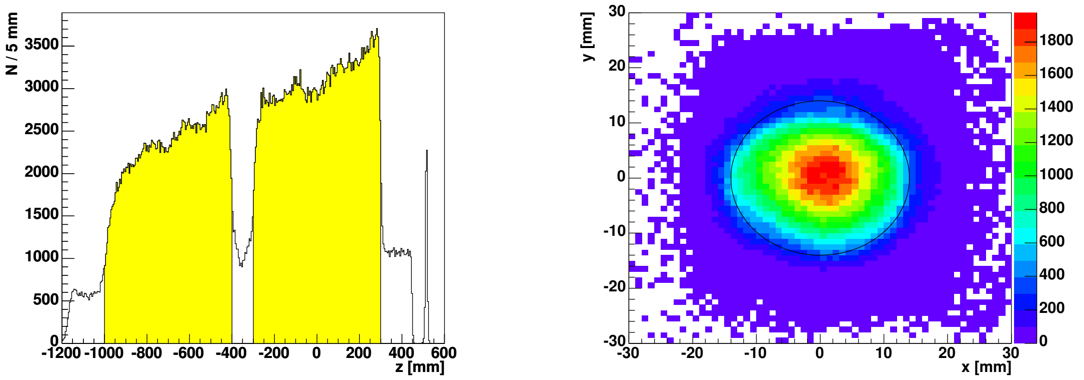

Figure 5.5: The distribution of the spatial coordinates of the primary vertex. The plots are generated from the data sample after applying all cuts but the target cuts defined in the following. The distribution of the z coordinate shows that the two target cells can be well separated. The nominal position of the target cells is shown as the shaded region. In the distribution of the lateral coordinates the applied cut on the target radius of $r < 14$ mm is shown as a black circle.

It turned out that the target is not perfectly aligned with the z axis of the spectrometer (cf. Fig. 5.6 and Tab. 5.1). The cuts on the position of the primary vertex are thus applied in the reference frame of the inclined target. The containers, which hold the target material can only be opened in a few places for filling purposes. This means that it is technically not easily possible to fill the two target containers completely with ^{6}LiD, especially also because the filling has to be done in liquid nitrogen. The fact that the target cells are not completely filled is taken into account by a cut on the y coordinate of the vertex. The cuts applied on the coordinates of the primary vertex are thus as follows:

- The z coordinate is situated in the upstream cell ($100\,\mathrm{cm}<\mathrm{z}<-40\,\mathrm{cm}$) or in the downstream cell ($-30\,\mathrm{cm}<\mathrm{z}<-30\,\mathrm{cm}$) of the target.
- The radius r is smaller than 1.4 cm.
- The y component is smaller than 1 cm.

The advantage of having two oppositely polarised target cells is that the terms entering the asymmetry can be measured simultaneously. This means that the measurement is

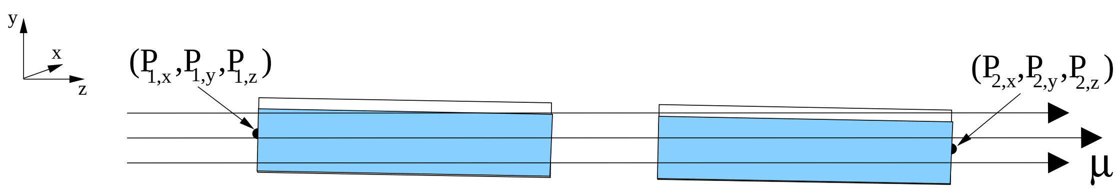

Figure 5.6: The plot shows a sketch of the inclination of the COMPASS target. The coordinates of P_1 and P_2 are summarised in Tab. 5.1. The shaded area inside the target cells indicates the volume actually filled with ^{6}LiD.

Table 5.1: Summary of the target inclination in 2002–2004 [97, 98]. The position of the points defining the inclination is indicated in Fig. 5.6.

	P_1			P_2		
Year	x/cm	y/cm	z/cm	x/cm	y/cm	z/cm
2002	−0.20	0.10	−100	−0.30	−0.15	30
2003	0.04	0.03	−100	−0.03	−0.20	30
2004	0.01	0.05	−100	0.02	−0.30	30

independent of possible variations of the beam flux. However, the flux only cancels in the asymmetry if it is the same for both target cells. Possible acceptance effects have to be avoided. This is done by requiring that a beam particle, which interacts in a given target cell, could also in principle have interacted in the other cell. A set of cuts is thus applied on the entrance and exit points of the extrapolated beam trajectory, which is equivalent to the one discussed above.

5.4 $D^\star$ Tagging

The choice of cuts for the reconstruction of the charmed mesons is governed by the aim to minimise the statistical error on the measurement of the gluon polarisation. The effective signal is used to monitor the effect of a given cut and is defined as

$$S_{\text{eff}} = \frac{S}{1+\frac{B}{S}}, \tag{5.8}$$

where S and B are the number of signal and background events in a given mass interval. With increasing width of this interval the amount of included signal events increases and the signal-over-background ratio decreases such that the effective signal has a maximum at a certain interval size. The optimal intervals were found to be $\pm 1.8\,\sigma$ and $\pm 1.45\,\sigma$ around the nominal D^0 mass in the case of the $D^\star$ tagged and the untagged D^0 samples, respectively. These mass ranges were then used for the optimisation of the cuts.

Assuming equal acceptances of the target cells, S_{eff} is related to the statistical error on the gluon polarisation via

$$\delta\left(\frac{\Delta G}{G}\right) = \frac{1}{P_\mu P_{\text{B}} f D \langle \hat{a}_{\text{LL}}\rangle} \frac{1}{\sqrt{S_{\text{eff}}}}, \tag{5.9}$$

where P_μ,P_{B},f and D are the diluting factors defined in Eq. (2.73) and $\langle \hat{a}_{\text{LL}}\rangle$ is the mean partonic asymmetry (cf. Eq. (2.70)).

The cuts described in this section and Sec. 5.5 were tuned such that the effective signal is maximised. The effective signal as a function of the corresponding cut is shown in Sec. B.3 for each of the cuts.

This section is dedicated to those D^0s which originate from a $D^\star$ via

$$D^{\star +} \rightarrow D^0 \pi_S^+ \text{ and } D^{\star -} \rightarrow \overline{D^0} \pi_S^- , \tag{5.10}$$

with a branching ratio of 68.3 %. The characteristic feature of this decay is the small mass difference between the $D^\star$ and the D^0 resulting in a so-called soft pion π_S with very small momentum. This feature gives rise to an efficient tagging method, which helps to suppress combinatorial background.

Before the tagging can be applied, the D^0 is reconstructed assuming the golden decay channel into charged kaons and pions (cf. Eq. (5.1)). The invariant mass of the combination is given by

$$M_{K\pi} = \frac{1}{c}\sqrt{(\mathbf{P}_K + \mathbf{P}_\pi)^2}, \tag{5.11}$$

where $\mathbf{P}_i$ are the four-momentum vectors of the kaon and the pion*. The resulting D^0 candidate is then combined with an additional pion according to the decay of Eq. (5.10). The invariant mass $M_{K\pi\pi}$ of the $D^\star$ candidate is then computed in analogy to Eq. (5.11). The strategy of identification of the kaons and pions will be described in Sec. 5.4.2.

5.4.1 Cut on the Mass Difference between $D^\star$ and D^0

The mass difference between the $D^\star$ and the D^0 is given as [6]

$$\Delta m = m_{D^\star} - m_{D^0} = (145.42 \pm 0.05) \text{ MeV}/c^2. \tag{5.12}$$

This mass difference is largely taken up by the pion mass $\Delta m - m_\pi = 5.8\,\text{MeV}/c^2$ and as a consequence the momenta of the decay products in the $D^\star$ rest frame are very small: p=39 MeV/c. The mass difference can therefore be very well reconstructed, since the influence of a limited momentum resolution is suppressed due to the domination by the pion mass.

In Fig. 5.7 the reconstructed mass difference reduced by the nominal pion mass

$$\Delta M - m_\pi = M_{K\pi\pi} - M_{K\pi} - m_\pi \tag{5.13}$$

is plotted versus the invariant $K\pi$ mass reduced by the nominal D^0 mass. The plot shows an enhancement in the expected region. The projections of the distribution on the corresponding axes are plotted in Fig. 5.8 and show how a cut on the mass difference can be used to suppress background. For the following analysis a cut of

$$3.4\,\text{MeV}/c^2 < M_{K\pi\pi} - M_{K\pi} - m_\pi < 8.6\,\text{MeV}/c^2 \tag{5.14}$$

was chosen.

*Throughout this work invariant masses are denoted by an upper case letter, e.g. $M_{K\pi}$. For the nominal value for a particle mass, which is taken from literature, lower case is used e.g. m_{D^0}.

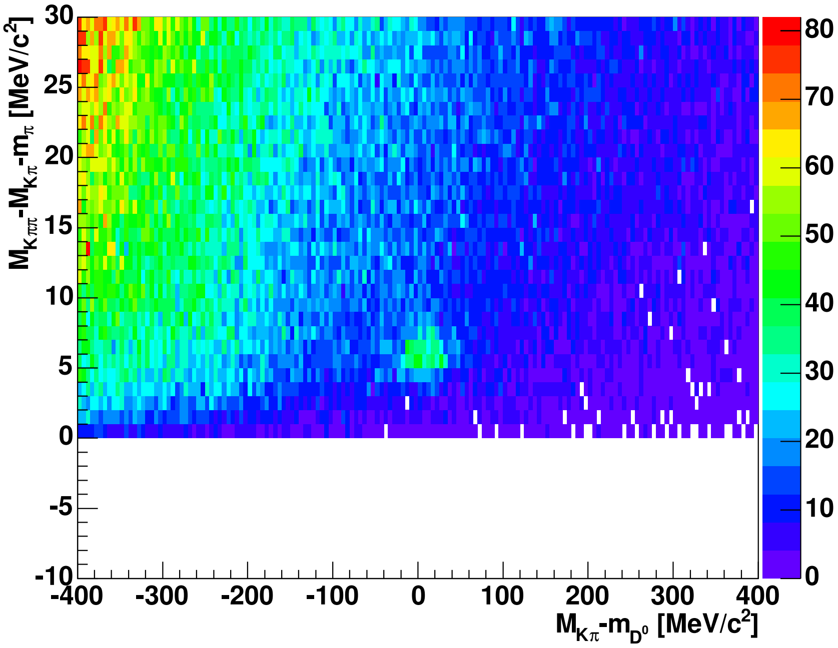

Figure 5.7: The reconstructed mass difference between the candidates for the $D^\star$ and the D^0 reduced by the nominal pion mass is plotted versus $M_{K\pi} - m_{D^0}$. A signal is seen as expected around $\Delta M - m_\pi \approx 6\,\mathrm{MeV}/c^2$ and $M_{K\pi} - m_{D^0} \approx 0\,\mathrm{MeV}/c^2$.

5.4.2 Particle Identification

Kaon Identification

The kaon candidates used for the reconstruction of the D^0 are identified by the χ^2 method described in Sec. 5.1.3. The absolute cut on the $\chi^2(K)$ of the kaon hypothesis requires

$$\chi^2(K) < 8.5. \tag{5.15}$$

It was mentioned in Sec. 3.3.2 that the Čerenkov photons emitted by halo muons constitute a significant source of background. This is especially true for the central region of the RICH around the beam axis. Excluding part of this central region improves the significance of the $D^\star$ signal. The following condition has therefore to be met by the radius of the impact point on the RICH of a given kaon candidate:

$$r_K > 8\,\mathrm{cm}. \tag{5.16}$$

Preparation of the Pion Sample

The pion candidates are tagged using the less strict veto method described in Sec. 5.1.4. The analysis can here profit from the fact that the cut on the mass difference has already

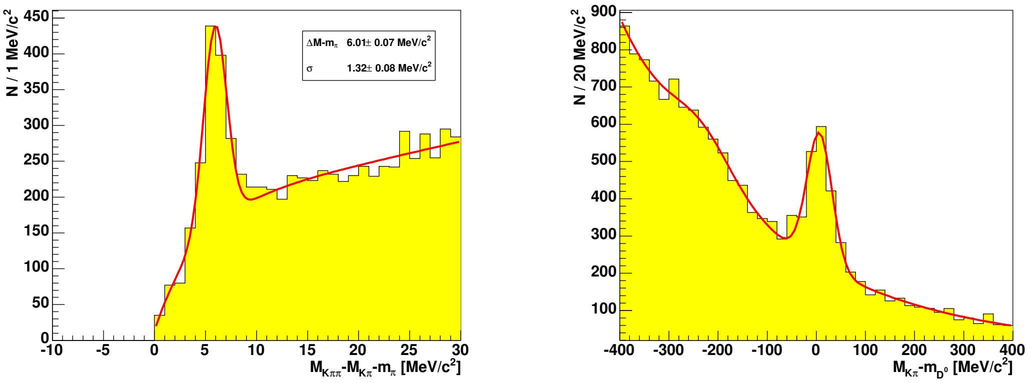

Figure 5.8: The two plots show projections of Fig. 5.7 onto the two axes. For the distribution on the left the interval $\pm 30\,\mathrm{MeV}/c^2$ around $M_{K\pi} - m_{D^0} = 0$ has been projected onto the $\Delta M - m_\pi$ axis. The distribution on the right shows the projection of the interval $3.4\,\mathrm{MeV}/c^2 < \Delta M - m_\pi < 8.6\,\mathrm{MeV}/c^2$ onto the $M_{K\pi} - m_{D^0}$ axis.

removed a lot of background. A cut on the pion momentum

$$p_\pi > 5\,\mathrm{GeV}/c \tag{5.17}$$

removes a region of phase space, where the reconstruction is not optimal especially in view of the momentum resolution. This cut is not applied on those pion candidates which are used as soft pions for the $D^\star$ reconstruction.

5.4.3 Cuts on D^0 Kinematics

A genuine D^0 produced in the photon-gluon fusion process carries a rather large fraction of the available photon energy ν. Assuming that two charmed mesons are produced from the $c\bar{c}$ pair, the energy fraction of a D^0 for example should be of the order of 0.5:

$$z_D = \frac{E_{D^0}}{\nu} \approx \mathcal{O}(0.5). \tag{5.18}$$

This is in contrast to the arbitrary combination of a kaon and a pion, which come from the fragmentation of a quark and thus are part of the background. In this case the fractional energy is expected to be significantly smaller since their production was not directly related to the photon.

A cut on the fractional energy of the D^0 candidate can therefore help to improve the significance of the signal. For the $D^\star$ tagging the cut was chosen to be

$$z_D > 0.26. \tag{5.19}$$

The D^0 is a particle with spin 0 and thus decays isotropically. This means that the distribution of $\cos\theta$ is flat, where θ is the emission angle of the kaon in the rest frame of the D^0 relative to the direction of motion of the D^0 (cf. Fig. 5.9). For an arbitrary

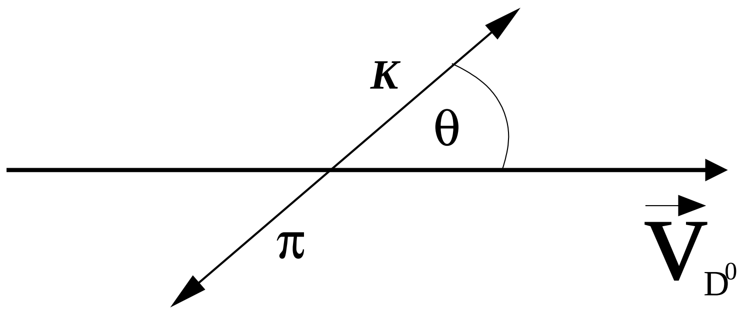

Figure 5.9: A sketch clarifying the definition of the emission angle θ of the kaon in the rest frame of the D^0 relative to the D^0 direction of flight.

combination of pions and kaons from the background, the distribution of $\cos\theta$ is peaked at ± 1. This behaviour is due to the fact that these particles are produced in the fragmentation of quarks, where they get only a small amount of transverse momentum. Since signal and background events give a different $\cos\theta$ distribution, this in principle can be used to suppress background by cutting away regions around $\cos\theta \approx \pm 1$. However, these regions of the distributions are already suppressed by the acceptance of the RICH and the cut on the position of the impact point of the kaon on the RICH. An additional cut yields no improvement of the effective signal in case of the $D^\star$ tagging.

5.5 D^0 Selection

This section describes the reconstruction procedure for D^0s without requiring that they originate from a $D^\star$. In principle the reconstruction approach is similar to the one used for the $D^\star$-tagging method. In many cases, however, the cuts are chosen to be more strict, since with the cut on the mass difference ΔM an efficient tool to suppress background is missing. As in the $D^\star$-tagging method the cuts are tuned to optimise the effective signal defined in Eq. (5.8) and details on the choice of the cuts are given in Sec. B.3.

A D^0 candidate is formed by combining particles which are taken to be a kaon and a pion. The identification procedure for the kaon and pion samples will be described in the following section.

5.5.1 Particle Identification

Kaon Identification

For the identification of kaons the χ^2 method described in Sec. 5.1.3 is used. The absolute cut on the χ^2 of the kaon hypothesis is chosen to be

$$\chi^2(K) < 8. \tag{5.20}$$

A cut on the impact point on the RICH is applied just like in the case of the $D^\star$ tagging. The distance of this point to the z axis has to meet the condition

$$r_K > 18\,\text{cm}. \tag{5.21}$$

Pion Identification

The pions are positively identified using the RICH. For this purpose the χ^2 method described in Sec. 5.1.4 is applied. For those particles above the RICH kaon threshold the absolute cut on the χ^2 of the pion hypothesis is

$$\chi^2(\pi) < 5. \tag{5.22}$$

The sample of pion candidates whose momentum is below the kaon threshold is discarded. This is done because using these particles for the reconstruction of D^0s results in a spectrum of the invariant mass with no hint of a signal.

Additionally, there is a cut on the radius of the impact point on the RICH of

$$r_\pi > 13\,\text{cm}. \tag{5.23}$$

5.5.2 Cuts on D^0 Kinematics

Similar to the $D^\star$-tagging method a cut on the fractional energy of the D^0 candidate is applied:

$$z_D > 0.25. \tag{5.24}$$

The suppression of background by requiring $\cos\theta$ (cf. Fig. 5.9) to lie in a certain interval is here more successful than it was in the case of the $D^\star$ tagging. The interval is chosen to be

$$|\cos\theta| < 0.64. \tag{5.25}$$

5.6 The Final Sample

The reconstruction procedures described above can in principle yield more than one charmed meson per event. However, for the extraction of asymmetries an event should only be counted once. The signal resulting from the $D^\star$-tagging method has a better signal to background ratio. Therefore a D^0 found with this method gets first priority and D^0s from the same event but reconstructed without associated $D^\star$ are removed. This procedure reduces the effective signal of the untagged sample by about 20 % and results in a data sample whose events contain either a $D^\star$-tagged or an untagged D^0. But there are also events which contain more than one candidate from the mentioned categories. This is in principle not surprising, since the $c\bar{c}$ pair can fragment into two charmed mesons. However, it turns out that in most cases the D^0s in question are reconstructed from the same kaon combined with different pions. No unbiased way could be found to choose the correct combination, since the properties of the candidates do not differ significantly. Therefore events with multiple candidates are removed from the sample. The consequence of this is a reduction of the effective signal by about 1 % in the case of the $D^\star$ tagging and about 7 % in that of the untagged D^0s.

The sample of D^0s obtained after these final cuts is shown in Fig. 5.10 for the data from the years 2002 to 2004. The spectra obtained with the $D^\star$ tagging exhibit a bump

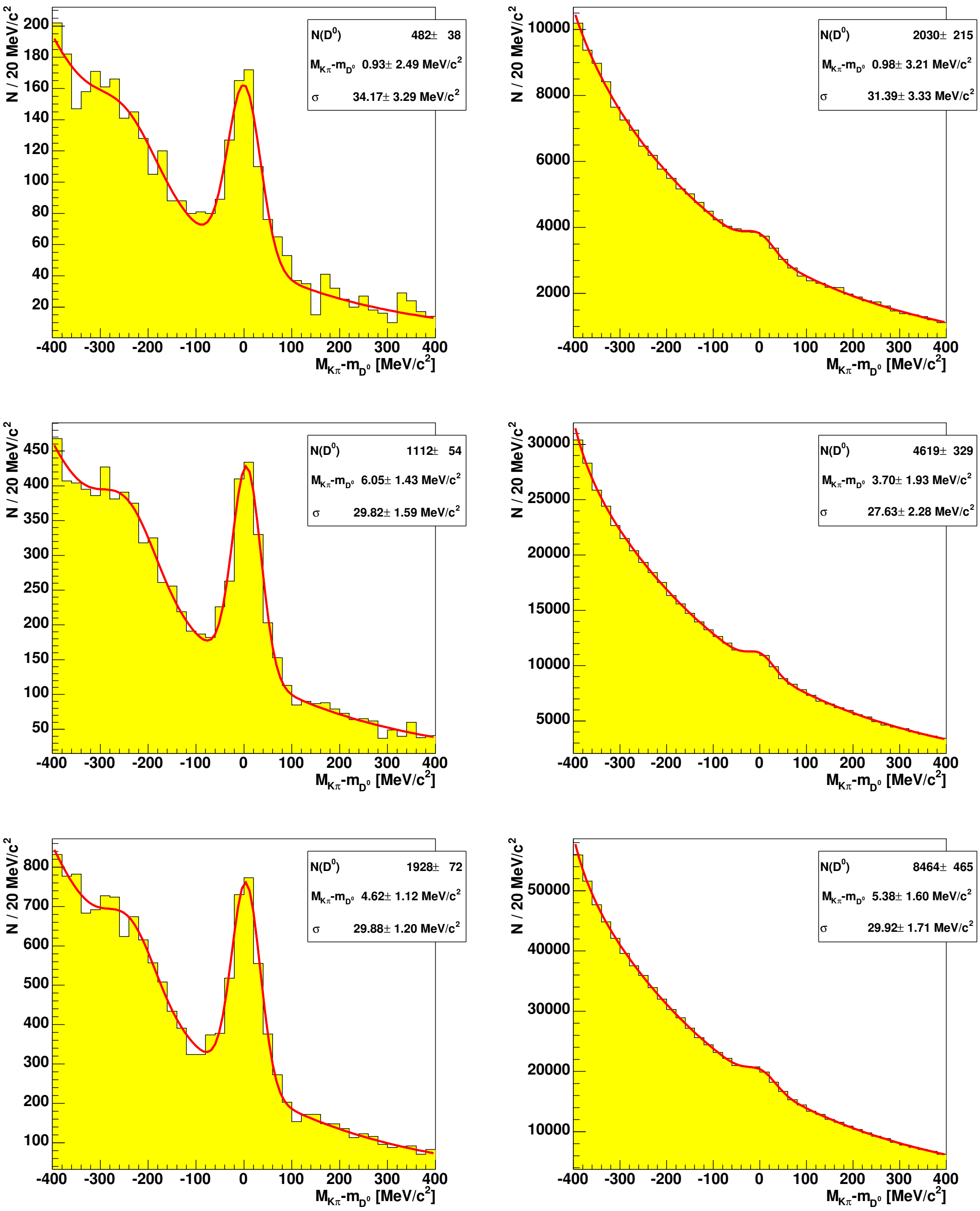

Figure 5.10: The plots show the invariant mass spectra after all cuts for the two categories of D^0s. The left column shows the spectra obtained with the $D^\star$-tagging method and the right column the ones for the untagged D^0s. The spectra in the first row are extracted from the data of 2002 and the ones in the second and third row from the data of 2003 and 2004, respectively. The statistics indicated in the plots have been extracted from a fit to the spectra. Details on the fit functions and the complete set of results of the fit parameters can be found in Sec. B.4. Also the values for the effective signal are summarised in that section.

on the left of the central peak. This feature is a reflection of the decay

$$D^\star \to D^0\pi_S \to K\pi\pi^0\pi_S, \tag{5.26}$$

where the D^0 now decays into a π^0 in addition to the pair of the charged kaon and pion. The neutral pion from this decay can not easily be detected in the COMPASS spectrometer as it was equipped during the years 2002 to 2004. The effect of ignoring the neutral pion in the decay chain of Eq. (5.26) is shown in Fig. 5.11. The result is indeed a reflection at around $M_{K\pi} - m_{D^0} \approx -250$ MeV/c^2.

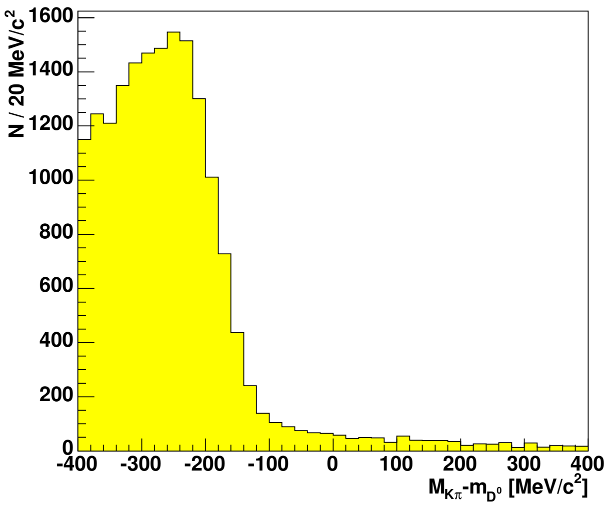

Figure 5.11: The plot shows the reflection of the D^0 decay of Eq. (5.26) extracted from a Monte Carlo simulation. In the simulation only PGF events yielding D^0s are allowed and the mesons are forced to decay via the mentioned decay chain. The data are then reconstructed using the cuts described above, i.e. the π^0 is ignored. The distribution shows a peak at around $M_{K\pi} - m_{D^0} \approx -250$ MeV/c^2. This is also the region where the real data exhibit the bump.

5.6.1 Properties of the Charmed Meson Sample

This section is devoted to the kinematic properties of the event sample presented in Fig. 5.10. Among the interesting quantities are the negative 4-momentum transfer Q^2 and the fractional energy of the virtual photon y, both defined in Chapter 2. In addition to that there are those variables depending on the kinematics of the charmed meson, like its momentum and the momenta of the decay products, but also z_D, the fractional energy of the D^0. Assuming that the distributions of these quantities do not depend strongly on the invariant mass, one can obtain distributions for the signal part of the spectra by using the technique of side-band subtraction. In this approach the distributions obtained from the side bands of the mass spectrum ($|M - m_{D^0}|/(\text{MeV}/c^2) \in [150, 400]$) are subtracted from those extracted from the signal region after being normalised to the number of background events in the signal region taken from the fit. The interval for the signal region is chosen as discussed in Sec. 5.4. Monte Carlo simulations show that the distributions of the mentioned kinematic variables are very similar for D^0s produced directly and D^0s resulting from $D^\star$ decays. Since the $D^\star$ tagged sample yields a cleaner signal than the untagged sample, it is used for the extraction of the distributions. The result for the general event kinematics, namely Q^2 and y is shown in Fig. 5.12. The Q^2 distribution confirms

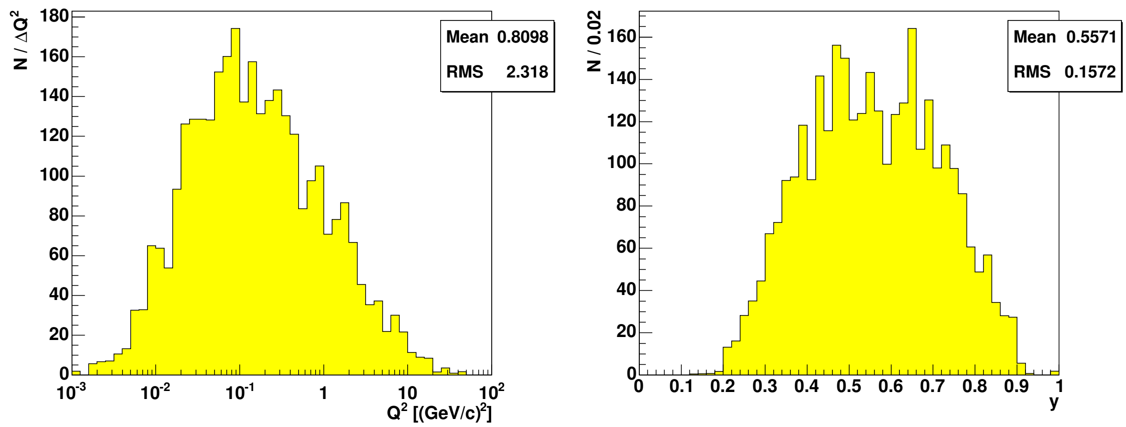

Figure 5.12: The plots show the kinematic properties of the event sample obtained with the $D^\star$-tagging method. All spectra are produced by subtracting distributions from the side bands of the invariant mass spectra.

that really a wide range of the virtual photon spectrum even down to quasi-real photons is exploited in order to detect as many charmed mesons as possible. The fractional photon energy y covers the entire range starting as expected at $y \approx 0.2$ (cf. Sec. 3.3.3).

The momenta of the D^0s and their decay products are shown in Fig. 5.13 together with the momentum of the soft pion from the $D^\star$ decay. As expected from the mass dominated difference between the masses of the $D^\star$ and the D^0, the momentum of the soft pion is very small with a mean of about $3\,\mathrm{GeV}/c$.

The distributions of the fractional energy z_D of the D^0 and its transverse momentum p_t relative to the photon are shown in Fig. 5.14. They are compared to distributions obtained from a Monte Carlo simulation, where $D^\star$s were produced by the AROMA generator and then forced to decay via the golden channel. The spectrometer response is simulated by COMGEANT (cf. Sec. 3.4) and the resulting output is treated analogously to real data.

The agreement between the real data and the Monte Carlo distributions is generally very good, which shows that the sample of charmed mesons collected is really coming from photon-gluon fusion. The mean of the z_D distribution is about 0.5 which corresponds to the expected value. In case of a non-negligible charm content in the nucleon, events with charmed hadrons could result from direct scattering of the photon from a charm quark. In such a process one charmed hadron is found in the final state which now carries most of the energy of the photon and thus has a relatively large fractional energy. From Monte Carlo simulations one would expect a mean value for the fractional energy of the resulting D^0 of above 0.6.

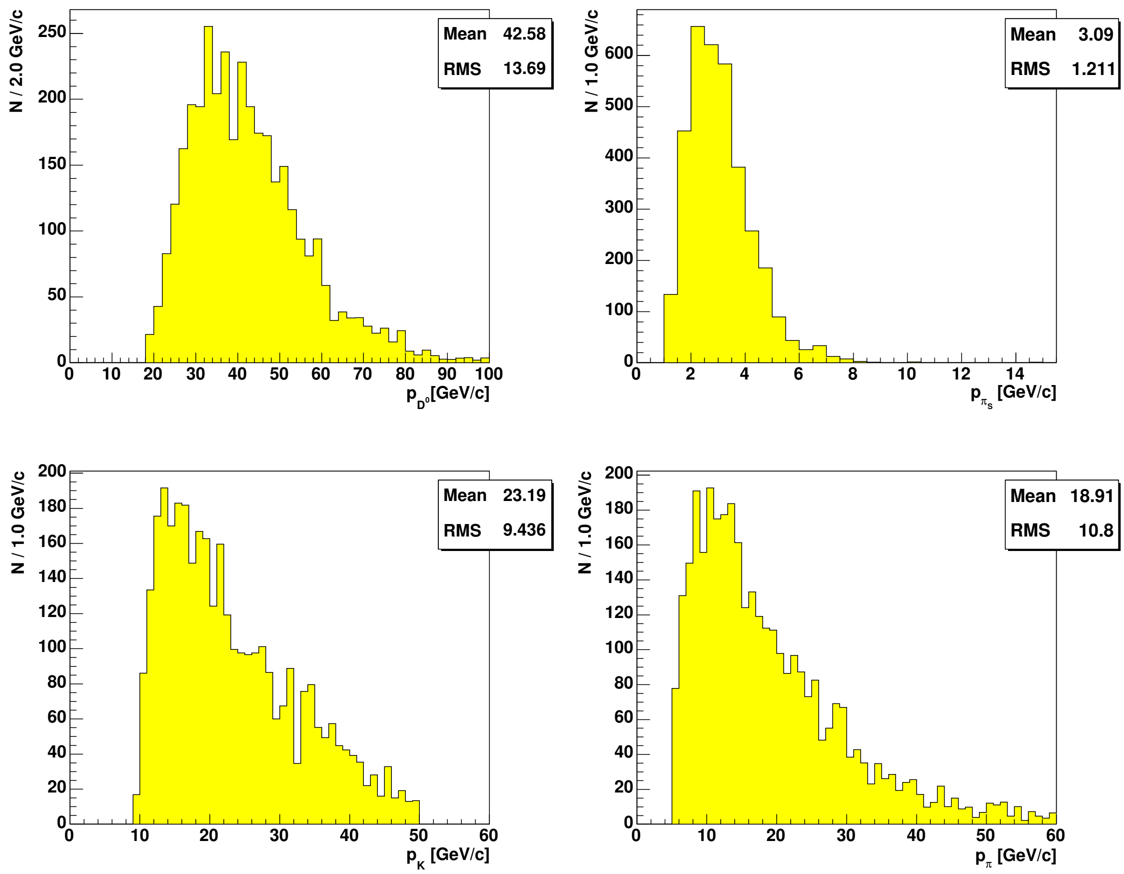

Figure 5.13: The top row shows the momenta of the decay products of the $D^\star$, namely D^0 and soft pion. The bottom row contains the spectra of the momenta of the decay products of the D^0. All spectra are obtained from the $D^\star$-tagged sample by subtracting distributions from the side bands.

For leading order scattering from charm quarks one would in addition expect that the struck quark is typically emitted in the direction of the virtual photon (cf. Sec. 2.5.1). Assuming that in the fragmentation only small amounts of transverse momenta are generated this would result in a distribution of transverse momenta of the charmed meson which is significantly smaller than the one shown in Fig. 5.14.

One can thus conclude that the sample of D^0s reconstructed with the procedure described in this chapter is really generated by photon-gluon fusion. The methods which are used to extract the gluon polarisation from the reconstructed event sample will be the subject of the next chapter.

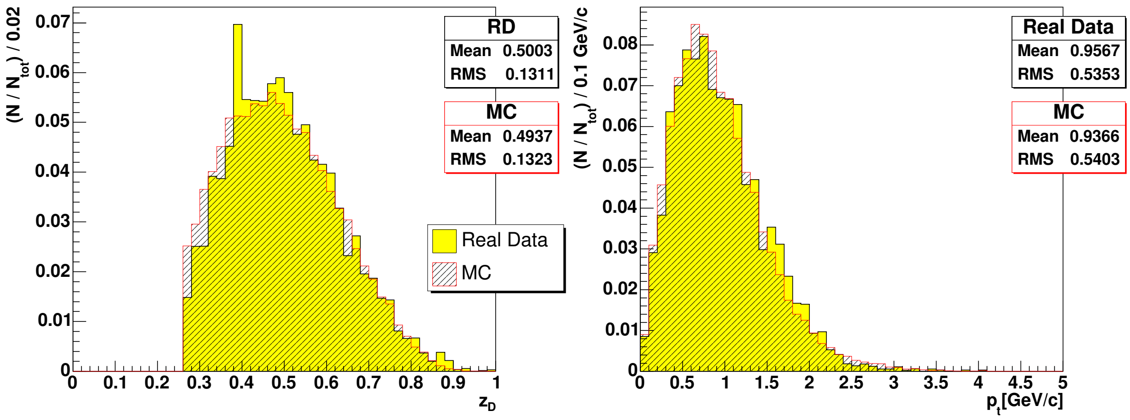

Figure 5.14: The plots show the distributions of z_D, the fractional energy of the D^0 and its transverse momentum p_t relative to the photon. As expected the mean of the z_D distribution is about 0.5. Both spectra agree well with the corresponding distributions extracted from a Monte Carlo simulation. The spectra for the real data are obtained from the $D^\star$-tagged sample by subtracting distributions from the side bands.

Chapter 6

The Extraction of the Gluon Polarisation

The subject of this chapter is the extraction of the gluon polarisation $\Delta G/G$ from a sample of events in which a candidate for a D^0 could be found. The yield of events containing charmed hadrons is given for the upstream target cell by*

$$\begin{aligned} \tilde{N}_u^{c\bar{c}} &= a_u \big\{ \, (\Phi^{\rightarrow} n_u^{\Rightarrow} + \Phi^{\leftarrow} n_u^{\Leftarrow}) \, \sigma_{c\bar{c}}^{\overset{\leftarrow}{\Leftarrow}} + (\Phi^{\rightarrow} n_u^{\Leftarrow} + \Phi^{\leftarrow} n_u^{\Rightarrow}) \, \sigma_{c\bar{c}}^{\overset{\leftarrow}{\Rightarrow}} \\ &\quad + \Phi \sum_A n_A \sigma_{c\bar{c},A} \big\}, \end{aligned} \tag{6.1}$$

where the following quantities enter:

a_u	acceptance of the upstream cell.
$\Phi^{\rightarrow}$, $\Phi^{\leftarrow}$	integrated flux of muons with positive and negative helicity giving the total flux $\Phi = \Phi^{\rightarrow} + \Phi^{\leftarrow}$.
$n_u^{\Rightarrow}$, $n_u^{\Leftarrow}$	number of polarisable nucleons per unit area with positive and negative spin projections onto the beam axis. The total polarisable area density is given by $n_u = n_u^{\Rightarrow} + n_u^{\Leftarrow}$.
$\sigma_{c\bar{c}}^{\overset{\leftarrow}{\Leftarrow}}$, $\sigma_{c\bar{c}}^{\overset{\leftarrow}{\Rightarrow}}$	cross sections for the parallel and antiparallel spin configurations. The spin averaged cross section is defined as $\overline{\sigma}_{c\bar{c}} = 1/2(\sigma_{c\bar{c}}^{\overset{\leftarrow}{\Leftarrow}} + \sigma_{c\bar{c}}^{\overset{\leftarrow}{\Rightarrow}})$.
n_A, $\sigma_{c\bar{c},A}$	the area density of unpolarisable nucleons bound in a nucleus of type A and the corresponding cross section. The contribution to the event yield from the unpolarised nucleons is absorbed in a sum, which runs over all involved types of nuclei A.

An analogous expression holds for the number of events in the downstream cell, $\tilde{N}_d$. In this chapter cell-dependent quantities will be discussed for the case of the upstream cell and the equivalent expressions for the downstream cell are omitted for clarity. The muon-nucleon asymmetry for charmed hadron events is defined as

$$A^{c\bar{c}} = \frac{\sigma_{c\bar{c}}^{\overset{\leftarrow}{\Rightarrow}} - \sigma_{c\bar{c}}^{\overset{\leftarrow}{\Leftarrow}}}{\sigma_{c\bar{c}}^{\overset{\leftarrow}{\Rightarrow}} + \sigma_{c\bar{c}}^{\overset{\leftarrow}{\Leftarrow}}}. \tag{6.2}$$

*In order to simplify the notation the shorthand $c\bar{c}$ is used for $\mu N \rightarrow c\bar{c}$.

The relation between this asymmetry and the event yield can be obtained by re-writing Eq. (6.1):

$$\tilde{N}_u^{c\bar{c}} = a_u \Phi \hat{n}_u \hat{\sigma}_{c\bar{c}} \left(1 - P_\mu P_u f A^{c\bar{c}}\right), \tag{6.3}$$

with the total number of nucleons per unit area $\hat{n}_u = n_u + \sum_A n_A$ and the average total cross section $\hat{\sigma}_{c\bar{c}} = (n_u \overline{\sigma}_{c\bar{c}} + \sum_A n_A \sigma_{c\bar{c},A})/\hat{n}_u$. The beam and target polarisations P_μ and P_t and the dilution factor f in this expression are given by

$$P_\mu = \frac{\Phi^{\rightarrow} - \Phi^{\leftarrow}}{\Phi^{\rightarrow} + \Phi^{\leftarrow}} \qquad P_u = \frac{n_u^{\Rightarrow} - n_u^{\Leftarrow}}{n_u^{\Rightarrow} + n_u^{\Leftarrow}} \qquad f = \frac{n_u \overline{\sigma}_{c\bar{c}}}{n_u \overline{\sigma}_{c\bar{c}} + \sum_A n_A \sigma_{c\bar{c},A}}, \tag{6.4}$$

which means that for positive values of the polarisations the corresponding net spin points along the beam axis.

The mass spectra plotted in Fig. 5.10, however, show that the event sample, which is to be used for the asymmetry extraction does not purely consist of the type $\mu N \rightarrow c\bar{c}$. There is a background contribution in addition, which is taken into account in the event yield by replacing $\hat{\sigma}_{c\bar{c}}$ by $\hat{\sigma}_{\text{tot}} = \hat{\sigma}_{c\bar{c}} + \hat{\sigma}_{\text{Bg}}$. The total event yield is then given by

$$\tilde{N}_u^{\text{tot}} = a_u \Phi \hat{n}_u \hat{\sigma}_{\text{tot}} \left(1 - P_\mu P_u f \frac{\hat{\sigma}_{c\bar{c}}}{\hat{\sigma}_{\text{tot}}} A^{c\bar{c}} - P_\mu P_u f \frac{\hat{\sigma}_{\text{Bg}}}{\hat{\sigma}_{\text{tot}}} A^{\text{Bg}}\right), \tag{6.5}$$

with the asymmetry of the background contribution A^{Bg}.

The event yield $\tilde{N}_u^{\text{tot}}$ depends on a number of variables ξ_i, among the most important are the invariant mass $M_{K\pi}$, the position of the primary vertex $\vec{r}_v$, the energy of the incident muon E_μ and the time t at which the event takes place

$$\vec{\xi} = (M_{K\pi}, \vec{r}_v, E_\mu, t, ...). \tag{6.6}$$

The target polarisation and the beam flux may depend on the time of the event, as does the acceptance, which in addition depends also on the vertex position. The cross sections depend on $M_{K\pi}$ and the event kinematics in general. The diluting factors like the beam polarisation and the dilution factor depend on the kinematics of the muon. A naive analysis proceeds by counting the events from a given target cell in a given mass window, without further classification of the events according to the dependence on $\vec{\xi}$. This means that one measures the integrated event yield

$$N_u^{\text{tot}} = \int \tilde{N}_u^{\text{tot}}(\vec{\xi}) d\vec{\xi} = l_u \langle a_u \rangle \left(1 - \langle \beta_u^{c\bar{c}} \rangle A^{c\bar{c}} - \langle \beta_u^{\text{Bg}} \rangle A^{\text{Bg}}\right), \tag{6.7}$$

with $l_u = \int \Phi \hat{n}_u \hat{\sigma}_{\text{tot}} d\vec{\xi}$. The average acceptance and diluting factors are given by

$$\langle a_u \rangle = \frac{\int a_u \Phi \hat{n}_u \hat{\sigma}_{\text{tot}} d\vec{\xi}}{\int \Phi \hat{n}_u \hat{\sigma}_{\text{tot}} d\vec{\xi}} \qquad \langle \beta_u^i \rangle = \frac{\int a_u \Phi \hat{n}_u \hat{\sigma}_{\text{tot}} P_\mu P_u f \frac{\hat{\sigma}_i}{\hat{\sigma}_{\text{tot}}} d\vec{\xi}}{\int a_u \Phi \hat{n}_u \hat{\sigma}_{\text{tot}} d\vec{\xi}}, \tag{6.8}$$

where $i \in \{c\bar{c}, \text{Bg}\}$. Assuming $\beta A \ll 1$ the average of the diluting factors can be evaluated by $\langle \beta_u^i \rangle \approx \sum_k^{N_u^{\text{tot}}} \beta_{u,k}^i / N_u^{\text{tot}}$ [99]. The sum runs over all events and the approximation holds for large event numbers. If in addition the acceptance is assumed to be equal for signal and for background events the cross-section ratios $\hat{\sigma}_i/\hat{\sigma}_{\rm tot}$ can be expressed as

$$\frac{\hat{\sigma}_{c\bar{c}}}{\hat{\sigma}_{\rm tot}} = \frac{S}{S+B} \quad \text{and} \quad \frac{\hat{\sigma}_{\rm Bg}}{\hat{\sigma}_{\rm tot}} = \frac{B}{S+B}, \tag{6.9}$$

where S and B are parametrisations of the signal and background contributions to the invariant mass spectrum. These parametrisations are in general functions of the invariant mass and the kinematics of the event.

In the following several different methods for the extraction of the charmed hadron asymmetry $A^{c\bar{c}}$ are discussed. The approaches introduced in Secs. 6.1.1 and 6.1.2 are based on the assumption that the asymmetry of the background events $A^{\rm Bg}$ vanishes. It will be discussed in Sec. 7.2.1 to what extent this assumption is justified. A method of asymmetry extraction, which does not rely on the assumption $A^{\rm Bg} = 0$, is subject of Sec. 6.1.3. How the pre-factors of the asymmetry in Eq. (6.5) are obtained is then covered in the subsequent sections along with a discussion of the analysing power $a_{\rm LL}$, which relates the charmed hadron asymmetry to the gluon polarisation.

6.1 Methods for Asymmetry Extraction

6.1.1 First Order Method

The starting point for this method is Eq. (6.7) and the assumption that the background term is zero. The counting rate asymmetry is then given by

$$\begin{aligned} A_N &= \frac{N_u^{\rm tot} - N_d^{\rm tot}}{N_u^{\rm tot} + N_d^{\rm tot}} \\ &= \frac{l_u\langle a_u\rangle - l_d\langle a_d\rangle - (l_u\langle a_u\rangle\langle\beta_u^{c\bar{c}}\rangle - l_d\langle a_d\rangle\langle\beta_d^{c\bar{c}}\rangle)A^{c\bar{c}}}{l_u\langle a_u\rangle + l_d\langle a_d\rangle - (l_u\langle a_u\rangle\langle\beta_u^{c\bar{c}}\rangle + l_d\langle a_d\rangle\langle\beta_d^{c\bar{c}}\rangle)A^{c\bar{c}}}. \end{aligned} \tag{6.10}$$

This expression can be turned into a first order equation in $A^{c\bar{c}}$ by assuming that the acceptance difference between the two target cells is small. This means that the second term in the denominator can be neglected with respect to the first term, since $\langle\beta_u^{c\bar{c}}\rangle \approx -\langle\beta_d^{c\bar{c}}\rangle$.

It was discussed in Sec. 3.2 that for a given microwave setting data are taken in two target spin configurations. In one configuration the target spins point inward ($\Rightarrow\Leftarrow$) and the corresponding asymmetry is called $A_N^{\rm i}$ and in the other configuration the spins point outward ($\Leftarrow\Rightarrow$) resulting in $A_N^{\rm o}$. Computing the mean of the two asymmetries one arrives at

$$A^{c\bar{c}} = -\frac{1}{2\langle\beta\rangle}\left(A_N^{\rm i} - A_N^{\rm o}\right) - A_{\rm false}, \tag{6.11}$$

where $A_{\rm false}$ and $\langle\beta\rangle$ are given by

$$A_{\rm false} = -\frac{1}{2\langle\beta\rangle}\left\{\left(\frac{l_u\langle a_u\rangle - l_d\langle a_d\rangle}{l_u\langle a_u\rangle + l_d\langle a_d\rangle}\right)^{\rm i} - \left(\frac{l_u\langle a_u\rangle - l_d\langle a_d\rangle}{l_u\langle a_u\rangle + l_d\langle a_d\rangle}\right)^{\rm o}\right\} \quad \text{and} \tag{6.12}$$

$$\langle\beta\rangle = \frac{1}{2}\left\{\left(\frac{l_u\langle a_u\rangle\langle\beta_u^{c\bar{c}}\rangle - l_d\langle a_d\rangle\langle\beta_d^{c\bar{c}}\rangle}{l_u\langle a_u\rangle + l_d\langle a_d\rangle}\right)^{\mathrm{i}} - \left(\frac{l_u\langle a_u\rangle\langle\beta_u^{c\bar{c}}\rangle - l_d\langle a_d\rangle\langle\beta_d^{c\bar{c}}\rangle}{l_u\langle a_u\rangle + l_d\langle a_d\rangle}\right)^{\mathrm{o}}\right\}. \quad (6.13)$$

The false asymmetry A_{false} takes into account acceptance variations and vanishes if the following equations are fulfilled

$$\kappa = \frac{\langle a_u^{\mathrm{i}}\rangle\langle a_d^{\mathrm{o}}\rangle}{\langle a_u^{\mathrm{o}}\rangle\langle a_d^{\mathrm{i}}\rangle} = 1 \quad \text{and} \quad \frac{l_u^{\mathrm{i}} l_d^{\mathrm{o}}}{l_u^{\mathrm{o}} l_d^{\mathrm{i}}} = 1. \quad (6.14)$$

The two conditions essentially require that the flux in the two target cells is equal and in addition that the acceptances and the number of nucleons are stable in time.

Assuming equal acceptances of the target cells, i.e. $N/4 \approx N_u^{\mathrm{i(o)}} \approx N_d^{\mathrm{i(o)}}$ the statistical error on the asymmetry is given by

$$\delta A^{c\bar{c}} = \frac{1}{\langle\beta\rangle\sqrt{N}} \quad (6.15)$$

If the ratio $S/(S+B)$ is independent of the other diluting factors it can be pulled out of the average. This yields the relation between the effective signal and the statistical error on the asymmetry used also for Eq. (5.9)

$$\delta A^{c\bar{c}} = \frac{1+B/S}{\langle P_\mu P_t f\rangle\sqrt{N}} = \frac{1}{\langle P_\mu P_t f\rangle}\frac{1}{\sqrt{S_{\mathrm{eff}}}} \quad (6.16)$$

where P_t is the mean of the target polarisations defined in analogy to Eq. (6.13).

6.1.2 Second Order Method

This method is based on the double ratio of counting rates in contrast to the First Order Method which uses a counting rate asymmetry. The double ratio is given by [99]

$$\delta = \frac{(N_u^{\mathrm{tot}})^{\mathrm{i}}(N_d^{\mathrm{tot}})^{\mathrm{o}}}{(N_d^{\mathrm{tot}})^{\mathrm{i}}(N_u^{\mathrm{tot}})^{\mathrm{o}}}, \quad (6.17)$$

where the event yields are defined by Eq. (6.7) together with the assumption that the background asymmetry vanishes. The letters "i" and "o" denote the two target spin configurations of a given microwave setting defined in Sec. 6.1.1. Using the definition in Eq. (6.7) the double ratio reads

$$\delta = \frac{\langle a_u^{\mathrm{i}}\rangle\langle a_d^{\mathrm{o}}\rangle}{\langle a_u^{\mathrm{o}}\rangle\langle a_d^{\mathrm{i}}\rangle}\frac{l_u^{\mathrm{i}} l_d^{\mathrm{o}}}{l_u^{\mathrm{o}} l_d^{\mathrm{i}}}\frac{\left(1-\langle\beta_u^{c\bar{c},\mathrm{i}}\rangle A^{c\bar{c}}\right)\left(1-\langle\beta_d^{c\bar{c},\mathrm{o}}\rangle A^{c\bar{c}}\right)}{\left(1-\langle\beta_d^{c\bar{c},\mathrm{i}}\rangle A^{c\bar{c}}\right)\left(1-\langle\beta_u^{c\bar{c},\mathrm{o}}\rangle A^{c\bar{c}}\right)}. \quad (6.18)$$

Applying the same assumptions on the stability of acceptance, flux and number of nucleons in the target cells with respect to the two spin configurations as for the First Order Method (cf. Eq. (6.14)) one obtains a second order equation in $A^{c\bar{c}}$. This equation is given by

$$a\left(A^{c\bar{c}}\right)^2 - bA^{c\bar{c}} + c = 0, \quad (6.19)$$

with the parameters

$$a = \delta\langle\beta_u^{c\bar{c},\mathrm{o}}\rangle\langle\beta_d^{c\bar{c},\mathrm{i}}\rangle - \langle\beta_u^{c\bar{c},\mathrm{i}}\rangle\langle\beta_d^{c\bar{c},\mathrm{o}}\rangle \quad (6.20)$$

$$b = \delta\left(\langle\beta_u^{c\bar{c},\mathrm{o}}\rangle + \langle\beta_d^{c\bar{c},\mathrm{i}}\rangle\right) - \left(\langle\beta_u^{c\bar{c},\mathrm{i}}\rangle + \langle\beta_d^{c\bar{c},\mathrm{o}}\rangle\right) \quad (6.21)$$

$$c = \delta - 1 \quad (6.22)$$

The solution of the second order equation is

$$A = \frac{\pm\sqrt{b^2 - 4ac + b}}{2a}, \quad (6.23)$$

where the sign is determined by the type of microwave setting (cf. Fig. 3.6). The Second Order Method can thus extract the asymmetry without the assumption of equal acceptances of the two target cells, which was needed in the case of the First Order Method. This is an important advantage especially in view of the fact that in the open charm analysis the acceptance ratio of downstream cell over upstream cell is of the order of 1.5 to 2.

In the method described so far every event enters the analysis with the same weight. This is not optimal, since events with a small $\beta_{u(d)}$ carry less information about the asymmetry than those with large pre-factors. A weighting of events can be introduced by modifying Eq. (6.7)

$$N_u^w = \int w(\vec{\xi})\tilde{N}_u^{\mathrm{tot}}(\vec{\xi})d\vec{\xi} = l_u\langle a_u\rangle_w\left(1 - \langle\beta_u^{c\bar{c}}\rangle_w A^{c\bar{c}}\right), \quad (6.24)$$

where the background asymmetry has already been neglected at this stage for simplicity. The meaning of l_u is the same as before, but the average acceptance and diluting factors are now given by

$$\langle a_u\rangle_w = \frac{\int w a_u \Phi \hat{n}_u \hat{\sigma}_{\mathrm{tot}} d\vec{\xi}}{\int \Phi \hat{n}_u \hat{\sigma}_{\mathrm{tot}} d\vec{\xi}} \qquad \langle\beta_u^i\rangle_w = \frac{\int w a_u \Phi \hat{n}_u \hat{\sigma}_{\mathrm{tot}} P_\mu P_u f \frac{S}{S+B} d\vec{\xi}}{\int w a_u \Phi \hat{n}_u \hat{\sigma}_{\mathrm{tot}} d\vec{\xi}} \quad (6.25)$$

and the latter can approximately be evaluated by $\langle\beta_u^{c\bar{c}}\rangle_w \approx \sum_k \beta_{u,k}^{c\bar{c}} / \sum_k w_k$. Using the weighted event yields, the double ratio reads

$$\delta = \frac{(N_u^w)^{\mathrm{i}}(N_d^w)^{\mathrm{o}}}{(N_d^w)^{\mathrm{i}}(N_u^w)^{\mathrm{o}}}, \quad (6.26)$$

and the method can proceed in analogy to the unweighted case.

The statistically optimal weight is $w = \beta_{u(d)}^{c\bar{c}}$ [99]. In order to estimate the gain achieved through the weighting, one needs to compare the statistical errors for the weighted and the unweighted case. Using the weight defined above and assuming equal acceptances of the target cells and equal pre-factors ($\beta_u^{c\bar{c}} \approx \beta_d^{c\bar{c}}$) they are given as

$$\delta A_w^{c\bar{c}} = \frac{1}{\sqrt{\langle(\beta_{u(d)}^{c\bar{c}})^2\rangle N}} \quad \text{and} \quad \delta A^{c\bar{c}} = \frac{1}{\sqrt{\langle\beta_{u(d)}^{c\bar{c}}\rangle^2 N}}. \quad (6.27)$$

Thus the statistical error can be reduced by a factor given by

$$\sqrt{\frac{\langle(\beta^{c\bar{c}}_{u(d)})^2\rangle}{\langle\beta^{c\bar{c}}_{u(d)}\rangle^2}}. \tag{6.28}$$

Applying a weight $w = \beta^{c\bar{c}}_{u(d)}$, however, means that κ depends on the target polarisation. As mentioned above, this polarisation may be time dependent and one can realistically assume that the dependence is not equal for the two target cells. This implies that even in the case of perfectly stable acceptances the condition $\kappa = 1$ is not fulfilled. As a consequence the target polarisation is excluded from the weight in order to limit systematic effects.

6.1.3 Fit Method

The method derived in this section is not based on the assumption that the background asymmetry vanishes. Instead it allows for the simultaneous extraction of the signal and background asymmetries [100, 101].

The integrated event yield in the upstream target cell is given by an expression similar to Eq. (6.24)

$$N_u^{w_S} = \int w_S \tilde{N}_u^{\rm tot}(\vec{\xi})d\vec{\xi} \quad \text{with} \quad w_S = P_\mu f \frac{S}{S+B}, \tag{6.29}$$

where the signal weight is now explicitly marked with an index for reasons which will become clear later in this section. The event yield $\tilde{N}_u^{\rm tot}(\vec{\xi})$ is expressed similarly to Eq. (6.5) and reads

$$\tilde{N}_u^{\rm tot}(\vec{\xi}) = a_u \Phi \hat{n}_u \hat{\sigma}_{\rm tot}\left(1 - \hat{\beta}_u \frac{S}{S+B}A^{c\bar{c}} - \hat{\beta}_u \frac{B}{S+B}A^{\rm Bg}\right), \tag{6.30}$$

with $\hat{\beta}_u = P_\mu P_u f$. Assuming that the asymmetries are largely independent of $\vec{\xi}$, one can rewrite Eq. (6.29) as

$$\begin{aligned} N_u^{w_S} &= \int w_S \tilde{\alpha}_u \hat{\sigma}_{\rm tot} d\vec{\xi} - A^{c\bar{c}} \int w_S \tilde{\alpha}_u \hat{\beta}_u \hat{\sigma}_{\rm tot} \frac{S}{S+B} d\vec{\xi} \\ &\quad - A^{\rm Bg} \int w_S \tilde{\alpha}_u \hat{\beta}_u \hat{\sigma}_{\rm tot} \frac{B}{S+B} d\vec{\xi} && (6.31) \\ &= I_u^S \left(1 - A^{c\bar{c}} \frac{F_u^{SS}}{I_u^S} - A^{\rm Bg} \frac{F_u^{SB}}{I_u^S}\right), && (6.32) \end{aligned}$$

where

$$\tilde{\alpha}_u = a_u \Phi \hat{n}_u \tag{6.33}$$

$$I_u^S = \int w_S \tilde{\alpha}_u \hat{\sigma}_{\rm tot} d\vec{\xi} \tag{6.34}$$

$$F_u^{SS} = \int w_S \tilde{\alpha}_u \hat{\beta}_u \hat{\sigma}_{\rm tot} \frac{S}{S+B} d\vec{\xi} \tag{6.35}$$

$$F_u^{SB} = \int w_S \tilde{\alpha}_u \hat{\beta}_u \hat{\sigma}_{\mathrm{tot}} \frac{B}{S+B} d\vec{\xi}. \tag{6.36}$$

In analogy to Eq. (6.32) four expressions can be obtained for the two target cells and the two spin configurations ("inner" and "outer").

Using a background weight w_B given by

$$w_B = P_\mu f \frac{B}{S+B}, \tag{6.37}$$

four more equations can be derived. The equivalent to Eq. (6.31) then reads

$$\begin{aligned} N_u^{w_B} &= \int w_B \tilde{\alpha}_u \hat{\sigma}_{\mathrm{tot}} d\vec{\xi} - A^{c\bar{c}} \int w_B \tilde{\alpha}_u \hat{\beta}_u \hat{\sigma}_{\mathrm{tot}} \frac{S}{S+B} d\vec{\xi} \\ &\quad - A^{\mathrm{Bg}} \int w_B \tilde{\alpha}_u \hat{\beta}_u \hat{\sigma}_{\mathrm{tot}} \frac{B}{S+B} d\vec{\xi} \qquad (6.38) \\ &= I_u^B \left(1 - A^{c\bar{c}} \frac{F_u^{BS}}{I_u^B} - A^{\mathrm{Bg}} \frac{F_u^{BB}}{I_u^B} \right), \qquad (6.39) \end{aligned}$$

where I_u^B, F_u^{BS} and F_u^{BB} are defined in analogy to Eqs. (6.34–6.36). The weighted event yield N_u^{ws} can be approximately obtained by $N_u^{ws} \approx \sum_k^{N_u^{\mathrm{tot}}} w_{S,k}$ and F_u^{SS}/I_u^S is approximated by

$$\begin{aligned} \frac{F_u^{SS}}{I_u^S} &= \frac{\int w_S \tilde{\alpha}_u \hat{\beta}_u \hat{\sigma}_{\mathrm{tot}} \frac{S}{S+B} d\vec{\xi}}{\int w_S \tilde{\alpha}_u \hat{\sigma}_{\mathrm{tot}} d\vec{\xi}} \qquad (6.40) \\ &\approx \frac{\sum_k^{N_u^{\mathrm{tot}}} w_{S,k} \hat{\beta}_u \frac{S}{S+B} d\vec{\xi}}{\sum_k^{N_u^{\mathrm{tot}}} w_{S,k}}. \qquad (6.41) \end{aligned}$$

Analogous equations hold for F_u^{SB}/I_u^S and the corresponding quantities entering Eq. (6.39). This means that there are eight equations for eight unknown parameters, which are $A^{c\bar{c}}$, A^{Bg}, $(I_u^S)^{\mathrm{i}}$, $(I_d^S)^{\mathrm{i}}$, $(I_u^S)^{\mathrm{o}}$, $(I_u^B)^{\mathrm{i}}$, $(I_d^B)^{\mathrm{i}}$, $(I_u^B)^{\mathrm{o}}$, where the condition $\kappa = 1$ (cf. Eq. (6.14)) was used to fix $(I_d^S)^{\mathrm{o}}$ and $(I_d^B)^{\mathrm{o}}$. The set of equations can thus be solved to give the signal and background asymmetries $A^{c\bar{c}}$ and A^{Bg}. More details on this method are given in the appendix (Sec. C.1).

6.2 Data Grouping

All the methods for asymmetry extraction discussed in Sec. 6.1 have in common that they take as input the event numbers from the two target cells for the two spin configurations, which correspond to the two orientations of the solenoid field (cf. Fig. 3.6). Thus the data have to be grouped accordingly in order to extract asymmetries. One way to do this grouping is to combine runs taken before and after a given reversal of the solenoid field. This is called the consecutive grouping and is explained schematically in Fig. 6.1 (left). This way of data grouping has the advantage that the time interval in which the combined data have been taken is relatively short and that therefore the spectrometer is likely to be stable. This means that residual false asymmetries due to variations of the acceptance with time are suppressed.

However, for this analysis the resulting event numbers for a given target cell and a given spin configuration can be very small for the consecutive configuration. In such a situation the use of the Second Order Method (cf. Sec. 6.1.2) would be doubtful (cf. Eq. (6.8) and the discussion thereafter).

The lack of events can be cured by applying the so-called global way of combining the data. In this mode the data taken around several reversals of the solenoid field are combined for the asymmetry extraction (cf. Fig. 6.1 (right)). Typically the data from one data-taking period are combined together, but care is taken to split periods with large interruptions (e.g. 02P2G, 03P1D). In the global configuration there is the risk that false asymmetries due to possible variations of the spectrometer acceptance with time are not as well suppressed as in the case of the consecutive configuration. However, studies performed in the course of different analyses like the A_1 extraction or the high-p_t approach to measure $\Delta G/G$ have shown that there are no significant effects (cf. e.g. [97]). In the light of these studies and the current statistical accuracy of the open-charm approach the conclusion is that the global configuration can safely be used.

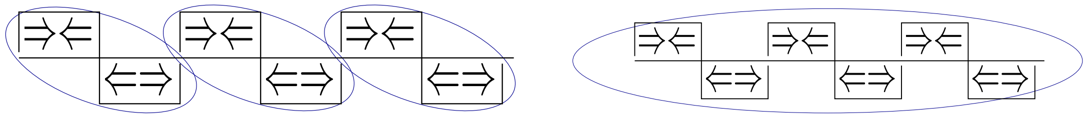

Figure 6.1: A schematic definition of two ways of data grouping for asymmetry extraction. On the left the data before and after a given solenoid-field reversal are grouped together. This is called consecutive configuration. On the right the data around several field reversals are grouped together, which is referred to as the global configuration. Typically the data from one data-taking period are grouped together in this mode.

6.3 Diluting Factors

6.3.1 Beam and Target Polarisation

The polarisation of the beam muons is obtained on an event-by-event basis from a parametrisation, which gives the polarisation as a function of the beam momentum. The mean value of the beam polarisation is -0.76 and -0.81 for the years 2002/2003 and 2004, respectively, with a relative error of 5 % (cf. Sec. 3.1 and Fig. 3.2).

The target polarisation is measured by five NMR coils along each target cell every 10–15 minutes. These measurements are then averaged to obtain the value for a given run, which typically takes 30–60 minutes (cf. 3.2 and Fig. 3.5). Averaged over the three years of data taking 2002 to 2004, one obtains for the polarisation a mean value of 51 % for the upstream cell and 50 % for the downstream cell with a relative error of 5 %. Only runs which are actually used in this analysis have entered in these statistics. Typically data are only recorded if the target polarisation is above a minimum polarisation. Due to this, the smallest polarisation values occurring in this analysis are 32 %, whereas the largest values amount to 57 %. In case a given run does not have a polarisation measurement because of technical problems, the values from neighbouring runs are linearly interpolated. This rescue procedure had to be applied for about 7 % of the runs.

6.3.2 Dilution Factor

The dilution factor (cf. Eq. (6.4)) gives the fraction of interactions in polarisable material. In a naive picture the target cells are completely filled with ^{6}LiD and the ^{6}Li nucleus is interpreted as a system comprised of an alpha particle and a deuterium nucleus (cf. Sec. 3.2). These assumptions yield a naive expectation for the dilution factor of 0.5. However, besides ^{6}LiD there are also other materials found in the volumes of the target cells. Mainly there is the ^{3}He-^{4}He responsible for the cooling of the target material, but also C, F, Ni and Cu are present, introduced by the NMR coils. All these materials need to be included in the computation of the dilution factor. Apart from the number of nucleons bound in the nuclei of a given type also the corresponding cross sections enter the dilution factor. This means that it depends on the event kinematics and among these mainly on x, which has been defined in Eq. (2.7). The dilution factor is given by a parametrisation as a function of x and y and is thus available on an event-by-event basis [102]. Averaged over the event sample used for the extraction of the gluon polarisation the mean value of the dilution factor is $\langle f \rangle = 0.40$. The uncertainties on the involved cross sections as well as the uncertain target composition enter in the error on the dilution factor, which amounts to 5 %.

6.3.3 Analysing Power

Definition of the Analysing Power

The analysing power is here defined as the ratio of the spin-dependent and the spin-averaged muon-gluon cross sections:

$$a_{\mathrm{LL}} = \frac{\Delta\sigma_{\mu g \to c\bar{c}}}{\sigma_{\mu g \to c\bar{c}}}. \tag{6.42}$$

It relates the muon-nucleon asymmetry to the gluon polarisation via

$$A^{c\bar{c}} = a_{\mathrm{LL}} \frac{\Delta G}{G}. \tag{6.43}$$

Referring to the formalism in Sec. 2.5.1 (cf. Eq. (2.70)) the analysing power a_{LL} incorporates the depolarisation factor D and the partonic asymmetry $\hat{a}_{\mathrm{LL}}$. The expression in Eq. (6.43) is an approximation of the convolution in Eq. (2.64). It was checked that this approach does not lead to a significant distortion of the result. This was done for the case of light quarks (A_1) [103] and it is expected that this result can be extended to charm quarks.

The cross sections in Eq. (6.42) have been calculated to first order in α_s [103]. They depend on a number of kinematic variables and the charm-quark mass m_c

$$(\Delta)\sigma_{\mu g \to c\bar{c}}(x, Q^2, x_p, z_q, \phi, m_c), \tag{6.44}$$

where the inclusive variables x and Q^2 have been defined in Sec. 2.1.1 and x_p, z_q and ϕ depend on the fraction of nucleon momentum η carried by the interacting gluon and the 4-momenta of the proton, the virtual photon and the charm quark in the final state, $\mathbf{P}$, $\mathbf{q}$ and $\mathbf{P}_q$, via

$$x_p = \frac{x}{\eta} \qquad z_q = \frac{\mathbf{P}\cdot\mathbf{P}_q}{\mathbf{P}\cdot\mathbf{q}} \qquad \phi = \frac{(\mathbf{P}\times\mathbf{k})\cdot(\mathbf{P}\times\mathbf{P}_q)}{|\mathbf{P}\times\mathbf{k}||\mathbf{P}\times\mathbf{P}_q|}. \tag{6.45}$$

The complete equations are given in the appendix (Sec. C.2). The analysing power thus depends not only on the kinematics of the virtual photon, but also on the parton kinematics. Since only one charmed meson is reconstructed, the kinematics of the parton system are not exactly measurable. This, however, means that the true analysing power, computed with the complete kinematics of the event, is not available either.

The distribution of the analysing power extracted from a Monte Carlo simulation is shown in Fig. 6.2. For this simulation D^0s have been generated with AROMA and are

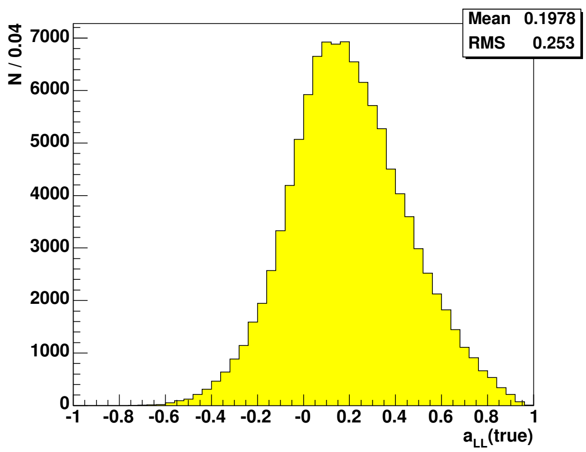

Figure 6.2: The analysing power $a_{\rm LL}$ as obtained from a Monte Carlo simulation of D^0 decays. For the distribution a charm-quark mass of 1500 MeV$/c^2$ was used.

forced to decay via the $K\pi$ channel. After simulation of the spectrometer response with COMGEANT (cf. Sec. 3.4) the events are then reconstructed like real data with the difference that the parton kinematics (η, z_q and ϕ) are available and can be used for the computation of the analysing power. For the plot in Fig. 6.2 a charm-quark mass of 1500 MeV$/c^2$ was used. A discussion of the dependence of the analysing power on this parameter will follow in the last part of this section. The cross sections which enter the analysing power are calculated to first order in α_s. In order to be consistent, care is taken that also the simulation is strictly leading order. Therefore parton showers have been switched off in the generator, since they are used to model next-to-leading order processes.

The distribution of the analysing power shows that the quantity changes sign in the accessible kinematic range. This means that it can take on small values even down to zero and as a consequence the corresponding events do not carry any information on the gluon polarisation. It is therefore desirable to have the analysing power available on an event-by-event basis in order to use it as an event weight.

Parametrisation of the Analysing Power

A possibility to provide the needed value of the analysing power is to produce a parametrisation from Monte Carlo. This parametrisation has to map the partonic quantities on which the analysing power actually depends onto reconstructable variables.

The starting point of the extraction of the parametrisation is a Monte Carlo simulation as described above. The main dependence on the photon kinematics is absorbed in a pre-factor as shown in the following factorisation

$$a_{\mathrm{LL}} = \frac{1-(1-y)^2}{1+(1-y)^2}\tilde{a}_{\mathrm{LL}}. \tag{6.46}$$

The residual dependencies are then mapped onto the fractional energy z_D of the D^0 and its transverse momentum p_t relative to the virtual photon. This is done by determining $\tilde{a}_{\mathrm{LL}}$ on a grid in z_D and p_t and using these values as input to a spline fit. The values of $\tilde{a}_{\mathrm{LL}}$ on this grid are included in the appendix (Sec. C.3). This procedure results in a parametrisation of the analysing power, which depends on y, p_t and z_D: $a_{\mathrm{LL}}^{\mathrm{par}}(y, p_t, z_D)$. Finally a multiplicative correction factor of about 3 % is applied in order to adjust the mean value.

A comparison of the true analysing power to the value obtained from the parametrisation is shown in Fig. 6.3. The correlation obtained between the two values is 0.78.

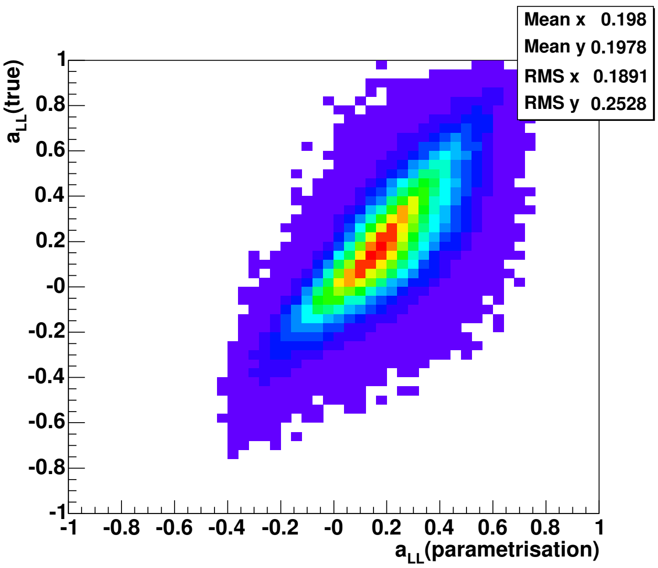

Figure 6.3: The true analysing power is plotted versus the value obtained from the parametrisation. A clear correlation is visible.

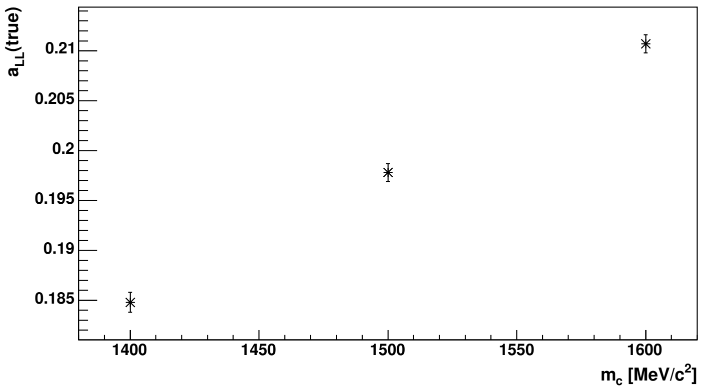

Figure 6.4: The mean value of the true analysing power is plotted versus the charm quark mass. The value $m_c = 1500\,\mathrm{MeV}/c^2$ is favoured by cross section measurements, however, variations of $\pm 100\,\mathrm{MeV}/c^2$ are not excluded.

Dependence on the Mass of the Charm Quark

The equations quoted in Sec. C.2 reveal a dependence of the analysing power on the mass of the charm quark. The charm-quark mass may for example be determined from measurements of the total charm production cross section. A comparison of this cross section to the expectation for a given charm-quark mass allows an estimation of the parameter. The most favoured value† is $m_c = 1500\,\mathrm{MeV}/c^2$, but variations of the order of $\pm 100\,\mathrm{MeV}/c^2$ are not excluded [104].

The mean values of the analysing power for charm-quark masses of $1400\,\mathrm{MeV}/c^2$, $1500\,\mathrm{MeV}/c^2$ and $1600\,\mathrm{MeV}/c^2$ are shown in Fig. 6.4 and summarised in Tab. 6.1. The quantities have been obtained from a Monte Carlo simulation as described above. Parametrisations were produced for all three mass values. The gluon polarisation will be extracted using the cental value of $m_c = 1500\,\mathrm{MeV}/c^2$. The other configurations will be used for an estimation of the dependence of $\Delta G/G$ on the mass of the charm quark, which will then enter in the systematic uncertainty of the final result of this analysis.

Table 6.1: Summary of the mean values for the analysing power obtained for different values of the charm-quark mass. The true values of the analysing power are presented as well as the values obtained from a parametrisation $a_{\mathrm{LL}}^{\mathrm{par}}(y, p_t, z_D)$.

m_c [MeV/c^2]	true a_{LL}	$a_{\mathrm{LL}}^{\mathrm{par}}$
1400	0.1831 ± 0.0010	0.1831 ± 0.0009
1500	0.1978 ± 0.0009	0.1980 ± 0.0007
1600	0.2115 ± 0.0011	0.2099 ± 0.0009

†The pole mass of the charm quark cited here is about 20 % larger than the current or bare quark mass given in [6].

6.3.4 Signal to Background Ratio

The methods for the asymmetry extraction presented in Secs. 6.1.1 to 6.1.3 rely on the knowledge of pre-factors absorbed in $\langle\beta^{c\bar{c}}_{u(d)}\rangle$ with

$$\langle\beta^{c\bar{c}}_{u(d)}\rangle = \langle P_\mu P_{u(d)} f \frac{S}{S+B}\rangle. \tag{6.47}$$

For the extraction of the gluon polarisation these factors need to be supplemented with the analysing power according to Eq. (6.43), giving

$$\langle\beta^{c\bar{c}}_{u(d)}\rangle = \langle P_\mu P_{u(d)} f a_{\rm LL} \frac{S}{S+B}\rangle. \tag{6.48}$$

The plots in Fig. 6.5 show a comparison of the distributions of z_D and p_t from the signal part of the invariant mass spectrum to those extracted from the sidebands of the spectrum. For this purpose the distribution for the signal is obtained via sideband subtraction as described in Sec. 5.6.1. In the plots a shift between the distributions is clearly visible. This shift between the distributions indicates that the $S/(S+B)$ term depends among others on the kinematic variables z_D and p_t. As discussed in Sec. 6.3.3 the parametrisation of the analysing power $a_{\rm LL}$ also depends on these variables

$$\langle\beta^{c\bar{c}}_{u(d)}\rangle = \langle P_\mu P_{u(d)} f a_{\rm LL}(z_D, p_t) \frac{S}{S+B}(z_D, p_t)\rangle. \tag{6.49}$$

In a naive analysis $S/(S+B)$ is extracted from a fit to global mass spectra, such as the ones in Fig. 5.10. However, this means that $(S/(S+B))(z_D, p_t)$ is averaged over the event sample and the mean of the pre-factors is effectively given as

$$\langle\beta^{c\bar{c}}_{u(d)}\rangle = \langle P_\mu P_{u(d)} f a_{\rm LL}(z_D, p_t)\rangle\langle \frac{S}{S+B}(z_D, p_t)\rangle. \tag{6.50}$$

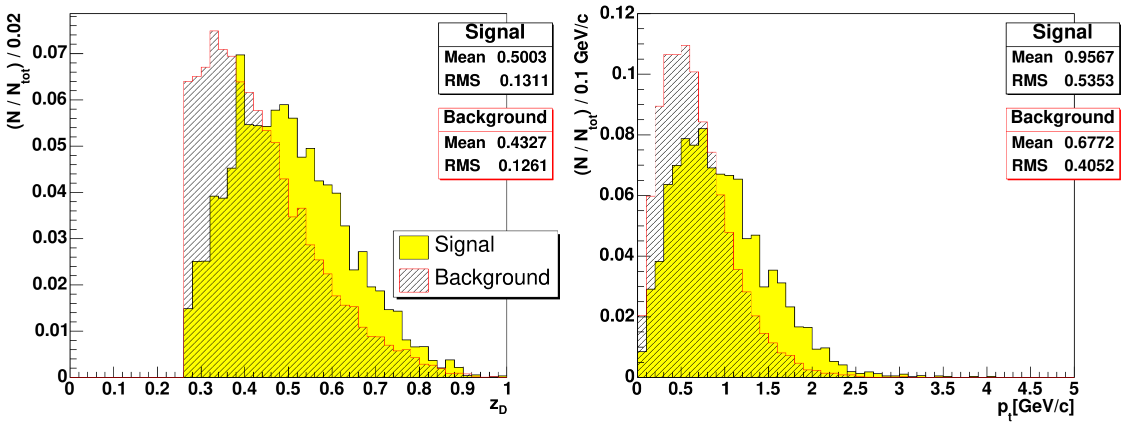

Figure 6.5: The plots show the distributions of z_D and p_t as extracted from the sideband-subtracted signal region and those from the background. A shift between the signal and the background distributions is visible.

Such a naive extraction thus suffers from a bias introduced by ignoring the implicit correlation between the analysing power and the $S/(S+B)$ factor.

This bias can be avoided by parametrising the signal and background contributions not only as a function of the invariant mass, but also as a function of the most important kinematic variables such as z_D and p_t. However, this approach is not feasible, since the available statistics is not sufficient. Alternatively, the parametrisation of $S/(S+B)$ is obtained as a function of only one variable which absorbs all dependencies, namely $fP_\mu a_{\mathrm{LL}}$.

The distribution of $fP_\mu a_{\mathrm{LL}}$ is shown in Fig. 6.6 for the $D^\star$ tagged sample. All events contained in the spectra of Fig. 5.10 are also included in this distribution. The binning for

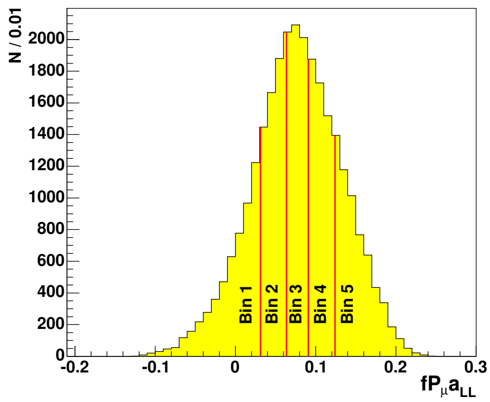

Figure 6.6: The distribution of $fP_\mu a_{\mathrm{LL}}$ for $D^\star$ tagged events for the complete data sample. All events that entered the corresponding spectra in Fig. 5.10 are included in this distribution. The bins used for the parametrisation of $S/(S+B)$ are indicated.

the parametrisation is arranged such that the events are distributed evenly. The resulting bins are indicated in the distribution shown in Fig. 6.6. The number of bins was chosen such that the dependence of the analysing power on e.g. p_t in the respective bin is minimised and on the other hand the statistics is sufficient to yield a reliable fit.

The invariant mass spectra in these bins of $fP_\mu a_{\mathrm{LL}}$ are shown in Fig. 6.7. The decrease of the signal-to-background ratio is clearly visible. In order to quantify the effect, the ratio was determined in a mass window around the nominal D^0 mass and the result is summarised in Tab. 6.2. It should be stressed that these values are meant only for the illustration of the effect. In the actual analysis the $S/(S+B)$ factor is evaluated on an event-by-event basis at the corresponding invariant mass.

For the untagged event sample a similar approach is used. In this case the number of bins is chosen to be three due to the less prominent signal compared to the $D^\star$ tagged case, which makes the fit more difficult. The signal-to-background values as determined from a mass window around the signal are also summarised in Tab. 6.2. The actual positions of the bins and the complete set of fit parameters in the different bins for the two event samples are summarised in the appendix (Sec. C.4).

As discussed above, the parametrisation of the signal-over-background ratio was done as a function of $fP_\mu a_{\mathrm{LL}}$ instead of p_t and z_D due to a lack of statistics. The correlation

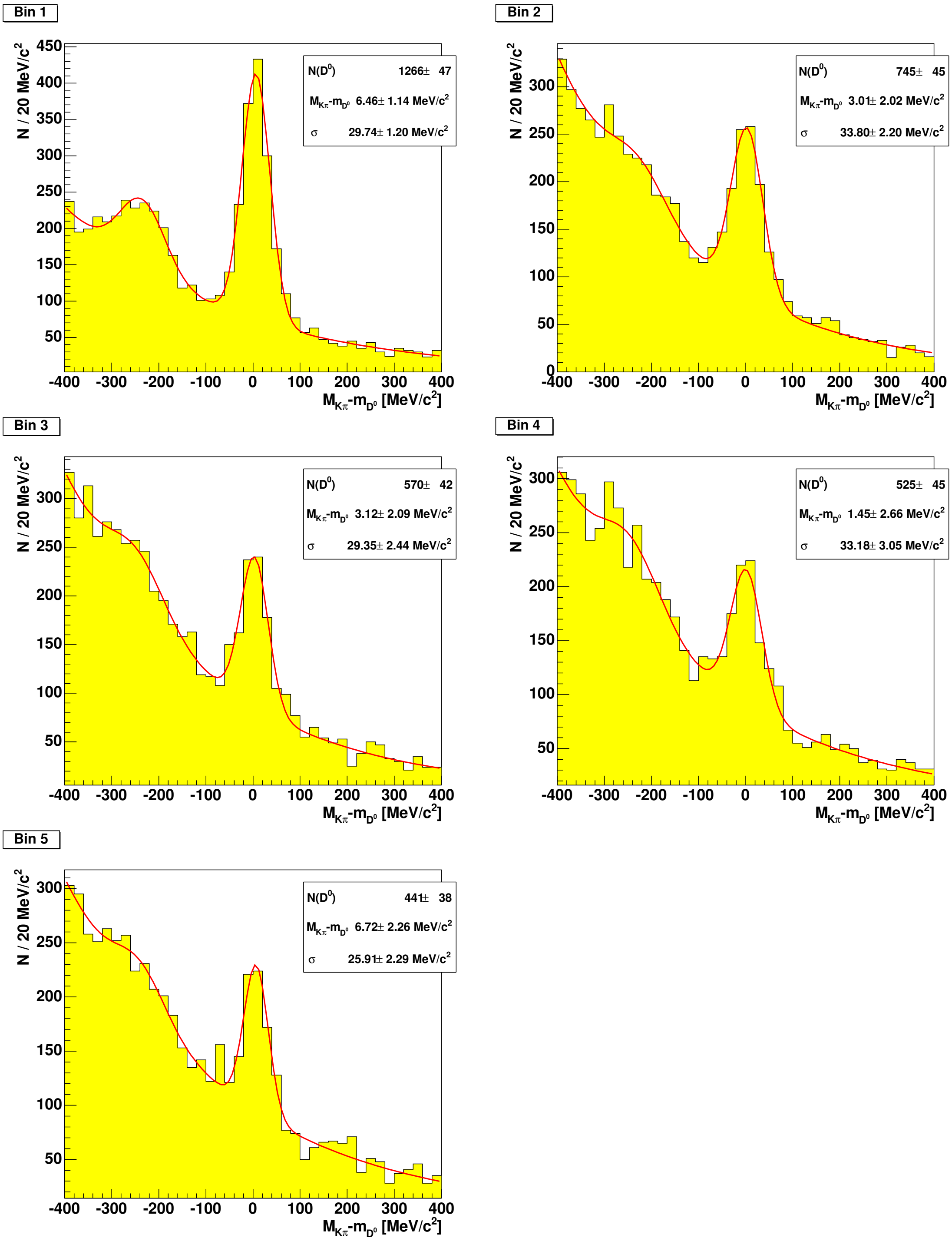

Figure 6.7: The plots show the invariant mass spectra for the $D^\star$ tagged sample in the bins of $fP_\mu a_{\rm LL}$ indicated in Fig. 6.6. A clear decrease of the signal-to-background ratio with increasing bin number is visible.

Table 6.2: Summary of the signal-to-background ratios as a function of bins in $fP_\mu a_{\rm LL}$ for the $D^\star$ tagged and the untagged event sample. The values result from a fit of S/B to the invariant mass spectrum in a mass window of $\pm 1.8\sigma$ and $\pm 1.45\sigma$ around the nominal D^0 mass in the $D^\star$ tagged case and the untagged one, respectively.

	$D^\star$ tagged D^0	untagged D^0
Bin 1	2.876 ± 0.160	0.112 ± 0.008
Bin 2	1.486 ± 0.118	0.071 ± 0.006
Bin 3	1.128 ± 0.107	0.070 ± 0.006
Bin 4	0.959 ± 0.102	
Bin 5	0.809 ± 0.081	

between the dilution factor, the beam polarisation and the signal-over-background ratio is weak, therefore this parametrisation is effectively a function of the analysing power, which in turn most strongly depends on p_t. The distributions of p_t and z_D in the first and the last bin of $fP_\mu a_{\rm LL}$ are shown in Fig. 6.8 and support the statement made before. The parametrisation is primarily a function of p_t.

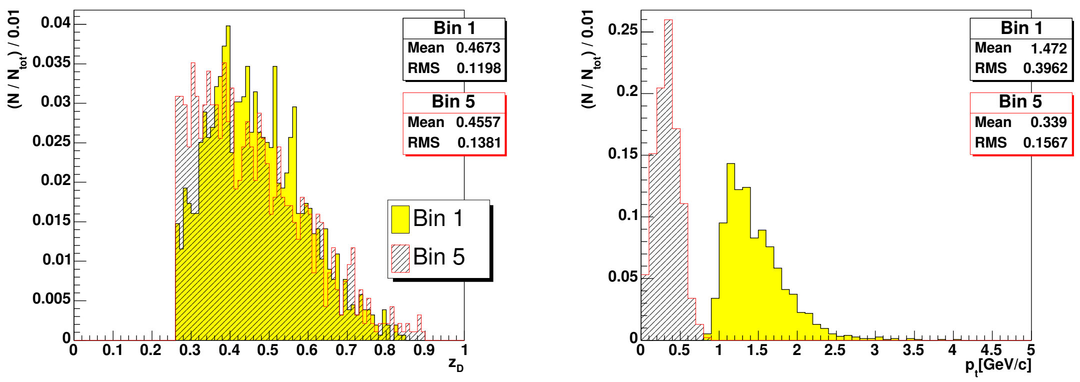

Figure 6.8: The plots show the distributions of z_D and p_t for those events in the first and the last bin of $fP_\mu a_{\rm LL}$, respectively. A clear shift is visible in the case of p_t indicating that the parametrisation is primarily a function of p_t.

In order to make sure that the dependence of the signal-to-background ratio on p_t is not an artefact of the spectrometer and the reconstruction, the distribution of p_t was studied in a Monte Carlo simulation at generator level. For the generation of background events the Pythia generator [105] was used and only events in the mass range of $\pm 400\,\mathrm{MeV}/c^2$ around the nominal D^0 mass were accepted. The resulting distribution for p_t is plotted in Fig. 6.9 and compared to the corresponding signal distribution obtained using AROMA. They show that the shift between the distributions for signal and for background events is present already at generator level and is therefore based on a physics effect and not on an artefact of acceptance and reconstruction. The background events mainly originate from leading order photon-quark scattering. As discussed in Sec. 2.5.1 the struck quark then emerges typically in the direction of the incident virtual photon and thus has small p_t.

This means that the $S/(S+B)$ parametrisation really describes basic physics and not the symptoms of low reconstruction efficiency in some parts of the phase space. The parametrisation is thus used in the extraction of the gluon polarisation, which will be presented in the next chapter.

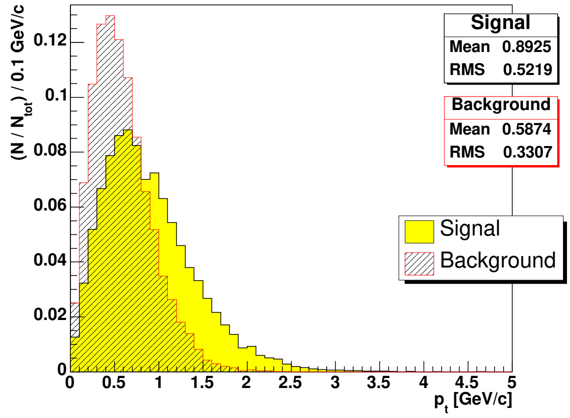

Figure 6.9: The distribution of p_t is studied at generator level. The background distribution is obtained from Pythia, whereas the signal events are as usual generated by AROMA. The shift between the distributions shows that the dependence of the signal-to-background ratio is due to a physics effect and not due to an artefact introduced by the spectrometer or the reconstruction.

Chapter 7

Results for $\Delta G/G$ and their Interpretation

7.1 Results for $\Delta G/G$

For the extraction of the gluon polarisation the so-called Second Order Method was used (cf. Sec. 6.1.2). The reason for this choice is that this method does not need the assumption of equal acceptances of the two target cells in contrast to the First Order Method (cf. Sec. 6.1.1). Since in this analysis the ratio of the acceptance of the downstream cell over the one in the upstream cell can be of the order of 1.5 to 2, this is a relevant aspect. For the extraction of the result it was assumed that the background is unpolarised. It will be discussed in Sec. 7.2.1 to what extent this assumption is justified and how large the systematic uncertainty due to this assumption is.

All events inside a $\pm 400\,\mathrm{MeV}/c^2$ mass window around the nominal D^0 mass were used for computing the asymmetries and, referring to Eq. (6.24), the following relations were used in order to directly determine $\Delta G/G$:

$$\beta = P_\mu P_t f a_{\mathrm{LL}} \frac{S}{S+B} \tag{7.1}$$

$$w = P_\mu f a_{\mathrm{LL}} \frac{S}{S+B}. \tag{7.2}$$

The factor $S/(S+B)$ is evaluated from the parametrisation discussed in Sec. 6.3.4 according to the invariant mass of the D^0 candidate and the value of $f P_\mu a_{\mathrm{LL}}$ of the event in question. Furthermore, the analysing power used for the extraction was computed using a mass of the charm quark of $m_c = 1500\,\mathrm{MeV}/c^2$, as this seems to be the value favoured most by the data (cf. Sec. 6.3.3).

The results for the two sub-samples, namely the $D^\star$ tagged D^0s and the untagged ones, are shown for the different years of data taking in Fig. 7.1. The numerical values are summarised in Tab. 7.1.

The combined result of the three years of data taking from 2002 to 2004 is

$$\frac{\Delta G}{G} = -0.31 \pm 0.44(\mathrm{stat.}). \tag{7.3}$$

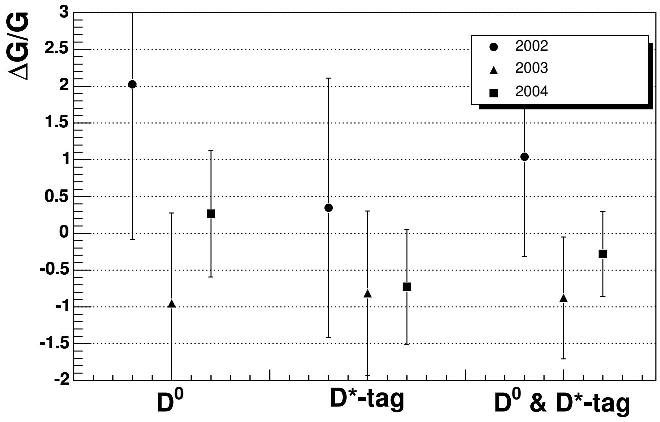

Figure 7.1: Result for $\Delta G/G$ for the $D^\star$ tagged D^0s and the untagged ones. Shown are the values obtained for the three years of data taking 2002 to 2004.

The corresponding average nucleon momentum fraction carried by the gluon is $\eta = 0.15$. A direct reconstruction of this quantity is not possible, since only one charmed meson is reconstructed, therefore the value was extracted from a Monte Carlo simulation along with the true analysing power (cf. Sec. 6.3.3). Two thirds of the η distributions are contained in the interval $[0.10, 0.22]$. This is taken to be the range in which the gluon polarisation is extracted.

The next section is devoted to the discussion of systematic effects inherent in the procedure of extraction of the gluon polarisation or introduced by the various ingredients of the analysis. The final result of this work will be presented at the end of that section.

Table 7.1: Summary of the results for the gluon polarisation shown in Fig. 7.1.

	$\Delta G/G$ (no tagging)	$\Delta G/G$ ($D^\star$ tagging)	Mean
2002	2.03 ± 2.11	0.34 ± 1.76	1.04 ± 1.35
2003	-0.95 ± 1.23	-0.82 ± 1.12	-0.88 ± 0.83
2004	0.27 ± 0.86	-0.73 ± 0.78	-0.28 ± 0.58

7.2 Systematic Effects

7.2.1 Polarisation of the Background

The result for $\Delta G/G$ presented in the last section was extracted assuming an unpolarised background, which means that the background asymmetry A^{Bg} vanishes. This section is devoted to the question, whether this assumption is justified. There are several different approaches to estimate the asymmetry of the background. Three of them will be discussed in the following:

- Extraction of asymmetries from the side bands of the invariant mass distribution
- Extraction of asymmetries from wrongly charged background
- Use of the so-called Fit Method for the asymmetry extraction.

Exploiting the Side Bands

This approach is based on the assumption that the signal contribution is negligible in the side bands of the invariant mass spectrum. In case of the D^0 this assumption is justified as long as the safety margin to the signal region is chosen to be large enough. For this purpose the intervals $|M - m_{D^0}|/(\mathrm{MeV}/c^2) \in [150, 400]$ was chosen, leaving a $\sim 5\sigma$ distance to the nominal mass of the D^0 .

In the case of the $D^\star$ tagged D^0s , however, the assumption is not justified due to the reflection of the decay $D^0 \to K\pi\pi^0$, which is clearly seen in the spectra of Fig. 5.10. Therefore only the side bands of the untagged D^0 sample are used in this approach, since there the influence of the reflection is strongly diluted. The background asymmetry is not expected to differ significantly between the two samples. The result from the untagged D^0s can thus be generalised.

The raw asymmetries $A^{\mathrm{Bg}}_{\mathrm{raw}}$ are extracted from the side bands using the Second Order Method with

$$|\beta| = \frac{B}{S+B} \tag{7.4}$$

$$w = \frac{B}{S+B}. \tag{7.5}$$

The results for the raw asymmetries, which are largely consistent with zero are summarised in Tab. 7.2.

Table 7.2: Summary of the results for the raw background asymmetry $A^{\mathrm{Bg}}_{\mathrm{raw}}$ extracted from the side bands of the untagged D^0 invariant mass spectrum. For this purpose a mass range $|M - m_{D^0}|/(\mathrm{MeV}/c^2) \in [150, 400]$ was chosen.

	$A^{\mathrm{Bg}}_{\mathrm{raw}}$
2002	-0.0031 ± 0.0030
2003	-0.0038 ± 0.0018
2004	0.0001 ± 0.0013
Mean	-0.0016 ± 0.0009

Wrongly charged Background

The contamination by signal events can be neglected in the case of wrongly charged background. For this approach D^0 candidates are reconstructed using kaon and pion candidates with the same charge. For the $D^\star$ tagging the correctly charged soft pion is used. Apart from these choices of the charges all other cuts are equal to the nominal reconstruction. The charge combinations used for the nominal reconstruction and for this approach of the wrongly charged background are collected in Tab. 7.3.

Table 7.3: Summary of the charge combinations used for the nominal D^0 reconstruction and for the wrongly charged background.

	nominal	wrongly charged background
$D^0\,(K,\pi)$	$(-,+)$ or $(+,-)$	$(-,-)$ or $(+,+)$
$D^\star\,(K,\pi,\pi_S)$	$(-,+,+)$ or $(+,-,-)$	$(-,-,+)$ or $(+,+,-)$

The resulting mass spectra of this reconstruction are shown in Fig. 7.2. The raw asymmetries are again extracted using the Second Order Method, where now $|\beta| = 1$ and $w = 1$ are used. Since a signal contribution to the spectra can be neglected there is no need to avoid the signal region. Thus the mass range $|M - m_{D^0}|/(\mathrm{MeV}/c^2) \in [0, 400]$ is used for the extraction. The results for the raw asymmetries $A_{\mathrm{raw}}^{\mathrm{Bg}}$ are summarised in Tab. 7.4. All values turn out to be consistent with zero.

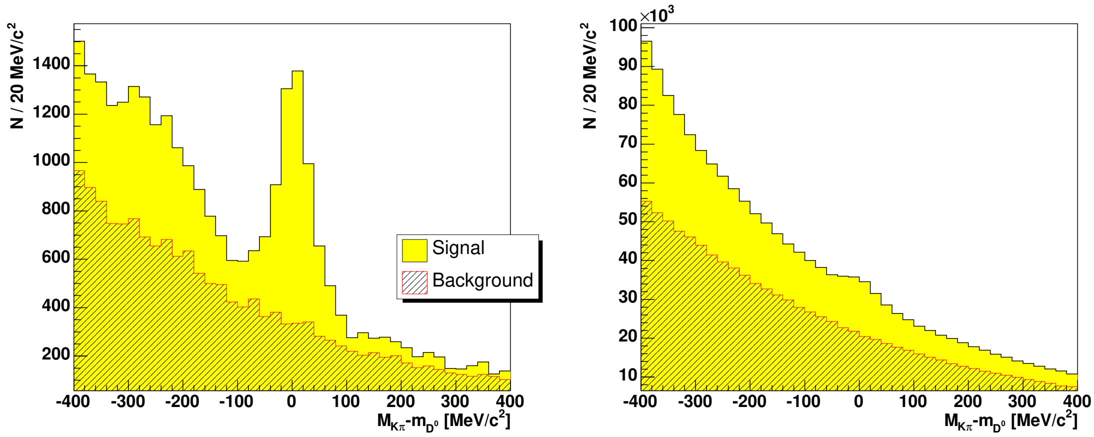

Figure 7.2: The invariant mass spectrum of the wrongly charged background compared to the nominal reconstruction. The left plot shows the $D^\star$ tagged spectrum, whereas the D^0s reconstructed without the tagging enter the spectrum on the right. Both spectra contain the three years of data taking 2002–2004.

Table 7.4: Summary of the results for the raw background asymmetry $A^{\mathrm{Bg}}_{\mathrm{raw}}$ extracted from wrongly charged background. The mass range used for the extraction is $|M - m_{D^0}|/(\mathrm{MeV}/c^2) \in [0, 400]$.

	$A^{\mathrm{Bg}}_{\mathrm{raw}}$ (untagged D^0)	$A^{\mathrm{Bg}}_{\mathrm{raw}}$ ($D^\star$ tagging)
2002	-0.0001 ± 0.0032	0.006 ± 0.023
2003	-0.0015 ± 0.0018	-0.006 ± 0.014
2004	-0.0005 ± 0.0013	0.011 ± 0.011
Mean 2002 to 2004	-0.0007 ± 0.0010	

Fit Method

In order to exploit the Fit Method for the extraction of the background asymmetry the following was used (cf. Eq. (6.29) and (6.30)):

$$|\hat{\beta}| = 1 \tag{7.6}$$

$$w_S = \frac{S}{S+B} \quad \text{and} \quad w_B = \frac{B}{S+B}. \tag{7.7}$$

Due to the reflection of the D^0 decay via an undetected neutral pion only the untagged D^0 sample is used in this approach. The results for the raw asymmetry $A^{\mathrm{Bg}}_{\mathrm{raw}}$ obtained with the Fit Method are summarised in Tab. 7.5 and are compared in Fig. 7.3 to the results previously presented.

As was discussed in Sec. 6.1.3 the Fit Method is not only able to extract the asymmetry of the background but can simultaneously determine the charmed asymmetry $A^{c\bar{c}}$. The

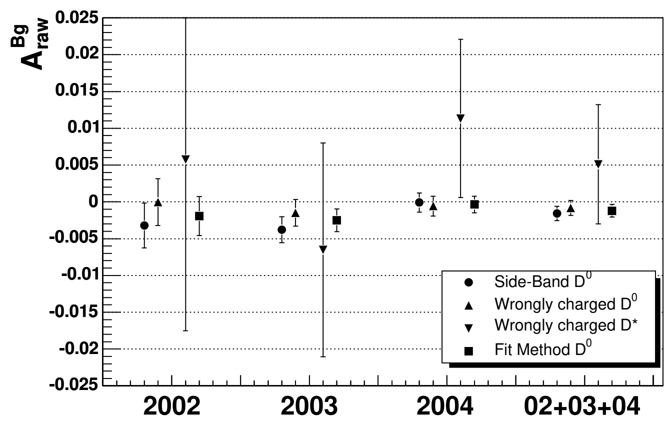

Figure 7.3: Results for $A^{\mathrm{Bg}}_{\mathrm{raw}}$ extracted by applying different methods. Compared are the values obtained from the side bands of the untagged D^0 invariant mass spectrum, the ones from the wrongly charged background and the results extracted by the Fit Method. The results are consistent with each other and mostly also consistent with zero.

Table 7.5: Summary of the results for the raw background asymmetry $A_{\rm raw}^{\rm Bg}$ extracted with the Fit Method. The mass range used for the extraction is $|M - m_{D^0}|/(\mathrm{MeV}/c^2) \in [0, 400]$.

	$A_{\rm raw}^{\rm Bg}$ (untagged D^0)
2002	-0.00192 ± 0.00266
2003	-0.00251 ± 0.00155
2004	-0.00036 ± 0.00114
Mean 2002 to 2004	-0.00120 ± 0.00087

results are compared to values for $A_{\rm raw}^{c\bar{c}}$ computed with the Second Order Method with

$$|\beta| = \frac{S}{S+B} \tag{7.8}$$

$$w = \frac{S}{S+B}. \tag{7.9}$$

The values obtained are summarised in Tab. 7.6 and plotted in Fig. 7.4. No significant deviations are observed between the result from the Second Order Method, which neglects the contribution from $A^{\rm Bg}$ and the Fit Method. This result justifies the use of the Second Order Method with its assumptions for the extraction of the gluon polarisation in Sec. 7.1.

Table 7.6: Summary of the results for the raw asymmetry $A_{\rm raw}^{c\bar{c}}$ extracted with the Fit Method and the Second Order Method. The values give the weighted average of untagged and $D^\star$ tagged D^0s.

	Fit Method	Second Order Method
2002	0.001 ± 0.051	-0.001 ± 0.051
2003	-0.019 ± 0.030	-0.015 ± 0.031
2004	-0.027 ± 0.023	-0.023 ± 0.023
Mean 2002-2004	-0.021 ± 0.017	-0.018 ± 0.018

Conclusion on the Asymmetry of the Background

The information about the background asymmetry collected with the different approaches is consistent. In order to arrive at a final result for the background asymmetry the results obtained from the side bands of the D^0 and the values from the wrongly charged background are combined. Due to the strong correlation between the side band approach and the result from the Fit Method the latter is to be interpreted as a cross check. The result for the raw background asymmetry is given by

$$A_{\rm raw}^{\rm Bg} = -0.00115 \pm 0.00071. \tag{7.10}$$

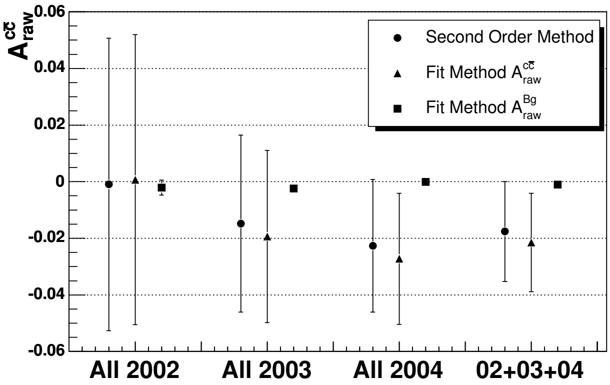

Figure 7.4: Summary of the results for the asymmetry $A^{c\bar{c}}_{\mathrm{raw}}$ extracted with the Fit Method. The values are compared to those, which were extracted with the Second Order Method. The values show the weighted average of untagged and $D^\star$ tagged D^0s. In addition the values for $A^{\mathrm{Bg}}_{\mathrm{raw}}$ obtained from the Fit Method are shown for the untagged D^0 sample.

In order to estimate the systematic effect of neglecting this asymmetry in the extraction of the gluon polarisation the result for $A^{\mathrm{Bg}}_{\mathrm{raw}}$ is compared to $A^{c\bar{c}}_{\mathrm{raw}}$. This yields a value of 7 % for the relative systematic error due to the influence of a possibly polarised background.

7.2.2 Analysing Power

The systematic influence of the analysing power on the result for the gluon polarisation is two-fold. The inevitable deviation of the parametrisation of a_{LL} from the true value is to be taken into account as well as the dependence of the analysing power on the mass of the charm quark whose value is uncertain.

Influence of the Parametrisation

The parametrisation $a^{\mathrm{par}}_{\mathrm{LL}}(y, p_t, z_D)$ (cf. Sec. 6.3.3) is performing well considering the fact that only part of the charmed final state is detected. However, with a correlation of about 78 % it is not perfect and thus could possibly distort the result for $\Delta G/G$. In order to quantify the effect a toy Monte Carlo was used, which simulates the spin dependent effects.

In this approach unpolarised events were generated and reconstructed just like for the extraction of the parametrisation $a^{\mathrm{par}}_{\mathrm{LL}}$ (cf. Sec. 6.3.3). Each event was then randomly assigned to one of the solenoid-field configurations ("inner" or "outer") according to a flat distribution. Depending on the z coordinate of the corresponding primary vertex the events were associated to one of the target cells. The spin-dependent part of the interaction was simulated by weighting each event with

$$w_{\mathrm{pol}} = 1 - \hat{\beta} a^{\mathrm{true}}_{\mathrm{LL}} \frac{\Delta G}{G}, \tag{7.11}$$

where the true analysing power was used, which is computed with the complete information about the parton kinematics. The gluon polarisation was chosen to be -0.3 corresponding to the central value of the final result quoted in Sec. 7.1. The absolute values of the diluting factors entering $\hat{\beta}$ namely f, P_μ and P_t were set to one in order to increase the statistical significance of the analysis. The resulting event sample was then analysed with the Second Order Method, once using the true value for the analysing power and once using the value from the parametrisation. For the analysis an unweighted approach was chosen (weight $w = 1$ in Eq. (6.24)), which means that the two analyses are 100 % correlated and the interpretation is easier. The results of the analysis are summarised in Tab. 7.7. Both results are consistent with the input of $\Delta G/G$. Comparing the realistic result obtained with the parametrised $a_{\rm LL}$ to the one obtained with the true analysing power one can deduce a deviation of 0.5 %. This effect is small compared to other systematic effects in the analysis and will thus be neglected.

Table 7.7: Summary of the results for $\Delta G/G$ obtained from a toy Monte Carlo. An event sample was generated assuming the true analysing power and $\Delta G/G = -0.3$. The sample was then analysed once using the true value of the analysing power and once with the value from the parametrisation.

	input $\Delta G/G$	with $a_{\rm LL}^{\rm true}$	with $a_{\rm LL}^{\rm par}$
$\Delta G/G$	-0.3	-0.291 ± 0.016	-0.289 ± 0.016

Influence of the Mass of the Charm Quark

As discussed in Sec. 6.3.3 the favoured value for the mass of the charm quark is $m_c = 1500\,\mathrm{MeV}/c^2$, which is also the value used for the extraction of the result presented in Sec. 7.1. However, it was also pointed out that variations of m_c of $\pm 100\,\mathrm{MeV}/c^2$ are not excluded. In order to estimate the uncertainty on the result for the gluon polarisation due to this possibly different charm quark mass, the analysis is repeated using the two extreme values $m_c = 1400\,\mathrm{MeV}/c^2$ and $m_c = 1600\,\mathrm{MeV}/c^2$. In the default analysis using the Second Order Method the analysing power enters in the weight of each event. Changing the weight between two analyses means that the event sample is effectively changed, which makes the interpretation of the results more difficult. This is the reason why the unweighted approach ($w = 1$) was applied here. For the extraction of the results events were taken from a mass window of $\pm 1.8\sigma$ in the case of the $D^\star$ tagged D^0s and $\pm 1.45\sigma$ for the untagged sample. This was done to make the results also applicable in Sec. 7.2.4.

The parametrisations of the analysing power for the different masses of the charm quarks were produced as described in Sec. 6.3.3. The results for $\Delta G/G$ for the different mass values are summarised in Tab. 7.8. These values indicate a variation of the result for the gluon polarisation of ± 11 %.

7.2.3 False Asymmetries

All methods for the asymmetry extraction introduced in Chapter 6 rely on the assumption that the experimental setup is stable in time (cf. Eq. (6.14)). Only under this condition do the acceptance differences between the two target cells cancel exactly. Even though great

Table 7.8: Summary of the results for $\Delta G/G$ extracted using different values for the mass of the charm quark m_c. For the analysis the unweighted Second Order Method was applied on an event sample taken only from the signal region around m_{D^0}.

	$m_c = 1400\,\mathrm{MeV}/c^2$	$m_c = 1500\,\mathrm{MeV}/c^2$	$m_c = 1600\,\mathrm{MeV}/c^2$
$\Delta G/G$	-0.43 ± 0.67	-0.39 ± 0.60	-0.35 ± 0.55

efforts are made to avoid changes in the experimental setup and to keep the setup stable, the assumption mentioned above is not always perfectly fulfilled. This means that instead of the pure physical asymmetry a result is extracted, which can be distorted by a false asymmetry.

The influence of false asymmetries has been studied extensively also by other analysis groups inside COMPASS in the course of extracting results for A_1 or for $\Delta G/G$ via the high-p_t approach. Both of these analyses have a considerably larger statistical significance than the open charm approach studied in this thesis. In these analyses the influence of false asymmetries was found to be small compared to the statistical error [26, 97]. Considering these results and the current statistical accuracy of the open-charm analysis, it is not expected that the influence of false asymmetries plays an important rôle here.

There are, however, two differences between the mentioned analyses and this work which may be relevant. First, due to small event yields this analysis is forced to use the global configuration for the grouping of the data (cf. Sec. 6.2) and secondly, the approach presented in this thesis is heavily relying on the RICH detector, which is not used in the other analyses. In order to confirm that these differences do not introduce important effects, a few investigations have been performed.

One way to estimate false asymmetries is to extract asymmetries in a situation, where physical asymmetries are absent. This can be done by artificially dividing each target cell into two halves, which are then treated as upstream and downstream cell (cf. Fig. 7.5). A separate measurement of the false asymmetry can then be obtained from each of the two physical target cells.

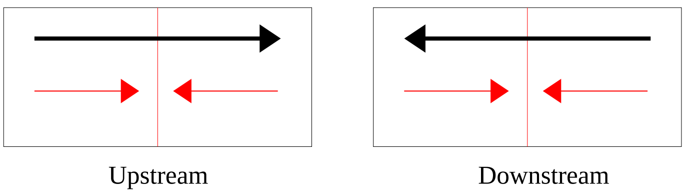

Figure 7.5: The principle of the extraction of asymmetries, which do not have a physical origin. Each of the target cells is artificially divided into two halves, which are then treated as separate cells for the purpose of computing asymmetries. The data are analysed as if the spins were oriented as indicated by the short arrows.

In order to increase the statistical significance of the determination of the false asymmetry, it is desirable to use not only the signal part of the invariant mass spectrum but also the background region. Provided that the corresponding events are detected in similar regions of the spectrometer, there is no reason to assume different false asymmetries for signal and background. As an indication, which region of the spectrometer is used for the detection of a given track, the polar angle $\theta_{\rm lab}$ in the laboratory frame is used. The distributions of this angle for the decay products of the $D^\star$ candidates are shown in Fig. 7.6. The comparison between the distribution for the side-band subtracted signal and the one for the background shows that one can safely assume that the two categories of events are reconstructed in the same regions of the spectrometer. This means that the invariant mass spectrum in the range of $\pm 400\,\mathrm{MeV}/c^2$ around the nominal D^0 mass can be used for the extraction of the false asymmetry, in order to enhance the statistical significance.

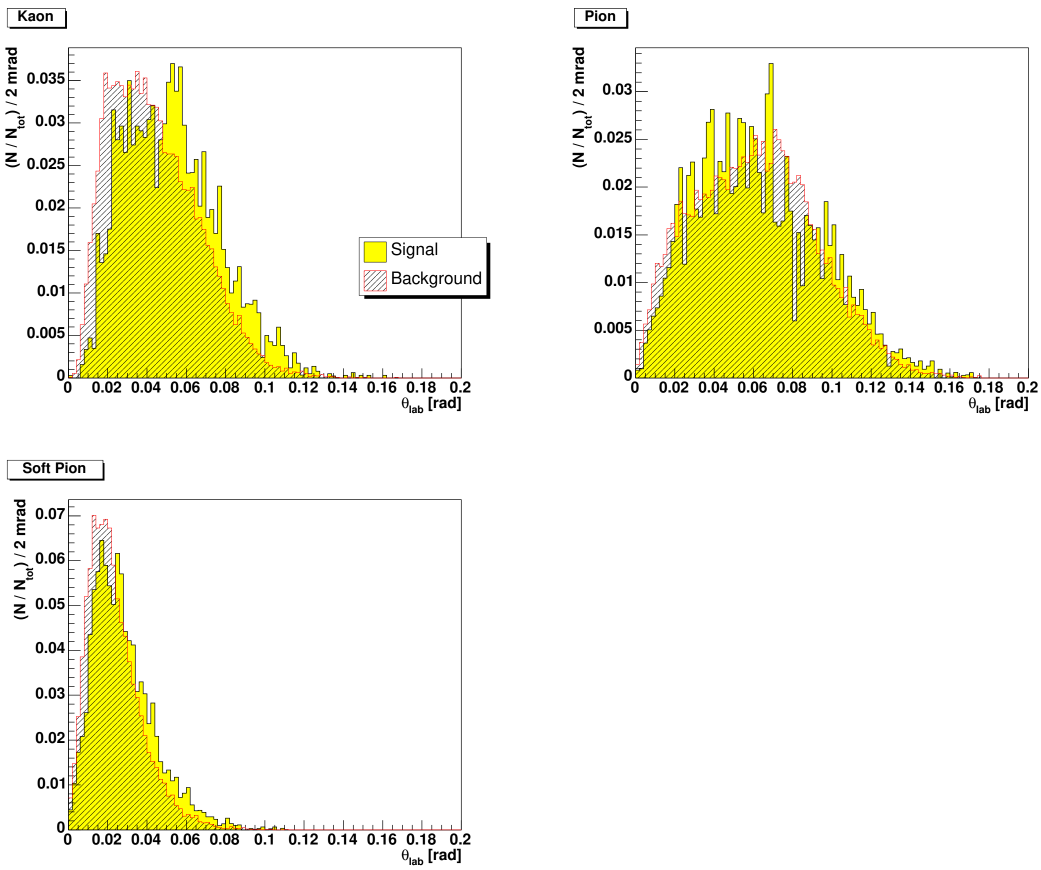

Figure 7.6: The plots show the polar angle $\theta_{\rm lab}$ in the laboratory frame for the decay products of the $D^\star$. The distributions for signal events obtained by side-band subtraction are compared to the one extracted from the background region of the invariant mass spectrum. The agreement between the signal and background distributions justify the use of the spectrum in the range of $\pm 400\,\mathrm{MeV}/c^2$ around m_{D^0} for the extraction of the false asymmetries.

The analysis proceeds by using the Second Order Method with $w = 1$ and $|\beta| = 1$. The results obtained are shown in Fig. 7.7 and summarised in Tab. 7.9. Computing the mean over the three years and the two target cells, where the statistical error of the signal

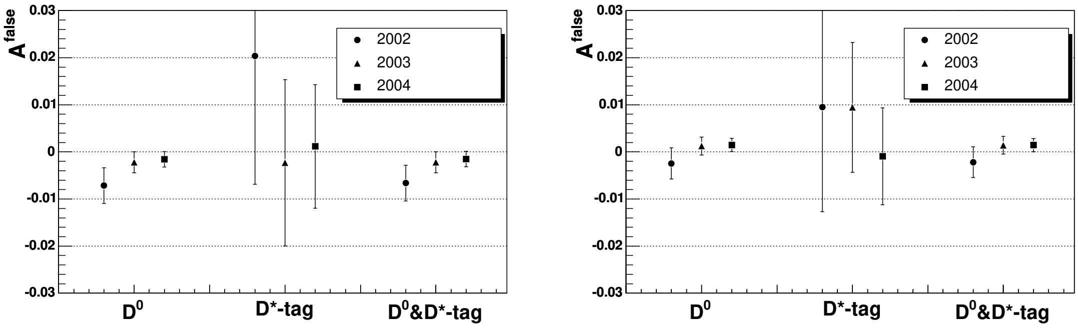

Figure 7.7: The false asymmetry A_{false} extracted by sub-dividing the upstream target cell (left) and the downstream target cell (right). The plots show A_{false} for the $D^\star$ tagged event sample as well as for the untagged D^0s for the years 2002–2004.

Table 7.9: Summary of the results for A_{false} extracted by subdividing a single target cell. The values give the weighted means over the $D^\star$ tagged sample and the untagged D^0s for the corresponding years.

Year	A_{false} upstream	A_{false} downstream
2002	-0.0066 ± 0.0038	-0.0022 ± 0.0033
2003	-0.0022 ± 0.0022	0.0014 ± 0.0018
2004	-0.0015 ± 0.0016	0.0014 ± 0.0014

asymmetry $A^{c\bar{c}}_{\mathrm{raw}}$ serves as weight, one obtains

$$A_{\mathrm{false}} = -0.00041 \pm 0.00080. \tag{7.12}$$

This result is compatible with zero, however, in order to be safe the error on the false asymmetry is used to estimate the systematic influence. Putting this value in relation to the value for the signal asymmetry $A^{c\bar{c}}_{\mathrm{raw}}$, the estimation for the relative error due to false asymmetries is 8 %.

7.2.4 Signal and Background Parametrisations

The parametrisation of the signal and the background contributions to the invariant mass spectrum as functions of $fP_\mu a_{\mathrm{LL}}$ was discussed in Sec. 6.3.4. It was extracted by integrating over the three years of data taking. Possible differences between the years are ignored by this approach, which was motivated by the wish for a reasonable number of bins in $fP_\mu a_{\mathrm{LL}}$ and reliable fits.

In order to estimate the systematic effect of the integration over the entire data sample, parametrisations were produced for each year separately. In the case of the $D^\star$ tagged sample of 2002 the statistics are too low for a stand-alone fit. As a remedy the shape of the background in the different bins was fixed to the value of the global spectrum. The analysis was then repeated with the new parametrisations. For reasons which were already discussed in the context of the dependence on the charm quark mass (cf. Sec. 7.2.2) the unweighted Second Order Method was chosen and applied on an event sample from a narrow mass window. The result is summarised in Tab. 7.10 and compared to the equivalent analysis with the default parametrisation of signal and background. The relative systematic error estimated from these results amounts to 5 %.

Table 7.10: Summary of the results for $\Delta G/G$ obtained using different signal and background parametrisations. The default is obtained by integrating over the three years of data taking 2002-2004. The alternative approach uses one parametrisation per year.

	default	parametrisation per year
$\Delta G/G$	-0.39 ± 0.60	-0.37 ± 0.59

7.2.5 Other Sources of Systematic Errors

In addition to those sources of systematic effects discussed in dedicated sections above, there are a few more quantities introducing rather small uncertainties. The dilution factor, the beam polarisation and the target polarisation have been covered in Secs. 6.3.2 and 6.3.1, respectively. The relative errors associated to these quantities have been discussed in the corresponding sections and are summarised in Tab. 7.11.

Table 7.11: Summary of the relative errors on the dilution factor, the beam and the target polarisations.

$\delta f/f$	$\delta P_\mu/P_\mu$	$\delta P_t/P_t$
5 %	5 %	5 %

7.2.6 Final Result for $\Delta G/G$

In order to arrive at the final result for $\Delta G/G$ the different contributions to the systematic error need to be combined. For this purpose the assumption has to be made that the various sources of systematic errors are independent. This is in some cases not entirely true. The estimated background asymmetry and the false asymmetry are correlated. Adding their contributions linearly should, however, give an upper limit of the resulting systematic error.

The different contributions to the systematic error are summarised in Tab. 7.12. When adding these contributions according to the discussion above the resulting uncertainty is about 21 %. With this value the final result for the gluon polarisation is

$$\frac{\Delta G}{G} = -0.31 \pm 0.44(\text{stat.}) \pm 0.07(\text{syst.}). \tag{7.13}$$

This value for the gluon polarisation has been measured at a mean momentum fraction carried by the gluon $\langle\eta\rangle = 0.15$ in a range given by $[0.10, 0.22]$.

Table 7.12: Summary of the contributions to the systematic error. The various sources of uncertainties were discussed in the previous sections.

A^{Bg}	m_c	A^{false}	$S/(S+B)$	f	P_μ	P_t
7 %	11 %	8 %	5 %	5 %	5 %	5 %

7.3 Interpretation

This section is dedicated to the discussion of the result for the gluon polarisation obtained in this analysis via the open charm approach. The value will be compared to previous measurements of $\Delta G/G$ from various experiments and to the expectations based on results from QCD fits (cf. Sec. 2.4).

In order to compare the result of this work directly to the polarised gluon density $\Delta G(\eta)$ from QCD fits, a parametrisation of the unpolarised density $G(\eta)$ is needed. For this purpose the GRV98 parametrisation [106] is averaged over the kinematic range of the open charm result for $\Delta G/G$. In the case of open charm production the hard scale of the process, which allows for the perturbative treatment, is given by the mass of the charm quark and the transverse momentum p_t of the D^0: $\mu^2 = 4(m_c^2 + p_t^2)$. This means that the gluon distribution is probed at the scale $\mu^2 \approx 13\,(\text{GeV}/c)^2$. The momentum fraction carried by the gluon is plotted in Fig. 7.8 together with $G(\eta, \mu^2 = 13\,(\text{GeV}/c)^2)$.

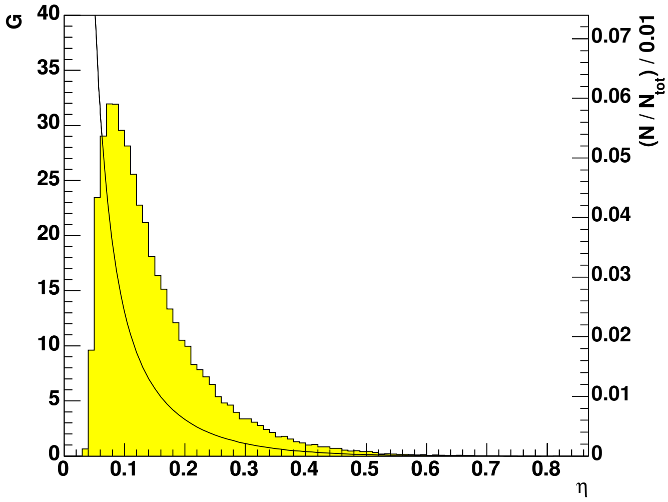

Figure 7.8: The plot shows the unpolarised gluon density $G(\eta)$ given by the parametrisation GRV98, which has been obtained from a QCD fit to the world data of the spin independent structure function $F_2(x, Q^2)$. The parametrisation is shown at a scale of $\mu^2 = 13\,(\mathrm{GeV}/c)^2$. In addition the distribution of the momentum fraction carried by the gluons is shown, as extracted from a Monte Carlo simulation. This spectrum is expected to reflect the distribution of η in the measurement presented in this thesis.

As pointed out in Sec. 7.1 the momentum fraction η cannot be directly extracted from the data. This means that the quantity has to be obtained from a Monte Carlo simulation, which is done in the same way as for the true analysing power $a_{\mathrm{LL}}^{\mathrm{true}}$ (cf. Sec. 6.3.3).

The weighted average of the unpolarised gluon density in η amounts to $\int_0^1 w(\eta)G(\eta)d\eta = 12.4$, which is taken to be without error. The weight entering the average is given by the distribution of η shown in Fig. 7.8. Using this value for the gluon distribution one arrives at a result for $\eta\Delta G$ for this analysis of

$$\eta\Delta G = -0.58 \pm 0.82(\mathrm{stat.}). \tag{7.14}$$

This value is plotted in Fig. 7.9 and compared to various parametrisations of ΔG obtained from QCD fits. The final result of this work is compatible with all the parametrisations shown in the plot.

In Fig. 7.10 the value obtained for the gluon polarisation is compared to previous measurements of this quantity. Different experiments have already extracted $\Delta G/G$ by tagging the photon-gluon fusion process via the detection of hadron pairs with large transverse momentum p_t (cf. Sec. 2.5.1). The various analyses can be categorised by the Q^2 range in which the corresponding data have been taken. This is of importance since resolved photon contributions are expected to be negligible at large Q^2 ($Q^2 > 1\,(\mathrm{GeV}/c)^2$) but could give sizeable contributions at low Q^2.

The HERMES experiment at DESY has extracted $\Delta G/G$ mainly in the low Q^2 range ($\langle Q^2\rangle = 0.06\,(\mathrm{GeV}/c)^2$) [107] and arrives at a value of $\Delta G/G = 0.41 \pm 0.18 \pm 0.03$ at $\langle\eta\rangle = 0.17$, neglecting possible contributions due to resolved photons. The result obtained

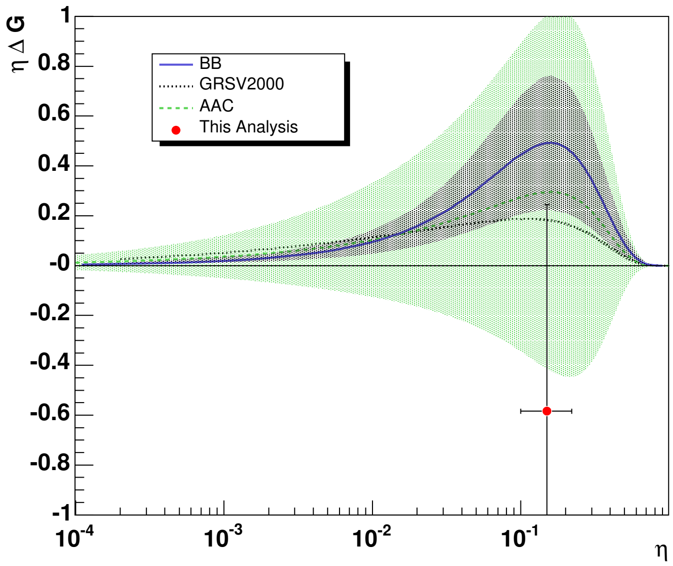

Figure 7.9: The plot shows the value for $\eta\Delta G$ as obtained in this analysis through the open charm approach. It is compared to different parametrisations for $\Delta G(\eta, \mu^2 = 13\,(\mathrm{GeV}/c)^2)$ obtained by QCD fits to the spin dependent structure function $g_1(x, Q^2)$. Shown are analyses by Blümlein/Böttcher (BB, [44]), Glück et al. (GRSV, [45]) and the Asymmetry Analysis Collaboration (AAC, [46]). The shaded areas give the uncertainties of the BB parametrisation (dark) and the AAC parametrisation, respectively.

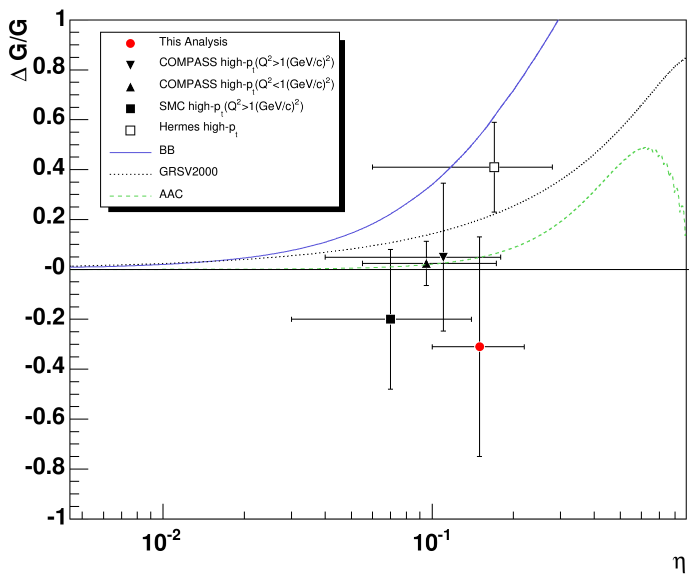

Figure 7.10: The result for the gluon polarisation as obtained in this work is compared to different previous measurements. In addition the parametrisations of $\Delta G/G$ from QCD fits are shown, computed from the parametrisations shown in Fig. 7.9 and the unpolarised density from GRV98.

by SMC was extracted for $Q^2 > 1\,(\mathrm{GeV}/c)^2$ and gives a value for the gluon polarisation of $\Delta G/G = -0.20 \pm 0.28 \pm 0.10$ at $\langle\eta\rangle = 0.07$ [108].

As discussed in Sec. 2.5.1 also the COMPASS collaboration has obtained results for the gluon polarisation, extracted via the high-p_t approach from the data collected in 2002 and 2003. The analysis for $Q^2 < 1\,(\mathrm{GeV}/c)^2$ takes into account resolved photon contributions and arrives at $\Delta G/G = 0.024 \pm 0.089 \pm 0.057$ at $\langle\eta\rangle = 0.095$. The corresponding analysis for the $Q^2 > 1\,(\mathrm{GeV}/c)^2$ range has obtained $\Delta G/G = 0.049 \pm 0.296 \pm 0.105$ at $\langle\eta\rangle = 0.11$.

In addition to the directly measured values for the gluon polarisation Fig. 7.10 also shows results from QCD fits for comparison. The parametrisations of $\Delta G(\eta)$ shown in Fig. 7.9 have been used to compute the gluon polarisation together with the parametrisation of GRV98 for the unpolarised density. The comparison in general shows that the direct measurements of the gluon polarisation are compatible with the parametrisations from QCD fits. The first moments of the parametrisations are around or below one and the overall agreement with the direct measurement leads to the impression that the contribution of the gluons to the nucleon spin is small. Taking the measured points at face value they are also compatible with a node at $\eta \approx 0.1$, which, however, would result in an even smaller value for the first moment of the distribution.

In Sec. 2.3.2 it was discussed that in the AB factorisation scheme the unexpected smallness of the measured value for a_0 could be explained by the reduction due to the anomalous gluon contribution. In this scheme the quark contribution to the nucleon spin is given by

$$\Delta\Sigma^{\mathrm{AB}} = a_0(Q^2) + \frac{n_f \alpha_s(Q^2)}{2\pi}\Delta G(Q^2). \tag{7.15}$$

In order to be consistent with the expectation for the quark contribution of about 0.75 [3] a value for ΔG of the order of 2.5 to 3 would be needed. This seems to be unlikely in the light of the results presented in Fig. 7.10 and leads to the conclusion that the smallness of the quark contribution to the nucleon spin cannot be explained by the contribution of the gluons in the AB scheme.

The challenge for future experiments is now to determine the contribution of the orbital angular momenta of the quarks and gluons to the nucleon spin and to find out whether these can account for the missing pieces in the nucleon spin structure.

Chapter 8

Summary

The complicated structure of the nucleon has been studied with great success in deep-inelastic lepton-nucleon scattering (DIS) experiments at CERN, SLAC and DESY. As a result the unpolarised structure functions have been measured accurately over a wide kinematic range. From these measurements it is possible to determine the gluon density in the nucleon with good accuracy via a so-called QCD fit.

In the case of the spin structure of the nucleon the situation is different. Even after decades of experimental and theoretical efforts it remains to be understood how the spin of the nucleon of $\hbar/2$ is to be accounted for in terms of contributions from the quarks and gluons inside the nucleon. Of particular interest is the question whether the polarised gluon density can explain the unexpected smallness of the quark contribution to the nucleon spin.

The QCD fit, which worked well in the unpolarised case, yields a polarised gluon density $\Delta G(\eta)$ which is only badly constrained. This is due to the fact that the information on the polarised structure functions is only available in a rather small kinematic range, since the corresponding measurements are so far exclusively performed by fixed-target experiments. The limited knowledge of the structure functions aggravates the difficulty that the gluon distribution enters only in next-to-leading order and is thus suppressed by α_s. A direct measurement of ΔG is therefore needed to get a clearer picture.

This direct measurement is the major aim of the COMPASS experiment at CERN. The process on which this measurement is based is the photon-gluon fusion (PGF). It can result in the production of a $c\bar{c}$ pair and is then tagged by detecting the charmed mesons in the final state. This approach results in a theoretically very clean sample of PGF events, assuming that the intrinsic charm content in the nucleon is negligible.

Since the charm tagging of the PGF process is very much statistically limited, it profits directly from improvements of the reconstruction efficiency. A major contribution was made in the course of this work concerning the reconstruction of the momentum of the beam muons. The efficiency of this reconstruction was initially limited by the fact that information from the contributing detectors, installed about 100 m apart along the beam line, could only be associated by using the time stamp of the corresponding measurements. The main improvement is that now also space information is taken into account, based on the knowledge of the transfer matrix of the beam line. In total the fraction of non-reconstructable events could be decreased from 19 % to 6 %.

The polarised target used in the COMPASS experiment is a large solid-state target which does not allow the use of dedicated vertex detectors. The identification of the charmed mesons thus has to proceed via the reconstruction of their invariant mass. In order to control the combinatorial background, the reconstruction relies heavily on the RICH detector. This work contributed to the understanding of how this detector and the spectrometer in general can be used best in order to extract the cleanest possible signal of charmed mesons. Especially the tagging of $D^\star$ decays results in a very clear signal and thus makes COMPASS the first polarised fixed-target experiment which is able to extract the gluon polarisation via the open charm approach.

The analysing power needed for the extraction is given by the ratio of spin dependent and spin averaged muon-nucleon cross sections, which have been calculated to first order in α_s. These cross sections cannot be computed exactly in the analysis, since they depend on parton kinematics, which are poorly known due to the fact that typically only one of the two charmed mesons produced in the PGF process is detected. Thus a parametrisation based on Monte Carlo simulations was prepared, which maps the parton kinematics onto measurable quantities. This makes the analysing power available on an event-by-event basis with sufficient accuracy and thus allows a statistically optimal analysis.

The final result for the gluon polarisation is extracted at a mean momentum fraction carried by the gluon of $\eta = 0.15$ and at a scale $\mu^2 \simeq 13\,(\mathrm{GeV}/c)^2$ and was found to be

$$\frac{\Delta G}{G} = -0.31 \pm 0.44(\mathrm{stat.}) \pm 0.07(\mathrm{syst.}). \tag{8.1}$$

The systematic error is mostly due to the uncertainty on the mass of the charm quark, possible false asymmetries and the background contribution to the asymmetry.

This result for $\Delta G/G$ is consistent with parametrisations obtained from QCD fits to polarised DIS data. Together with other direct measurements of the gluon polarisation by the SMC, HERMES and COMPASS experiments, where hadron pairs with high transverse momentum are used to tag the PGF, a consistent picture starts to form. The measurements favour a polarised gluon distribution whose integral is considerably smaller than the value needed in the AB factorisation scheme to explain the smallness of the quark spin contribution.

The significance of the result will be enhanced by more data to be taken by COMPASS in the future, especially in view of the new target magnet with increased acceptance and upgraded photon detectors for the RICH. But also the prospect of studying the orbital angular momentum contribution of the quarks via deeply virtual Compton scattering gives COMPASS the possibility to further contribute to our understanding of the spin structure of the nucleon.

Appendix A

Details of the Beam Reconstruction

As discussed in Sec. 4.3.2 the knowledge of the beam optics of the transfer line between the BMS setup and the position of the FI/SI telescope is used to sort out ambiguities in the reconstruction. The values of the elements of the transfer matrix used in Eq. (4.1) are summarised in Tab. A.1 [91].

Table A.1: Summary of the elements of the beam-line transfer matrix, used in the back-propagation procedure. The values are given for the position of the corresponding BMS stations.

	M_{33}	M_{34}	M_{36}
BMS 1	0.561	-43.498	13.596
BMS 2	-0.032	-21.484	6.376
BMS 3	-0.894	16.304	0.610
BMS 4	-1.288	37.401	1.076

Appendix B

Details of the D Meson Reconstruction

B.1 χ^2 Correction Method

The χ^2 of a given mass hypothesis can be written as follows

$$\chi_i^2 = \frac{1}{N_{\mathrm{DOF}}} \sum_{k=1}^{N^\gamma} \frac{\left(\theta_k^\gamma - \theta_i\right)^2}{\left(\sigma_\theta^\gamma\right)^2} \qquad i \in \{\pi, K, p\}, \tag{B.1}$$

where the sum runs over all photons N^γ in the signal, θ_k^γ is the angle of the k-th photon in the ring, θ_i is the expected Čerenkov angle for a given mass hypothesis i and σ_θ^γ is the resolution in θ. Since the mDSTs do not contain information about individual photons, the goal is to absorb the dependence on θ_k^γ into factors, which can then be determined from the available information. Eq. (B.1) can be written as follows

$$\chi_i^2 = a - 2 \cdot b \cdot \theta_i + c \cdot (\theta_i)^2, \tag{B.2}$$

with

$$a = \frac{1}{N_{\mathrm{DOF}}} \sum_{k=1}^{N^\gamma} \frac{\left(\theta_k^\gamma\right)^2}{\left(\sigma_\theta^\gamma\right)^2}, \qquad b = \frac{1}{N_{\mathrm{DOF}}} \sum_{k=1}^{N^\gamma} \frac{\theta_k^\gamma}{\left(\sigma_\theta^\gamma\right)^2}, \qquad c = \frac{1}{N_{\mathrm{DOF}}} \sum_{k=1}^{N^\gamma} \frac{1}{\left(\sigma_\theta^\gamma\right)^2}. \tag{B.3}$$

Thus one obtains a set of equations

$$\begin{aligned} \chi_\pi^2 &= a - 2 \cdot b \cdot \theta_\pi^{\mathrm{prod}} + c \cdot (\theta_\pi^{\mathrm{prod}})^2 \\ \chi_K^2 &= a - 2 \cdot b \cdot \theta_K^{\mathrm{prod}} + c \cdot (\theta_K^{\mathrm{prod}})^2 \\ \chi_{\mathrm{ring}}^2 &= a - 2 \cdot b \cdot \theta_{\mathrm{ring}}^{\mathrm{prod}} + c \cdot (\theta_{\mathrm{ring}}^{\mathrm{prod}})^2, \end{aligned} \tag{B.4}$$

where χ_i^2 are the values taken from the mDST information and $\theta_\pi^{\mathrm{prod}}$ and θ_K^{prod} are computed using the production value of the refractive index. The χ_{ring}^2 is the χ^2 of a ring fit without mass hypothesis and $\theta_{\mathrm{ring}}^{\mathrm{prod}}$ the Čerenkov angle resulting from this fit. In principle χ_p^2 could be used as the third equation, however, this choice would imply that the correction could only be applied to particles with a momentum above the RICH proton threshold. The set of equations can be solved for the parameters a, b and c, which are then functions of χ_i^2 and θ_i^{prod}, with $i \in \{\pi, K, \mathrm{ring}\}$.

Finally, the corrected χ^2s can be obtained using the expectations for the angles θ_i^{true} computed with the true refractive index

$$\begin{aligned}
\chi^2_{\pi,\mathrm{true}} &= a - 2\cdot b\cdot \theta_\pi^{\mathrm{true}} + c\cdot (\theta_\pi^{\mathrm{true}})^2 \\
\chi^2_{K,\mathrm{true}} &= a - 2\cdot b\cdot \theta_K^{\mathrm{true}} + c\cdot (\theta_K^{\mathrm{true}})^2 \\
\chi^2_{p,\mathrm{true}} &= a - 2\cdot b\cdot \theta_p^{\mathrm{true}} + c\cdot (\theta_p^{\mathrm{true}})^2.
\end{aligned} \tag{B.5}$$

B.2 Data Sample used for the Analysis

The production of the data is a crucial step in the analysis chain and as the understanding of the spectrometer improves, a reproduction can profit from a revised version of the reconstruction code. This also implies that the result of an analysis can depend on the production version used. For the interpretation of a given result it is therefore interesting to know the exact data sample and production versions used. Both are summarised in Tab. B.1. As was discussed in Section 5.1.2, the refractive index is only known approximately during the first production of the data. For subsequent production iterations the index is then known to the desired accuracy, provided that the data sample is the same. In some cases the run sample considered for production was extended for the reproduction, resulting in a mixture of runs where the index is known accurately and runs for which only the approximation is available. The status of the RICH refractive indices is given in Tab. B.1 for those periods which were used in the analysis presented in this thesis.

In addition to the “bad” spills (cf. Sec. 5.2) the following data were excluded for different reasons:

- The period 02P1C was excluded because of major problems during its production resulting in largely undefined detector calibrations.
- The first runs up to number 27963 of period 03P1A were excluded. Between this set of runs and the following runs lies a period of 2 days without data taking. It is therefore very probable that changes in the experimental setup were made. This could be a source of false asymmetries.

For the periods 02P2E and 02P2F the initial production version 1 is used, since for these periods and also the period 02P1C the reproduction procedure was not yet finished at the time of completion of this analysis*.

*Note that the production procedure does not only consist of the actual data production but also post production work like extraction of the “true” refractive indices and the preparation of lists of unstable spills.

Table B.1: Production versions and RICH index situation for the different periods used in the analysis of this thesis. The following code is used for the status of the RICH refractive indices: (0) means exact, (1) interpolated. Note that in the case of the period 03P1E the production version 1 is more up-to-date than version 3.

	Year 2002							
Period	02P2A	02P2D	02P2E	02P2F	02P2G			
Version	2	2	1	1	2			
RICH	0	0	1	1	0,1			
	Year 2003							
Period	03P1A	03P1B	03P1C	03P1D	03P1E	03P1F	03P1I	03P1J
Version	1	1	1	1	1	1	3	2
RICH	1	1	1	1	0,1	1	0	0
	Year 2004							
Period	04W22	04W23	04W26	04W27	04W28	04W29	04W30	04W31
Version	2	3	2	2	2	1	2	2
RICH	1	0,1	1	1	0,1	1	0,1	1
Period	04W32	04W37	04W38	04W39	04W40			
Version	2	3	2	2	3			
RICH	1	1	1	1	1			

B.3 Optimisation of S_{eff}

The cuts introduced in Secs. 5.4 and 5.5 were chosen such that they yield the maximum effective signal. This section contains the distributions which served as a basis for the decision where to place the cuts. For each of the cuts used in the analysis the effective signal (cf. Eq. (5.8)) is shown as a function of the cut. In addition to that there is a figure with the distribution of the variable on which the cut is to be applied. There is a correlation between the different plots shown. The cuts are applied in the order in which they are shown here. This means that the discussion of a given cut is done on the basis of a data set on which the previously mentioned cuts are already applied. The plots in this section are based on the data taken during 2003.

In the plots, which show the effective signal as a function of a certain cut, the data points are highly correlated. This is because the points contain mostly the same data set. One should keep this in mind when judging the significance of the improvement that a given cut yields. The shaded area around the distributions gives an estimation of the statistical error on the effective signal obtained with the usual $\delta_{\mathrm{N}} = \sqrt{N}$ for the number of events in the signal and in the background, respectively. The estimation ignores correlations between the two contributions.

B.3.1 $D^\star$ Tagging

Cut on ΔM

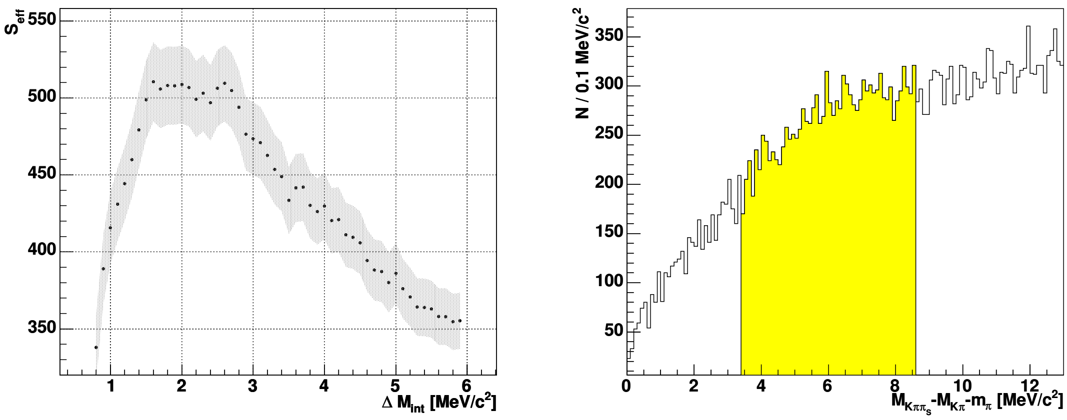

Figure B.1: The plot on the left shows the effective signal as a function of a cut on $\Delta M - m_\pi$, the mass difference between the reconstructed mass of the $D^\star$ and the D^0 reduced by the nominal pion mass. The cut is applied symmetrically around $6\,\mathrm{MeV}/c^2$: $\Delta M - m_\pi \in [6\,\mathrm{MeV}/c^2 - \Delta M_{\mathrm{int}}, 6\,\mathrm{MeV}/c^2 + \Delta M_{\mathrm{int}}]$. The size of the interval used in the analysis was chosen to be $\Delta M_{\mathrm{int}} = 2.6\,\mathrm{MeV}/c^2$. The plot on the right shows the raw distribution of $\Delta M - m_\pi$ as well as the distribution after applying the cut (filled area).

Particle Identification

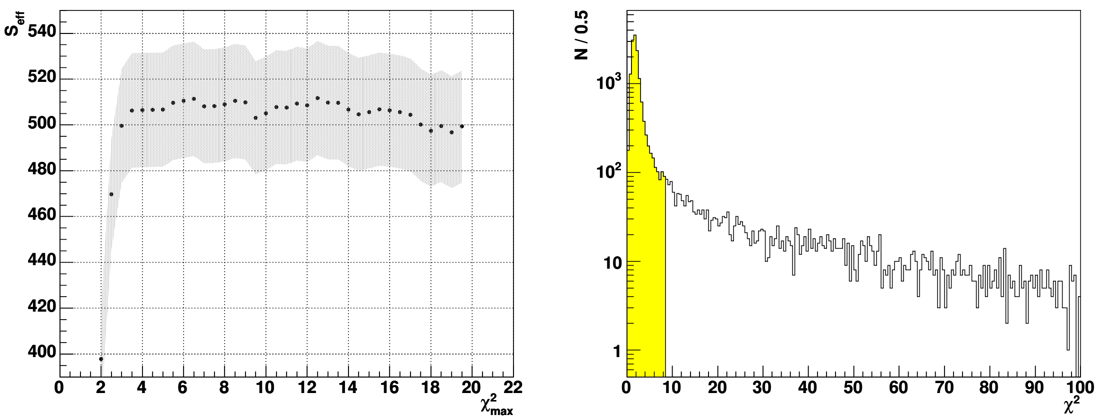

Figure B.2: The plot on the left shows the effective signal as a function of a cut on the χ^2 of the kaon hypothesis. The effective signal plotted is computed for the sample $\chi^2(K) < \chi^2_{\mathrm{max}}$. In the analysis $\chi^2(K) < 8.5$ is used. The distribution of the χ^2 of the kaon hypothesis is plotted on the left before and after (filled region) applying the cut.

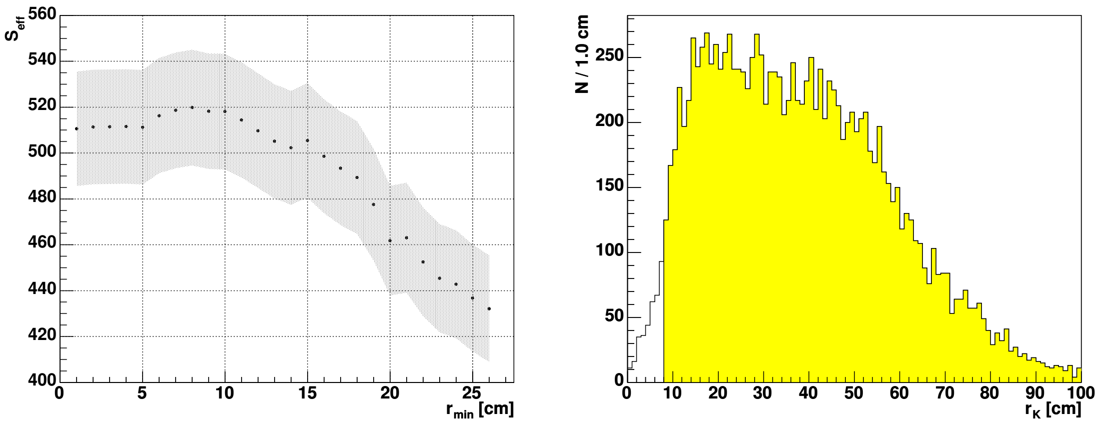

Figure B.3: The plot on the left shows the effective signal as a function of a cut on the position of the impact point of the kaon candidate on the RICH. For the radius of this point $r_K > r_{\mathrm{min}}$ is required. The cut for the analysis was chosen to be $r_K > 8\,\mathrm{cm}$. The raw distribution of the radius as well as its distribution after the cut (filled histogram) is shown in the right plot.

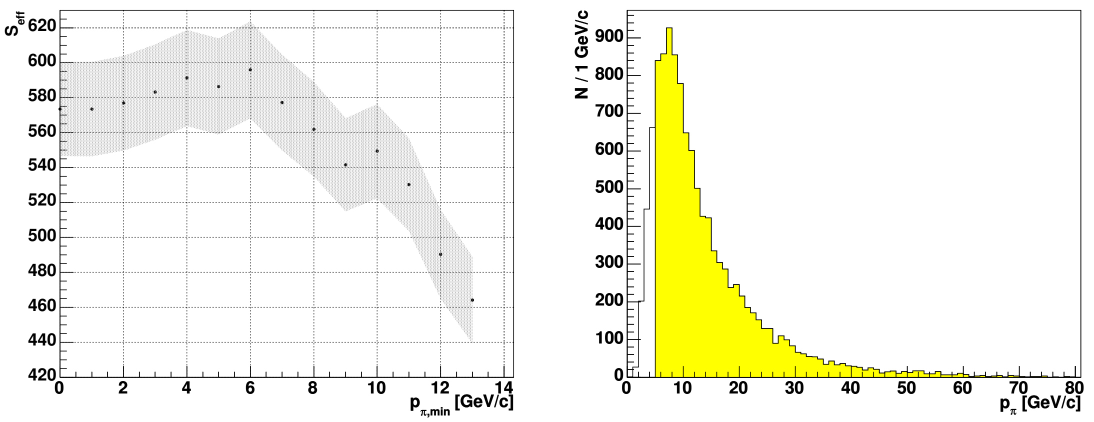

Figure B.4: The plot on the left shows the effective signal as a function of a cut on the pion momentum p_π. For the extraction of the effective signal the momentum is required to be larger than $p_{\pi,\mathrm{min}}$. The increase in effective signal compared to Fig. B.3 is due to the pion veto (cf. Sec. 5.4.2). For the analysis the momentum cut-off was chosen to be $5\,\mathrm{GeV}/c$. The raw distribution of the momentum and its distribution after the cut (filled area) is shown in the right plot.

Cut on D^0 Kinematics

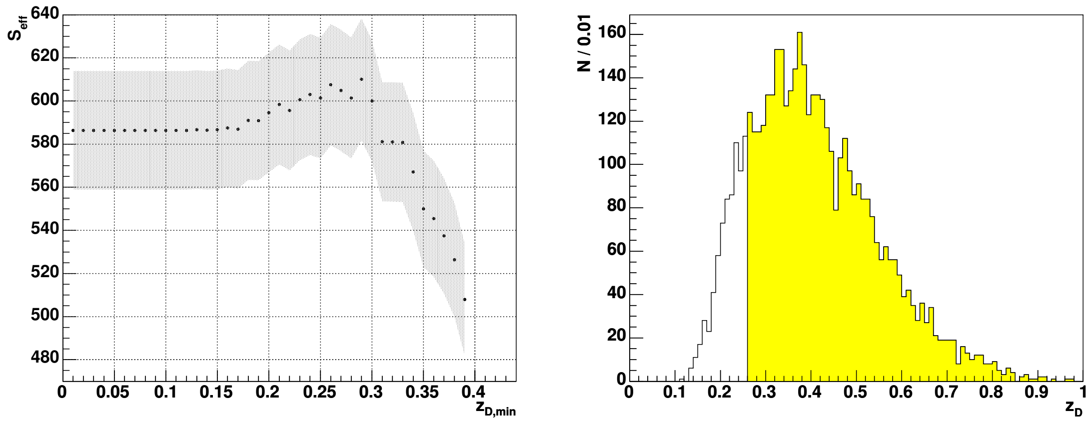

Figure B.5: The effective signal as a function of a cut on the fractional energy z_D of the D^0 is shown on the left side. The value of the effective signal is computed for the data sample with $z_D > z_{D,\mathrm{min}}$. For the analysis a choice of $z_{D,\mathrm{min}} = 0.26$ was made. The right plot contains the distribution of the fractional energy before and after (filled area) the cut.

B.3.2 D^0 Reconstruction

Particle Identification

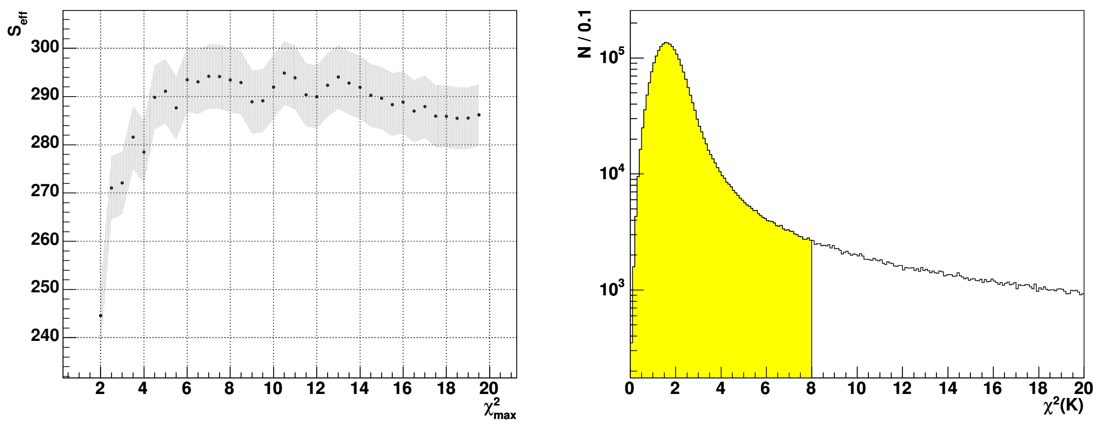

Figure B.6: The plot on the left contains the effective signal as a function of a cut on the χ^2 of the kaon hypothesis. The cut requires $\chi^2(K) < \chi^2_{\mathrm{max}}$. For the analysis a cut of $\chi^2(K) < 8$ is applied. The plot on the right shows the raw distribution of the χ^2 and in addition the distribution after applying the cut (filled area).

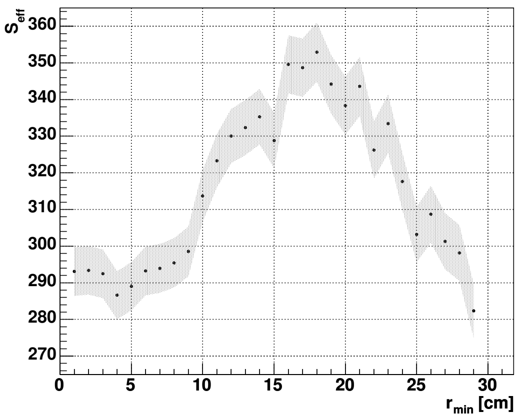

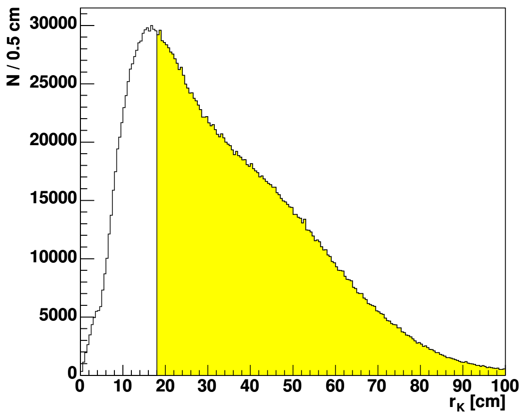

Figure B.7: The effective signal as a function of a cut on the position of the impact point of the kaon at the position of the RICH is shown on the left side. The cut is applied as follows: $r_K > r_{\mathrm{min}}$ and for the analysis the choice is $r_{\mathrm{min}} = 18\,\mathrm{cm}$. The distribution of r_K before and after the cut (filled region) is shown in the right plot.

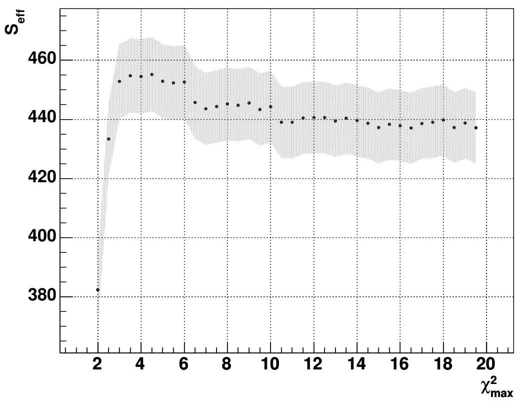

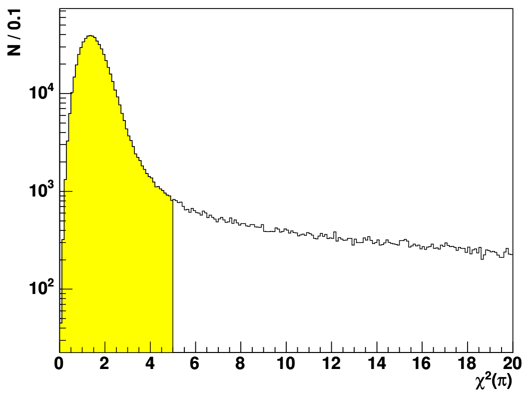

Figure B.8: The left plot shows the effective signal as a function of a cut on the χ^2 of the pion hypothesis. The effective signal is extracted from a data sample for which $\chi^2(\pi) < \chi^2_{\mathrm{max}}$ was required. For the analysis $\chi^2_{\mathrm{max}} = 5$ was chosen to be used. The right plot shows the raw distribution of $\chi^2(\pi)$ and its distribution after the cut (filled region). The increase in effective signal compared to Fig. B.7 is due to the basic requirement that the χ^2 of the pion hypothesis is the smallest χ^2.

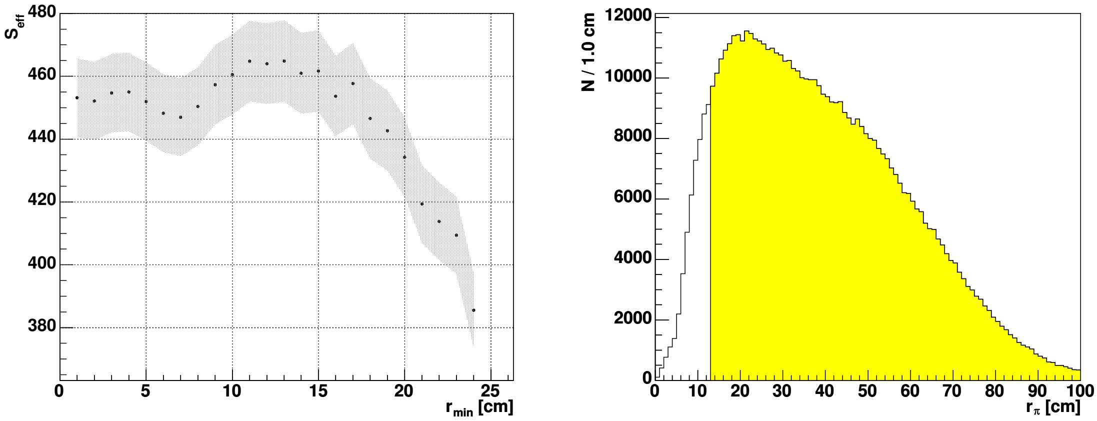

Figure B.9: The effective signal as a function of a cut on the position of the impact point of the pion at the position of the RICH is shown on the left side. The cut is applied as follows: $r_\pi > r_{\min}$. For the analysis the choice is $r_{\min} = 13\,\text{cm}$. The distribution of r_π before and after the cut (filled region) is shown in the right plot.

Cut on D^0 Kinematics

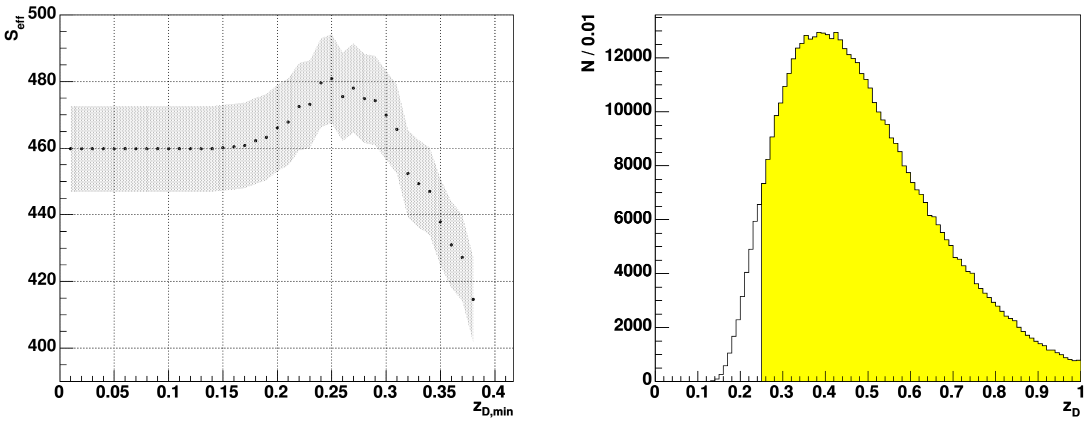

Figure B.10: The plot on the left shows the effective signal as a function of a cut on the fractional energy z_D of the D^0, where the points are extracted from the data sample which satisfies $z_D > z_{D,\min}$. For the analysis $z_{D,\min} = 0.25$ is used. The raw distribution of z_D is shown in the right plot together with its distribution after the cut (filled region).

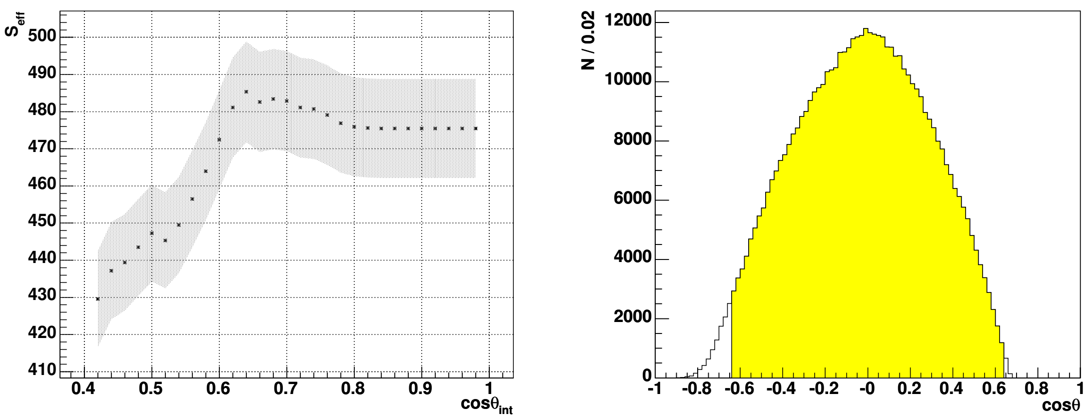

Figure B.11: The left plot shows the effective signal as a function of a cut on $\cos\theta$, where θ is the emission angle of the kaon in the D^0 rest frame relative to the direction of flight of the D^0. The cut is applied symmetrically around zero: $|\cos\theta| < \cos\theta_{\rm int}$. The choice for the analysis is $|\cos\theta| < 0.64$. The plot on the right shows the distribution of $\cos\theta$ before and after the cut (filled region).

B.4 Fit Parameters for the Final Event Sample

This section is devoted to the details of the fits to the invariant mass spectra presented in Fig. 5.10. For the spectra obtained with the $D^\star$-tagging method a fit function is used which describes the signal with a Gaussian and the background with an exponential function added to a Gaussian to account for the $D^0 \to K\pi\pi^0$ reflection (cf. Sec. 5.6). The complete function is given by

$$\begin{aligned} N_{\rm tag}^{D^0}(M') &= \mathrm{Bg}_1 \cdot \exp(\mathrm{Bg}_2 \cdot M') + \frac{\mathrm{N}^{\pi^0}(D^0)}{\sqrt{2\pi}\sigma^{\pi^0}} \exp\left\{ \frac{1}{2} \left(\frac{M' - M_0^{\pi^0}}{\sigma^{\pi^0}} \right)^2 \right\} \\ &\quad + \frac{\mathrm{N}(D^0)}{\sqrt{2\pi}\sigma} \exp\left\{ \frac{1}{2} \left(\frac{M' - M_0}{\sigma} \right)^2 \right\}, \end{aligned} \tag{B.6}$$

where $N_{\rm tag}^{D^0}(M')$ is the number of tagged D^0s at a given invariant mass $M' = M_{K\pi} - m_{D^0}$, Bg_i are the parameters describing the background and $\mathrm{N}^{(\pi^0)}$, $\sigma^{(\pi^0)}$, $M_0^{(\pi^0)}$ are the number of D^0s in the Gaussian peak and the width and position of the Gaussian for the central peak and the reflection (π^0), respectively.

The spectrum of untagged D^0s is fitted with a function given by

$$\begin{aligned} N^{D^0}(M') &= \mathrm{Bg}_1 \cdot \exp(\mathrm{Bg}_2 \cdot M') + \mathrm{Bg}_3 \cdot \exp(\mathrm{Bg}_4 \cdot M') \\ &\quad + \frac{\mathrm{N}(D^0)}{\sqrt{2\pi}\sigma} \exp\left\{ \frac{1}{2} \left(\frac{M' - M_0}{\sigma} \right)^2 \right\}. \end{aligned} \tag{B.7}$$

The fit parameters resulting from the fit of the mentioned functions to the spectra shown in Fig. 5.10 are summarised in Tab. B.2.

Table B.2: Summary of the fit parameters obtained from fitting the functions defined in Eqs. (B.6) and (B.7) to the spectra shown in Fig. 5.10.

	D^0s from $D^\star$ tagging							
	Bg_1 [(20 MeV/c^2)$^{-1}$]	Bg_2 [(10^3MeV/c^2)$^{-1}$]	N^{π^0}	$M_0^{\pi^0}$ [MeV/c^2]	σ^{π^0} [MeV/c^2]	N	M_0 [MeV/c^2]	σ [MeV/c^2]
2002	49.9 ± 2.3	-3.39 ± 0.14	259 ± 118	-242 ± 14	63.5 ± 22.7	482 ± 38	0.92 ± 2.49	35.2 ± 3.3
2003	133 ± 3	-3.11 ± 0.08	718 ± 152	-239 ± 8	58.9 ± 9.6	1112 ± 54	6.0 ± 1.4	29.8 ± 1.6
2004	249 ± 4	-3.07 ± 0.05	994 ± 159	-234 ± 6	52.3 ± 6.4	1928 ± 71	4.6 ± 1.1	29.9 ± 1.2

	Untagged D^0s							
	Bg_1 [(20 MeV/c^2)$^{-1}$]	Bg_2 [(10^2MeV/c^2)$^{-1}$]	Bg_3 [(20 MeV/c^2)$^{-1}$]	Bg_4 [(10^3MeV/c^2)$^{-1}$]	N	M_0 [MeV/c^2]	σ [MeV/c^2]	
2002	0.45 ± 1.02	-1.90 ± 0.05	3297 ± 15	-2.69 ± 0.02	2030 ± 215	0.98 ± 3.21	31.4 ± 3.3	
2003	0.013 ± 0.023	-3.10 ± 0.04	9829 ± 19	-2.70 ± 0.01	4619 ± 328	3.70 ± 1.93	27.6 ± 2.3	
2004	0.013 ± 0.019	-3.24 ± 0.38	18152 ± 26	-2.69 ± 0.01	8464 ± 465	5.38 ± 1.60	29.9 ± 1.7	

The values for the effective signal obtained for the event sample presented in Fig. 5.10 are summarised in Tab. B.3.

Table B.3: Summary of the values for the effective signal obtained for the final event sample presented in Fig. 5.10.

	D^0s from $D^\star$ tagging	untagged D^0s
2002	262 ± 19	177 ± 8
2003	603 ± 28	354 ± 11
2004	1015 ± 36	592 ± 14

Appendix C

Details of the Extraction of $\Delta G/G$

C.1 The Fit Method for Asymmetry Extraction

As discussed in Sec. 6.1.3 a set of eight equations can be obtained. It is given by

$$\sum_k^{N_{u,\mathrm{i}}} w_k^S = I_{u,\mathrm{i}}^S \left(1 - A^{c\bar{c}} \frac{F_{u,\mathrm{i}}^{SS}}{I_{u,\mathrm{i}}^S} - A^{\mathrm{Bg}} \frac{F_{u,\mathrm{i}}^{SB}}{I_{u,\mathrm{i}}^S}\right) =: f_{u,\mathrm{i}}^S(I_{u,\mathrm{i}}^S, A^{c\bar{c}}, A^{\mathrm{Bg}}) \tag{C.1}$$

$$\sum_k^{N_{d,\mathrm{i}}} w_k^S = I_{d,\mathrm{i}}^S \left(1 - A^{c\bar{c}} \frac{F_{d,\mathrm{i}}^{SS}}{I_{d,\mathrm{i}}^S} - A^{\mathrm{Bg}} \frac{F_{d,\mathrm{i}}^{SB}}{I_{d,\mathrm{i}}^S}\right) =: f_{d,\mathrm{i}}^S(I_{d,\mathrm{i}}^S, A^{c\bar{c}}, A^{\mathrm{Bg}}) \tag{C.2}$$

$$\sum_k^{N_{u,\mathrm{o}}} w_k^S = I_{u,\mathrm{o}}^S \left(1 - A^{c\bar{c}} \frac{F_{u,\mathrm{o}}^{SS}}{I_{u,\mathrm{o}}^S} - A^{\mathrm{Bg}} \frac{F_{u,\mathrm{o}}^{SB}}{I_{u,\mathrm{o}}^S}\right) =: f_{u,\mathrm{o}}^S(I_{u,\mathrm{o}}^S, A^{c\bar{c}}, A^{\mathrm{Bg}}) \tag{C.3}$$

$$\sum_k^{N_{d,\mathrm{o}}} w_k^S = I_{d,\mathrm{o}}^S \left(1 - A^{c\bar{c}} \frac{F_{d,\mathrm{o}}^{SS}}{I_{d,\mathrm{o}}^S} - A^{\mathrm{Bg}} \frac{F_{d,\mathrm{o}}^{SB}}{I_{d,\mathrm{o}}^S}\right) =: f_{d,\mathrm{o}}^S(I_{d,\mathrm{o}}^S, A^{c\bar{c}}, A^{\mathrm{Bg}}) \tag{C.4}$$

$$\sum_k^{N_{u,\mathrm{i}}} w_k^B = I_{u,\mathrm{i}}^B \left(1 - A^{c\bar{c}} \frac{F_{u,\mathrm{i}}^{BS}}{I_{u,\mathrm{i}}^B} - A^{\mathrm{Bg}} \frac{F_{u,\mathrm{i}}^{BB}}{I_{u,\mathrm{i}}^B}\right) =: f_{u,\mathrm{i}}^B(I_{u,\mathrm{i}}^B, A^{c\bar{c}}, A^{\mathrm{Bg}}) \tag{C.5}$$

$$\sum_k^{N_{d,\mathrm{i}}} w_k^B = I_{d,\mathrm{i}}^B \left(1 - A^{c\bar{c}} \frac{F_{d,\mathrm{i}}^{BS}}{I_{d,\mathrm{i}}^B} - A^{\mathrm{Bg}} \frac{F_{d,\mathrm{i}}^{BB}}{I_{d,\mathrm{i}}^B}\right) =: f_{d,\mathrm{i}}^B(I_{d,\mathrm{i}}^B, A^{c\bar{c}}, A^{\mathrm{Bg}}) \tag{C.6}$$

$$\sum_k^{N_{u,\mathrm{o}}} w_k^B = I_{u,\mathrm{o}}^B \left(1 - A^{c\bar{c}} \frac{F_{u,\mathrm{o}}^{BS}}{I_{u,\mathrm{o}}^B} - A^{\mathrm{Bg}} \frac{F_{u,\mathrm{o}}^{BB}}{I_{u,\mathrm{o}}^B}\right) =: f_{u,\mathrm{o}}^B(I_{u,\mathrm{o}}^B, A^{c\bar{c}}, A^{\mathrm{Bg}}) \tag{C.7}$$

$$\sum_k^{N_{d,\mathrm{o}}} w_k^B = I_{d,\mathrm{o}}^B \left(1 - A^{c\bar{c}} \frac{F_{d,\mathrm{o}}^{BS}}{I_{d,\mathrm{o}}^B} - A^{\mathrm{Bg}} \frac{F_{d,\mathrm{o}}^{BB}}{I_{d,\mathrm{o}}^B}\right) =: f_{d,\mathrm{o}}^B(I_{d,\mathrm{o}}^B, A^{c\bar{c}}, A^{\mathrm{Bg}}), \tag{C.8}$$

where "i" and "o" denote the two spin configurations. Two parameters can be fixed using $\kappa = 1$ (cf. Eq. (6.14)), here $(I_d^S)^\mathrm{o}$ and $(I_d^B)^\mathrm{o}$ were chosen. The unknown parameters $A^{c\bar{c}}$,

A^{Bg}, $(I_u^S)^{\mathrm{i}}$, $(I_d^S)^{\mathrm{i}}$, $(I_u^S)^{\mathrm{o}}$, $(I_u^B)^{\mathrm{i}}$, $(I_d^B)^{\mathrm{i}}$, $(I_u^B)^{\mathrm{o}}$ can be extracted by minimising the χ^2 given by

$$\chi^2 = (\vec{N} - \vec{f})^T \mathrm{cov}^{-1} (\vec{N} - \vec{f}), \tag{C.9}$$

with

$$\vec{N} = \left(\sum_k^{N_{u,\mathrm{i}}} w_k^S, \sum_k^{N_{d,\mathrm{i}}} w_k^S, \sum_k^{N_{u,\mathrm{o}}} w_k^S, \sum_k^{N_{d,\mathrm{o}}} w_k^S, \sum_k^{N_{u,\mathrm{i}}} w_k^B, \sum_k^{N_{d,\mathrm{i}}} w_k^B, \sum_k^{N_{u,\mathrm{o}}} w_k^B, \sum_k^{N_{d,\mathrm{o}}} w_k^B \right) \tag{C.10}$$

$$\vec{f} = \left(f_{u,\mathrm{i}}^S, f_{d,\mathrm{i}}^S, f_{u,\mathrm{o}}^S, f_{d,\mathrm{o}}^S, f_{u,\mathrm{i}}^B, f_{d,\mathrm{i}}^B, f_{u,\mathrm{o}}^B, f_{d,\mathrm{o}}^B, \right). \tag{C.11}$$

The diagonal elements of the covariance matrix are given by

$$\mathrm{cov}(N_m^{w_n}, N_m^{w_n}) \approx \sum_k^{N_m} (w_{n,k})^2 \tag{C.12}$$

with $m \in \{(u,\mathrm{i}), (d,\mathrm{i}), (u,\mathrm{o}), (d,\mathrm{o})\}$ and $n \in \{S, B\}$. Apart from these diagonal elements there are non-zero off-diagonal elements. This is due to the fact that the same data are used twice, once with a weight w_S and once with w_B (cf. Eqs. (6.29) and (6.37)). These elements are given by [100]

$$\mathrm{cov}(N_m^{w_S}, N_m^{w_B}) = \mathrm{cov}(N_m^{w_B}, N_m^{w_S}) \tag{C.13}$$

$$\approx \sum_k^{N_m} w_{S,k} w_{B,k}, \tag{C.14}$$

where again $m \in \{(u,\mathrm{i}), (d,\mathrm{i}), (u,\mathrm{o}), (d,\mathrm{o})\}$.

C.2 The Analysing Power

The analysing power was defined in Sec. 6.3.3 by

$$a_{\mathrm{LL}} = \frac{\Delta\sigma_{\mu g \to c\bar{c}}}{\sigma_{\mu g \to c\bar{c}}}. \tag{C.15}$$

The spin-averaged and the spin-dependent cross sections are given by

$$\sigma_{\mu g \to c\bar{c}} = \sigma^{(0)}_{\mu g \to c\bar{c}} + \cos\phi \cdot \sigma^{(1)}_{\mu g \to c\bar{c}} + \cos 2\phi \cdot \sigma^{(2)}_{\mu g \to c\bar{c}} \tag{C.16}$$

$$\Delta\sigma_{\mu g \to c\bar{c}} = \Delta\sigma^{(0)}_{\mu g \to c\bar{c}} + \cos\phi \cdot \Delta\sigma^{(1)}_{\mu g \to c\bar{c}}, \tag{C.17}$$

respectively. For the photon-gluon fusion process and the case of heavy quarks (charm or bottom) the contributing terms are given by [103]

$$\sigma^{(0)}_{\mu g \to c\bar{c}} = \frac{\alpha_s}{4\pi} \left\{ \frac{1 + (1-y)^2}{2} \left[\frac{\left[x_p^2 + (1-x_p)^2\right] \left[z_q^2 + (1-z_q)^2\right] + \beta(1-2x_p)}{z_q(1-z_q)} \right. \right.$$

$$+\frac{\beta(2x_p-\beta)}{4z_q^2(1-z_q)^2}\Bigg] + (1-y)\left[8x_p(1-x_p) - \frac{2\beta x_p}{z_q(1-z_q)}\right]\Bigg\} \quad \text{(C.18)}$$

$$\sigma^{(1)}_{\mu g\to c\bar{c}} = \frac{\alpha_s}{2\pi}(y-2)\sqrt{1-y}\sqrt{\frac{x_p(1-x_p)}{z_q(1-z_q)} - \frac{\beta x_p}{4z_q^2(1-z_q)^2)}}(1-2z_q)$$
$$\left(1-2x_p-\frac{\beta}{2z_q(1-z_q)}\right) \quad \text{(C.19)}$$

$$\sigma^{(2)}_{\mu g\to c\bar{c}} = \frac{\alpha_s}{\pi}(1-y)\left[x_p(1-x_p)+\frac{\beta(1-2x_p)}{4z_q(1-z_q)} - \frac{\beta^2}{16z_q^2(1-z_q)^2}\right] \quad \text{(C.20)}$$

$$\Delta\sigma^{(0)}_{\mu g\to c\bar{c}} = \frac{\alpha_s}{4\pi}\frac{1-(1-y)^2}{2}\left[\frac{2x_p-1}{z_q(1-z_q)}+\frac{\beta}{2z_q^2(1-z_q)^2}\right]\left[z_q^2+(1-z_q)^2\right] \quad \text{(C.21)}$$

$$\Delta\sigma^{(1)}_{\mu g\to c\bar{c}} = \frac{\alpha_s}{2\pi}y\sqrt{1-y}\sqrt{\frac{x_p(1-x_p)}{z_q(1-z_q)} - \frac{\beta x_p}{4z_q^2(1-z_q)^2}}(1-2z_q). \quad \text{(C.22)}$$

The form of Eq. (C.22) differs from the one in [103], which contains a misprint [109].

C.3 Parametrisation of the Analysing Power

The parametrisation of the analysing power is obtained from a grid in z_D and p_t in 8×10 bins. The values of the true analysing power in this grid are given for the charm masses of $1400\,\mathrm{MeV}/c^2$, $1500\,\mathrm{MeV}/c^2$ and $1600\,\mathrm{MeV}/c^2$ in Tabs. C.1, C.2 and C.3, respectively.

Table C.1: The true analysing power on a grid of z_D and p_t for $m_c = 1400\,\mathrm{MeV}/c^2$.

	0.025	0.099	0.222	0.396	0.618	0.868	1.226	1.918	3.248	6.231
0.000	0.618	0.609	0.488	0.359	0.247	0.147	-0.050	-0.122	-0.275	-0.523
0.181	0.618	0.609	0.488	0.359	0.247	0.147	-0.050	-0.122	-0.275	-0.523
0.262	0.658	0.559	0.480	0.338	0.241	0.130	0.032	-0.110	-0.278	-0.457
0.353	0.659	0.582	0.482	0.372	0.254	0.144	0.044	-0.100	-0.269	-0.449
0.450	0.690	0.623	0.542	0.428	0.300	0.201	0.090	-0.062	-0.233	-0.417
0.547	0.732	0.675	0.589	0.490	0.363	0.264	0.140	-0.024	-0.203	-0.415
0.645	0.753	0.701	0.639	0.530	0.430	0.339	0.214	0.042	-0.168	-0.405
0.759	0.804	0.751	0.690	0.614	0.507	0.399	0.297	0.115	-0.100	-0.366

Table C.2: The true analysing power on a grid of z_D and p_t for $m_c = 1500\,\mathrm{MeV}/c^2$.

	0.025	0.099	0.222	0.396	0.619	0.869	1.227	1.927	3.240	6.314
0.0	0.666	0.586	0.521	0.384	0.269	0.198	0.082	-0.076	-0.241	-0.446
0.181	0.666	0.586	0.521	0.384	0.269	0.198	0.082	-0.076	-0.241	-0.446
0.262	0.669	0.602	0.506	0.370	0.261	0.178	0.060	-0.075	-0.242	-0.423
0.353	0.689	0.614	0.519	0.395	0.284	0.179	0.076	-0.070	-0.217	-0.405
0.450	0.721	0.647	0.555	0.449	0.331	0.231	0.122	-0.023	-0.203	-0.394
0.548	0.756	0.699	0.599	0.507	0.398	0.296	0.187	0.023	-0.165	-0.386
0.645	0.779	0.744	0.661	0.576	0.475	0.366	0.267	0.078	-0.134	-0.363
0.757	0.818	0.763	0.724	0.606	0.542	0.432	0.347	0.172	-0.066	-0.335

Table C.3: The true analysing power on a grid of z_D and p_t for $m_c = 1600\,\mathrm{MeV}/c^2$.

	0.025	0.099	0.223	0.399	0.617	0.869	1.229	1.925	3.256	6.285
0.000	0.742	0.609	0.537	0.415	0.341	0.226	0.092	-0.080	-0.205	-0.324
0.180	0.742	0.609	0.537	0.415	0.341	0.226	0.092	-0.080	-0.205	-0.324
0.261	0.683	0.627	0.515	0.403	0.286	0.191	0.084	-0.030	-0.202	-0.385
0.353	0.704	0.638	0.537	0.426	0.316	0.212	0.110	-0.018	-0.184	-0.375
0.449	0.725	0.673	0.586	0.467	0.362	0.270	0.164	0.011	-0.155	-0.356
0.547	0.761	0.716	0.635	0.534	0.431	0.339	0.226	0.065	-0.123	-0.336
0.645	0.793	0.749	0.683	0.584	0.501	0.408	0.298	0.126	-0.076	-0.311
0.755	0.829	0.780	0.735	0.662	0.582	0.487	0.384	0.192	0.015	-0.271

C.4 Parametrisation of the Signal to Background Ratio

As discussed in Sec. 6.3.4 the signal and background contributions are parametrised as functions of $fP_\mu a_{\mathrm{LL}}$. For this purpose the invariant mass spectra are needed in bins of $fP_\mu a_{\mathrm{LL}}$. The corresponding bin borders are summarised in Tab. C.4 for the $D^\star$ tagged event sample as well as the untagged one.

Table C.4: The table summarises the bin borders for the binning of the data in $fP_\mu a_{\mathrm{LL}}$ for the purpose of parametrising the signal and background contributions to the invariant mass spectrum as functions of $fP_\mu a_{\mathrm{LL}}$.

	$D^\star$ tagged D^0	untagged D^0
Bin 1	$[-1, 0.03]$	$[-1, 0.06]$
Bin 2	$[0.03, 0.06]$	$[0.06, 0.10]$
Bin 3	$[0.06, 0.09]$	$[0.10, 1]$
Bin 4	$[0.09, 0.12]$	
Bin 5	$[0.12, 1]$	

The values of the parameters entering the parametrisation of the signal and background contributions to the invariant mass spectrum are given in Tab. C.5. They are obtained by fitting the functions defined in Eqs. (B.6) and (B.7) to the spectra shown in Fig. 6.7.

Table C.5: Summary of the fit parameters for the signal and background parametrisations as functions of $fP_\mu a_{\mathrm{LL}}$.

	D^0s from $D^\star$ tagging							
	Bg_1 $[(20\ \mathrm{MeV}/c^2)^{-1}]$	Bg_2 $[(10^3\mathrm{MeV}/c^2)^{-1}]$	N^{π^0}	$M_0^{\pi^0}$ $[\mathrm{MeV}/c^2]$	σ^{π^0} $[\mathrm{MeV}/c^2]$	N	M_0 $[\mathrm{MeV}/c^2]$	σ $[\mathrm{MeV}/c^2]$
Bin 1	74.7 ± 2.2	-2.81 ± 0.10	577 ± 82	-235 ± 5	48.2 ± 5.7	1266 ± 47	6.46 ± 1.14	29.7 ± 1.2
Bin 2	81.7 ± 2.5	-3.51 ± 0.09	340 ± 100	-225 ± 14	60.4 ± 12.6	745 ± 45	3.01 ± 2.02	33.8 ± 2.2
Bin 3	86.4 ± 2.8	-3.33 ± 0.10	386 ± 141	-245 ± 13	59.1 ± 16.3	570 ± 42	3.12 ± 2.09	29.3 ± 2.4
Bin 4	90.0 ± 2.9	-3.08 ± 0.11	432 ± 144	-243 ± 13	61.8 ± 14.1	525 ± 45	1.45 ± 2.66	33.2 ± 3.0
Bin 5	95.6 ± 2.5	-2.93 ± 0.09	272 ± 103	-238 ± 14	53.8 ± 15.9	441 ± 38	6.72 ± 2.26	25.9 ± 2.3
	Untagged D^0s							
	Bg_1 $[(20\ \mathrm{MeV}/c^2)^{-1}]$	Bg_2 $[(10^2\mathrm{MeV}/c^2)^{-1}]$	Bg_3 $[(20\ \mathrm{MeV}/c^2)^{-1}]$	Bg_4 $[(10^3\mathrm{MeV}/c^2)^{-1}]$	N	M_0 $[\mathrm{MeV}/c^2]$	σ $[\mathrm{MeV}/c^2]$	
Bin 1	4.01 ± 3.85	-1.73 ± 0.24	10446 ± 31	-2.55 ± 0.02	6462 ± 348	5.80 ± 1.47	28.1 ± 1.5	
Bin 2	$3.05 \cdot 10^{-2} \pm 4.33 \cdot 10^{-2}$	-2.93 ± 0.36	10186 ± 23	-2.88 ± 0.01	5514 ± 489	1.49 ± 2.93	39.5 ± 4.0	
Bin 3	$1.14 \cdot 10^{-6} \pm 6.91 \cdot 10^{-6}$	-5.31 ± 1.23	10568 ± 20	-2.65 ± 0.01	4087 ± 345	2.13 ± 2.14	27.7 ± 2.8	

List of Figures

List of Tables

Bibliography

[1] G. Baum *et al.*, *COMPASS: A Proposal for a Common Muon and Proton Apparatus for Structure and Spectroscopy*, *CERN-SPSLC-96-14*.

[2] R. L. Jaffe and A. Manohar, *The g_1 Problem: Deep Inelastic Electron Scattering and the Spin of the Proton*, Nucl. Phys. **B337** (1990) 509.

[3] B. W. Filippone and X. Ji, *The Spin Structure of the Nucleon*, Adv. Nucl. Phys. **26** (2001) 1.

[4] A. Airapetian *et al.*, *Quark Helicity Distributions in the Nucleon for Up, Down, and Strange Quarks from Semi-Inclusive Deep-Inelastic Scattering*, Phys. Rev. **D71** (2005) 012003.

[5] M. Frhr. v. Hodenberg, *A First Reconstruction of COMPASS Data*, Diploma Thesis, Freiburg 2002.

[6] S. Eidelman *et al.*, *Review of Particle Physics*, Phys. Lett. **B592** (2004) 1.

[7] S. Chekanov *et al.*, *Measurement of the Neutral Current Cross-Section and F_2 Structure Function for Deep Inelastic e+p Scattering at HERA*, Eur. Phys. J. **C21** (2001) 443.

[8] C. Adloff *et al.*, *Deep-Inelastic Inclusive ep Scattering at Low x and a Determination of α_s*, Eur. Phys. J. **C21** (2001) 33.

[9] L. W. Whitlow *et al.*, *Precise Measurements of the Proton and Deuteron Structure Functions from a Global Analysis of the SLAC Deep Inelastic Electron Scattering Cross-Sections*, Phys. Lett. **B282** (1992) 475.

[10] A. C. Benvenuti *et al.*, *A High Statistics Measurement of the Proton Structure Functions $F_2(x, Q^2)$ and R from Deep Inelastic Muon Scattering at High Q^2*, Phys. Lett. **B223** (1989) 485.

[11] M. R. Adams *et al.*, *Proton and Deuteron Structure Functions in Muon Scattering at 470 GeV*, Phys. Rev. **D54** (1996) 3006.

[12] M. Arneodo *et al.*, *Measurement of the Proton and Deuteron Structure Functions, F_2^p and F_2^d, and of the Ratio σ_L/σ_T*, Nucl. Phys. **B483** (1997) 3.

[13] R. L. Jaffe, *g_2: The Nucleon's Other Spin Dependent Structure Function*, Comments Nucl. Part. Phys. **19** (1990) 239.

[14] B. Adeva *et al.*, *Spin Asymmetries A_1 of the Proton and the Deuteron in the Low x and Low Q^2 Region from Polarized High-Energy Muon Scattering*, Phys. Rev. **D60** (1999) 072004, Erratum-ibid., **D62** (2000) 079902.

[15] G. K. Mallot, *The Spin Structure Of The Nucleon from the SMC Experiment*, Habilitationsschrift, Mainz 1996.

[16] D. Adams *et al.*, *Spin Structure of the Proton from Polarised Inclusive Deep-Inelastic Muon-Proton Scattering*, Phys. Rev. **D56** (1997) 5330.

[17] A. Airapetian *et al.*, *First Measurement of the Tensor Structure Function b_1 of the Deuteron*, Preprint, hep-ex/0506018 (2005).

[18] U. Stösslein, *Measurement of the Spin Structure Function g_1 of the Proton and the Deuteron*, Proc. of 14. Int. Spin Physics Symposium (SPIN 2000), Osaka, (2000).

[19] P. L. Anthony *et al.*, *Deep Inelastic Scattering of Polarized Electrons by Polarized He-3 and the Study of the Neutron Spin Structure*, Phys. Rev. **D54** (1996) 6620.

[20] K. Abe *et al.*, *Measurements of the Proton and Deuteron Spin Structure Functions g_1 and g_2*, Phys. Rev. **D58** (1998) 112003.

[21] K. Abe *et al.*, *Precision Determination of the Neutron Spin Structure Function g_1^n*, Phys. Rev. Lett. **79** (1997) 26.

[22] P. L. Anthony *et al.*, *Measurement of the Deuteron Spin Structure Function $g_1^d(x)$ for $1\,(GeV/c)^2 < Q^2 < 40\,(GeV/c)^2$*, Phys. Lett. **B463** (1999) 339.

[23] A. Airapetian *et al.*, *Measurement of the Proton Spin Structure Function g_1^p with a Pure Hydrogen Target*, Phys. Lett. **B442** (1998) 484.

[24] J. Ashman *et al.*, *An Investigation of the Spin Structure of the Proton in Deep Inelastic Scattering of Polarized Muons on Polarized Protons*, Nucl. Phys. **B328** (1989) 1.

[25] B. Adeva *et al.*, *Spin Asymmetries A_1 and Structure Functions g_1 of the Proton and the Deuteron from Polarized High-Energy Muon Scattering*, Phys. Rev. **D58** (1998) 112001.

[26] E. S. Ageev *et al.*, *Measurement of the Spin Structure of the Deuteron in the DIS Region*, Phys. Lett. **B612** (2005) 154.

[27] J. D. Bjørken and E. A. Paschos, *Inelastic Electron Proton and Gamma Proton Scattering, and the Structure of the Nucleon*, Phys. Rev. **185** (1969) 1975.

[28] J. D. Bjørken, *Asymptotic Sum Rules at Infinite Momentum*, Phys. Rev. **179** (1969) 1547.

[29] C. G. Callan and D. J. Gross, *High-Energy Electroproduction and the Constitution of the Electric Current*, Phys. Rev. Lett. **22** (1969) 156.

[30] A. V. Manohar, *An Introduction to Spin Dependent Deep Inelastic Scattering*, Preprint *UCSD-PTH-92-10*, hep-ph/9204208 (1992).

[31] S. A. Larin, *The Next-To-Leading QCD Approximation to the Ellis-Jaffe Sum Rule*, *Phys. Lett.* **B334** (1994) 192.

[32] J. D. Bjørken, *Applications of the Chiral U(6)×U(6) Algebra of Current Densities*, *Phys. Rev.* **148** (1966) 1467.

[33] M. Anselmino, A. Efremov and E. Leader, *The Theory and Phenomenology of Polarized Deep Inelastic Scattering*, Phys. Rep. **261** (1995) 1.

[34] G. Altarelli, *Partons in Quantum Chromodynamics*, Phys. Rep. **81** (1982) 1.

[35] Y. L. Dokshitzer, *Calculation of Structure Functions of Deep-Inelastic Scattering and e^+e^- Annihilation by Perturbation Theory in Quantum Chromodynamics*, *Sov. Phys. JETP* **46** (1997) 641.

[36] V. N. Gribov, L. N. Lipatov, *Deep Inelastic ep Scattering in Perturbation Theory*, *Sov. J. Nucl. Phys.* **15** (1972) 438.

[37] G. Altarelli and G. Parisi, *Asymptotic Freedom in Parton Language*, Nucl. Phys. **B126** (1977) 298.

[38] R. D. Ball, S. Forte and G. Ridolfi, *NLO Determination of the Singlet Axial Charge and the Polarized Gluon Content of the Nucleon*, Phys. Lett. **B378** (1996) 255.

[39] S. Adler and W. Bardeen, *Absence of Higher Order Corrections in the Anomalous Axial Vector Divergence Equation*, Phys. Rev. **182** (1969) 1517.

[40] J. Kodaira *et al.*, *QCD Effects in Polarized Electroproduction*, Phys. Rev. **D20** (1979) 627.

[41] S. Adler, *Axial Vector Vertex in Spinor Electrodynamics*, Phys. Rev. **177** (1969) 2426.

[42] J. Kodaira *et al.*, *QCD Effects in Polarized Electroproduction*, Phys. Rev. **D20** (1979) 627; J. Kodaira, *QCD Higher Order Effects in Polarized Electroproduction: Flavor Singlet Coefficient Functions*, Nucl. Phys. **B165**, (1980) 129.

[43] R. Mertig, W. L. van Neerven, *The Calculation of the Two Loop Spin Splitting Functions $P_{ij}^{(1)}(x)$*, *Z. Phys.* **C70** (1996) 637; W. Vogelsang, *The Spin Dependent Two Loop Splitting Functions*, Nucl. Phys. **B475**, (1996) 47.

[44] J. Blümlein, H. Böttcher, *QCD Analysis of Polarised Deep Inelastic Scattering Data and Parton Distributions*, Nucl. Phys. **B636** (2002) 225.

[45] M. Glück *et al.*, *Models for the Polarised Parton Distributions of the Nucleon*, *Phys. Rev.* **D63** (2001) 094005.

[46] Y. Goto *et al.*, *Polarized Parton Distribution Functions in the Nucleon*, *Phys. Rev.* **D62** (2000) 034017.

[47] S. Hedicke, *Determination of the Gluon Polarisation from High p_t Hadron Pairs at COMPASS*, Doktorarbeit, Freiburg 2005.

[48] E. S. Ageev *et al.*, *The Gluon Polarization in the Nucleon from Quasi-Real Photoproduction of High p_t Hadron Pairs*, *Preprint*, hep-ex/0511028 (2005).

[49] M. Stratmann, W. Vogelsang, *Photoproduction of Jets and Heavy Flavors at Future Polarized ep-Colliders*, *Z. Phys.* **C74** (1997) 641.

[50] M. Klein, *Structure Functions in Deep Inelastic Lepton-Nucleon Scattering*, *Preprint*, hep-ex/0001059 (2000).

[51] A. D. Watson, *Spin-Spin Asymmetries in Inclusive Muon Proton Charm Production*, *Z. Phys.* **C12** (1982) 123.

[52] G. Bunce, N. Saito, J. Soffer, W. Vogelsang, *Prospects for Spin Physics at RHIC*, *Preprint*, hep-ph/0007218 (2000).

[53] T. Schmidt, *A Common Readout Driver for the COMPASS Experiment*, Doktorarbeit, Freiburg 2002.

[54] A. Grünemaier, *Eine universelle Ausleseschnittstelle für das COMPASS-Experiment*, Doktorarbeit, Freiburg 2002.

[55] R. Webb, *First Measurement of Transverse Spin Asymmetries through Single Pion Production at the COMPASS Experiment*, Doktorarbeit, Erlangen 2004.

[56] O.C. Allkofer *et al.*, *A Large Magnetic Spectrometer System for High-Energy Muon Physics*, *Nucl. Instr. and Meth.* **179** (1981) 445.

[57] B. Adeva *et al.*, *Measurement of the Polarization of a High-Energy Muon Beam*, *Nucl. Instr. and Meth.* **A343** (1994) 363.

[58] D. Adams *et al.*, *Measurement of the SMC Muon Beam Polarization using the Asymmetry in the Elastic Scattering off Polarized Electrons*, *Nucl. Instr. and Meth.* **A443** (2000) 1.

[59] R. Joosten, Universität Bonn, *Private Communication*, December 2003.

[60] G. Abragam, M. Goldman, *Principles of Dynamic Nuclear Polarisation*, *Rep. Prog. Phys.* **41** (1978) 395.

[61] A. Magnon *et al.*, *Tracking with $40 \times 40cm^2$ Micromega Detectors in the High Energy, High Luminosity COMPASS Experiment*, *Nucl. Instr. and Meth.* **A478** (2002) 210.

[62] S. Horikawa *et al.*, *Time Resolution of a Scintillating Fiber Detector*, Nucl. Instr. and Meth. **A431** (1999) 177.

[63] A. Teufel, *Entwicklung und Bau von Hodoskopen aus szintillierenden Fasern für das COMPASS-Experiment*, Doktorarbeit, Erlangen 2003.

[64] M. Wiesmann, *A Silicon Microstrip Detector for COMPASS and A First Measurement of the Transverse Polarization of Λ^0-Hyperons from Quasi-Real Photo-Production*, Doktorarbeit, München 2004.

[65] C. Altunbas *et al.*, *Construction, Test and Commissioning of the Triple-GEM Tracking Detector for COMPASS*, Nucl. Instr. and Meth. **A490** (2002) 177.

[66] Q. Weitzel, Talk given at COMPASS Collaboration Meeting, March 2004.

[67] H. Pereira da Costa, *Développement de chambres à dérive pour les hauts flux dans l'expérience COMPASS*, PhD. Thesis, Paris 2001.

[68] S. Panebianco, Talk given at COMPASS Collaboration Meeting, October 2003.

[69] C. J. Ilgner, *Fertigung und Inbetriebnahme einer Strohdriftkammerstation*, Doktorarbeit, München 2003.

[70] A. Zvyagin, Talk given at COMPASS Collaboration Meeting, December 2003.

[71] M. Leberig, Talk given at COMPASS Collaboration Meeting, October 2003.

[72] E. Albrecht *et al.*, *COMPASS RICH-1*, Nucl. Instr. and Meth. **A502** (2003) 112.

[73] E. Albrecht *et al.*, *The Mirror System of COMPASS RICH-1*, Nucl. Instr. and Meth. **A502** (2003) 236.

[74] E. Albrecht *et al.*, *COMPASS RICH-1*, Nucl. Instr. and Meth. **A478** (2002) 340.

[75] E. Albrecht *et al.*, *The Radiator Gas and the Gas System of COMPASS RICH-1*, Nucl. Instr. and Meth. **A502** (2003) 266.

[76] P. Abbon *et al.*, *Design and Status of COMPASS Fast-RICH*, to be published in Nucl. Instr. and Meth. **A**.

[77] P. Pagano, *Preliminary Measurement of Transversity at COMPASS Experiment*, PhD Thesis, Trieste 2002.

[78] P. Fauland, *The COMPASS Experiment and the RICH-1 Detector*, Doktorarbeit, Bielefeld 2004.

[79] F. Sozzi, *Identificazione di Particelle con il RICH di COMPASS al Superprotosincrotrone del CERN*, Diploma Thesis, Trieste 2003.

[80] C. Bernet *et al.*, *The COMPASS Trigger System for Muon Scattering*, Nucl. Instr. and Meth. **A 550** (2005) 217.

[81] M. D. Leberig, *Das COMPASS Triggersystem zur Messung von ΔG*, Doktorarbeit, Mainz 2002.

[82] L. Schmitt *et al.*, *The DAQ of the COMPASS Experiment*, *IEEE Trans. Nucl. Sci.* **51** (2004) 439.

[83] S. Gerassimov, *PHAST web page*, *http://ges.home.cern.ch/ges/phast/index.html*.

[84] R. Brun, F. Rademakers, *ROOT web page*, *http://root.cern.ch*.

[85] V. Alexakhine, *COMGEANT web page*, *http://valexakh.home.cern.ch/valexakh /wwwcomg/index.html*.

[86] G. Ingelman, J. Rathsman, G. A. Schuler, *A Monte Carlo Generator For Heavy Flavor Events in eP Collisions*, *Comp. Phys. Comm.* **101** (1997) 135.

[87] K. Klimaszewski, Talks given at the COMPASS Analysis Meetings, January 2005, April 2005 and June 2005.

[88] Y. Bedfer *et al.*, *COMPASS's Track Reconstruction Algorithm*, COMPASS Note 2004-1.

[89] S. Trippel, *Aufbau einer Messeinrichtung zur Bestimmung des Myonenflusses bei COMPASS*, Diploma Thesis, Freiburg 2005.

[90] C. Iselin, *Halo – A Computer Program to Calculate Muon Halo*, CERN Yellow Report, 74-17 (1974).

[91] L. Gatignon, CERN SL Division, *Private Communication*, January 2004.

[92] R. Windmolders, Universität Bonn, *Private Communication*, December 2002.

[93] O. Kouznetsov, *Talk given at COMPASS Analysis Meeting*, May 2005.

[94] A. Bressan, University of Trieste, *Private Communication*, August 2005.

[95] P. Schiavon, University of Trieste, *Private Communication*, March 2003.

[96] S. Koblitz, *Stability Web Page*, *http://wwwcompass.cern.ch/compass/software/ offline/input/stab/index.html*.

[97] C. Bernet, S. Hedicke, *Measurement of High p_t Asymmetries on 2002 Data*, COMPASS Note 2004-7.

[98] S. Procureur, CEA Saclay, *Private Communication*, May 2005.

[99] J. Pretz, *A New Method for Asymmetry Extraction*, COMPASS Note 2004-11.

[100] J. Pretz, *Asymmetry Extraction in Presence of Polarised Background*, COMPASS Note 2005-12.

[101] J. Pretz, Universität Bonn, *Private Communication*, September 2005.

[102] K. Gustafsson, *Computation of the Dilution Factor for the Year 2002 COMPASS Data*, COMPASS Note 2003-3.

[103] A. Bravar, K. Kurek, R. Windmolders, *A Monte Carlo for Polarised (Semi-Inclusive) Deep Inelastic Scattering*, Comp. Phys. Comm. **105** (1997) 42.

[104] I. Bojak, *NLO QCD Corrections to the Polarized Photo- and Hadroproduction of Heavy Quarks*, Doktorarbeit, Dortmund 2000.

[105] T. Sjostrand *et al.*, *Pythia 6.3 Physics and Manual*, Preprint, hep-ph/0308153 (2003).

[106] M. Glück, E. Reya, A. Vogt, *Dynamical Parton Distributions Revisited*, Eur. Phys. J. **C5** (1998) 461.

[107] A. Airapetian *et al.*, *Measurement of the Spin Asymmetry in the Photoproduction of Pairs of High p_t Hadrons at HERMES*, Phys. Rev. Lett. **84** (2000) 2584.

[108] B. Adeva *et al.*, *Spin Asymmetries for Events with High p_t Hadrons in DIS and an Evaluation of the Gluon Polarization*, Phys. Rev. **D70** (2004) 012002.

[109] K. Kurek, Soltan Inst. Warsaw, *Private Communication*, September 2005.

Acknowledgements

During the completion of this work I have benefited from the help and advice of many people, definitely too many to mention them all here.
I would like to thank

- Prof. Kay Königsmann for giving me the opportunity to work on the COMPASS experiment and for his support during all these years that I spent in his group. It was an interesting experience to take part in the transition of the experiment from the commissioning phase to serious physics output.
- Horst Fischer and Fritz-Herbert Heinsius for taking time for discussions and for all those useful comments and suggestions, which were of great importance.
- Sonja Hedicke for many discussions and a helpful collaboration in facing the adventure of analysing COMPASS data and the extraction of $\Delta G/G$.
- Christian Schill for helpful discussions and for proof-reading of the draft.
- Rainer Fastner and Khalil Rehmani not only for keeping the light on my desk burning and the viruses out of my computer but also for advice on which bike is the best to buy and on how Mt. Ventoux is to be tackled.
- the entire Freiburg-group for a friendly and helpful atmosphere.
- Jörg Pretz for many discussions, which helped me to understand and solve problems in the analysis, and for all his comments and ideas, that were essential for the success of this work.
- Susanne Koblitz for an excellent collaboration in the open charm analysis. The cross check of the $\Delta G/G$ extraction was a pleasure!
- Many people in the COMPASS collaboration and especially those in the open-charm group (J.-M. Le Goff, K. Kurek, N. Dedek, just to name a few) who contributed in various ways. There were many fruitful discussions and support on software questions and the like was always readily available.
- Angelika Lippitsch and Alexander Koschik – whenever the CERN hostel was overbooked I could be sure that there is a comfortable couch I could sleep on. Thanks

for countless dinners and BBQs, which were a very welcome distraction during my many stays at CERN.

- Inga Ludwig for her support especially during the "grande finale", for her patience and for countless encouragements. Special thanks also for the very careful reading of the draft, for correcting mistakes and inconsistencies and for putting things into question.

Finally, I would like to thank my parents for their constant support and valuable advice during the course of my studies with all its ups and downs.